Interplanetary Magnetic Field Influence on Flux Transfer Events at Mercury

Thesis submitted for the degree of

Doctor of Philosophy

at the University of Leicester

by

Roger Paul Leyser

Radio and Space Plasma Physics Group

Department of Physics and Astronomy

University of Leicester

September 2019

UNIVERSITY OF LEICESTER

Interplanetary Magnetic Field Influence on Flux Transfer Events at Mercury

Roger Paul Leyser

Abstract

Reconnection between the interplanetary magnetic field (IMF) and Mercury's intrinsic magnetospheric field at the dayside magnetopause drives the Dungey Cycle of magnetic flux. The formation of subsequent evolution of large magnetic structures known as flux transfer events (FTEs) therefore represents an important contribution to magnetospheric dynamics. This thesis presents three studies investigating the factors influencing the rate and location of FTEs, as well as the nature of their subsequent motion and evolution.

Flux transfer events in the dayside magnetosphere of Mercury have been visually identified using 12 Mercury years of Magnetometer data from the MErcury Surface, Space ENvironment, GEochemistry and Ranging (MESSENGER) spacecraft, covering the period from March 2011 to February 2014. The dependence of the observation rate on the orientation of the IMF in the magnetosheath is investigated, showing a clear preference for FTE formation during periods of southward IMF, and therefore antiparallel reconnection.

The locations of the FTE observations have also been analysed along with their direction of motion, in order to investigate the location and orientation of the average reconnection X-line for different IMF orientations. The motions are also used to produce a map showing the convection of the magnetic field in the dayside magnetosphere.

Finally, differences in the magnetic field signatures of the observed FTEs with various parameters, including IMF strength and orientation, are probed through the use of superposed epoch analysis. The results provide evidence of FTE rotation with increased distance from the subsolar point, as well as compression of the leading edge of the structure as it moves through the surrounding magnetic field and plasma.

Declaration

I, Roger Leyser, declare that the work within this thesis is my own. All information taken from external sources and reproduced material has been appropriately referenced. Sections of this thesis have previously been published in the following scientific paper:

Leyser, R. P., Imber, S. M., Milan, S. E., and Slavin, J. A. (2017). The influence of IMF clock angle on dayside flux transfer events at Mercury. *Geophysical Research Letters*, 44, 10,829–10,837. doi: 10.1002/2017GL074858.

Acknowledgements

Completing a PhD thesis isn't supposed to be easy, and there have certainly been challenges along the way, but it's also been a highly enjoyable and rewarding journey. Thanks must therefore be given to everyone who has helped me reach this point.

Firstly, to my supervisors, Suzie and Steve, for giving me this opportunity. Thank you for guiding me through these past 4 years, and for your encouragement and patience, even when I disappeared off to another country for the final few months! I've also been very fortunate to work within a great RSPP group, providing cakes, crosswords, curry and countless entertaining and productive tea breaks. Thank you in particular to Timothy, Alexandra, Rosie, and Katie, for putting up with my terrible jokes; Matt for joining in with them and also providing entertaining chats and advice; and Jenny, for your support, encouragement and advice - I couldn't have asked for a better group of people to share offices with over the years. A number of great friends have shared the whole journey through undergraduate and PhD with me - apologies and thanks must go to Jordan, Adam and Sam for having to endure 8 years of me! Thank you also to everyone who played Monday afternoon football, for providing a valuable source of stress relief!

Of course, special thanks must be extended to my family, for your constant support over the years. Thank you for providing me with the opportunities and encouragement that have enabled me to reach this point.

Finally, to Hayley, who has been at my side throughout the entire journey. You are a constant inspiration, and without your unwavering support and belief in me I couldn't have completed this PhD journey.

Contents

List of Figures

List of Tables

Chapter 1

Introduction

The subject of this thesis is the interaction between the planetary-dominated magnetosphere of Mercury and the solar-governed regime of interplanetary magnetic field (IMF) and solar wind, at the boundary known as the magnetopause. This interaction can take a wide range of forms, but this work focuses on the process of magnetic reconnection, through which planetary magnetic field becomes interconnected with the IMF, facilitating the transfer of solar wind plasma into the magnetosphere and driving the Dungey cycle [Dungey, 1961] of magnetic flux circulation that controls the structure and dynamics of Mercury's space environment.

This chapter introduces the fundamental laws and processes that describe the behaviour of space plasmas, providing a basis for understanding and discussing the physics of Mercury's magnetosphere. Chapter 2 reviews the current literature relevant to the Mercury system and flux transfer events, and the third chapter describes the instrumentation and data used in this thesis. The work presented in Chapters 4-6 focuses on flux transfer events at Mercury, and the factors influencing their formation and evolution. Finally, Chapter 7 provides a summary of this thesis and discusses possible directions of future research.

1.1 Maxwell's Equations

The nature and temporal evolution of electric (**E**) and magnetic (**B**) fields are described by Maxwell's equations. In their differential forms for fields in a vacuum, these are:

$$\nabla \cdot \mathbf{E} = \frac{\rho_{\mathrm{q}}}{\varepsilon_0} \tag{1.1}$$

$$\nabla \cdot \mathbf{B} = 0 \tag{1.2}$$

$$\nabla \times \mathbf{E} = -\frac{\partial \mathbf{B}}{\partial t} \tag{1.3}$$

$$\nabla \times \mathbf{B} = \mu_0 \mathbf{j} + \varepsilon_0 \mu_0 \frac{\partial \mathbf{E}}{\partial t}, \tag{1.4}$$

where ρ_{q} is the charge density, ε_0 is the permittivity of free space, μ_0 is the permeability of free space, and $\mathbf{j}$ is the current density.

Equation 1.1 is Gauss' Law for electricity, and describes how regions of electric charge density relate to electric fields, where positive charges act as sources and negative charges as sinks. This is in contrast with magnetic fields, which are shown in Equation 1.2, also known as the *law of no monopoles*, to exist without a point source, and therefore have no divergence.

The next two equations describe how electric and magnetic fields are connected through their spatial and temporal variations. Faraday's Law, shown in Equation 1.3, indicates that a magnetic field changing in time will induce spatial variations in the electric field, and vice versa. Equation 1.4 is the Ampère-Maxwell Law, and describes the spatial variations in a magnetic field. The second term on the right is the displacement current, but for most space plasmas the electric field varies on such long timescales that this term can be ignored, leaving only the term related directly to the electrical current.

1.2 The Motion of Charged Particles in Electromagnetic Fields

Maxwell's equations demonstrate how electric fields are produced by stationary charged particles, and when these particles move they then produce magnetic fields. However, the coupling is twofold, as the subsequent motion of the charged particles is strongly influenced by the fields that have been generated. The equation of motion for a particle of mass m and charge q, travelling at a velocity v through electromagnetic fields is given by

$$m\frac{d\mathbf{v}}{dt} = q\mathbf{E} + q\mathbf{v} \times \mathbf{B}, \tag{1.5}$$

which is Newton's second law with the force expressed in terms of **E** and **B**. The right hand side is the Lorentz force acting on the particle due to the magnetic field and Coulomb interactions. In this section, this equation of motion is considered in conjunction with Maxwell's equations to discuss the motion of charged particles in various configurations of electric and magnetic fields.

1.2.1 Gyromotion

The simplest case to consider is that of a charged particle in a static, uniform magnetic field (e.g. $\mathbf{B} = B\hat{\mathbf{z}}$), and no electric field ($\mathbf{E} = 0$), travelling with a velocity $\mathbf{v} = (v_x, v_y, v_z)$. Equation 1.5 can then be simplified and expressed in component form as

$$\frac{dv_x}{dt} = \frac{qB}{m}v_y \tag{1.6a}$$
$$\frac{dv_y}{dt} = -\frac{qB}{m}v_x \tag{1.6b}$$
$$\frac{dv_z}{dt} = 0. \tag{1.6c}$$

Taking the derivative of Equation 1.6a and substituting Equation 1.6b yields a simple harmonic motion solution:

$$\frac{d^2v_x}{dt^2} = -\omega_{\mathrm{g}}^2 v_x, \tag{1.7}$$

with a similar expression for v_y. This indicates that charged particles gyrate around the magnetic field with a gyrofrequency given by

$$\omega_g = \frac{qB}{m}. \tag{1.8}$$

The presence of the charge in this expression means that particles of opposite charge will gyrate with opposite chirality, therefore representing a circular current around the magnetic field line. The sense of this current is such that the magnetic field it generates acts in the opposite direction to the external field around which the particles are gyrating, creating a *diamagnetic effect*. The opposite sense of gyration for positive and negative particles has important consequences in more complex scenarios, as will be discussed later in this chapter. The centre of the particle's orbit is known as the *guiding centre*, and the gyroradius, r_g, of gyration is given by

$$r_g = \frac{v_\perp}{|\omega_g|} = \frac{mv_\perp}{|q|B}, \tag{1.9}$$

where $v_\perp = \sqrt{v_x^2 + v_y^2}$ is the velocity of the particle perpendicular to $\mathbf{B}$.

1.2.2 Pitch Angle

In addition to the perpendicular motion described above, the particle may have some velocity $v_\parallel$ parallel to the magnetic field, resulting in a helical motion. It can be shown that the total kinetic energy of the particle is conserved, and therefore the total velocity

$$v = \sqrt{v_\perp^2 + v_\parallel^2} = \text{constant}. \tag{1.10}$$

Although the total velocity remains constant, the relative components in the parallel and perpendicular directions can vary as the particle moves through different field regions. The ratio of the two components defines the *pitch angle*, α, of the particle:

$$\alpha = \tan^{-1}\left(\frac{v_\perp}{v_\parallel}\right), \tag{1.11}$$

which describes the angle between the particle's velocity and its guiding centre. For $0^\circ \leq \alpha < 90^\circ$, the particle has a component of its velocity parallel to the magnetic field, and for $\alpha = 90^\circ$ the orbit is circular.

1.2.3 Magnetic Mirroring

If a charged particle moves through a region of non-uniform magnetic field, its motion is modified from the simple gyromotion discussed in Section 1.2.1. We first consider a scenario where the particle moves into a region of converging magnetic field, such that $|\mathbf{B}|$ increases along the trajectory, as shown in Figure 1.1. Assuming some initial parallel velocity, as the particle moves in a helical path it experiences an increased Lorentz force ($\mathbf{F} = q\mathbf{v} \times \mathbf{B}$), a component of which points in the anti-parallel direction. This acts to increase $v_\perp$, but Equation 1.10 shows that the total velocity must remain constant, therefore $v_{\parallel}$ decreases. From Equation 1.11, the pitch angle therefore increases as the particle penetrates further into the increased field strength, until its entire velocity is in the perpendicular component and $\alpha = 90°$. This is known as the *magnetic mirror point*, due to the Lorentz force continuing to provide an anti-parallel acceleration that leads to the particle reflecting back along the field.

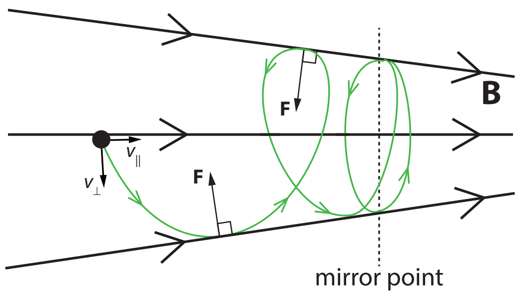

Figure 1.1: Sketch showing the trajectory of a charged particle in a converging magnetic field. Figure from Raymer [2018].

Mathematically, this can be shown using the *magnetic moment*, μ, of the particle, also referred to as the *first adiabatic invariant*:

$$\mu = \frac{W_{\perp}}{B} = \frac{mv_{\perp}^2}{2B}, \tag{1.12}$$

where $W_{\perp}$ is the perpendicular kinetic energy of the particle. Using the definition of pitch angle, this can be rewritten as

$$\mu = \frac{mv^2 \sin^2 \alpha}{2B}. \tag{1.13}$$

The magnetic moment remains constant in fields that vary on long timescales. As the speed, v, is also constant the pitch angle must vary with changing magnetic field strength. In the above example of a gradient in $\mathbf{B}$, α increases as the particle enters the region of stronger magnetic field. From Equation 1.11, this results in a conversion from parallel velocity to perpendicular. It can be shown that the field strength at the mirror point, B_m, is given by

$$B_m = \frac{B}{\sin^2 \alpha}. \tag{1.14}$$

The lack of other particle properties, such as mass, charge and velocity, in Equation 1.14 implies that the only factor determining how far a particle will propagate into a converging magnetic field is its pitch angle. Magnetic field gradients along the field direction occur at both polar regions of planetary dipolar fields, resulting in particles mirroring as they approach the planet and undergoing bounce motion between the poles.

1.2.4 Gradient Drift

In addition to magnetic field gradients parallel to the field direction, planetary dipolar magnetic fields also exhibit gradients perpendicular to **B**. This produces an additional force acting on the particles, resulting in a *grad-B (gradient) drift* in the direction perpendicular to both the magnetic field and its gradient. As the gyroradius of a particle (Equation 1.9) is dependent on the magnetic field strength, B, a particle gyrating around a magnetic field line in a region where large gradients exist perpendicular to **B** will experience changes in the field strength as it completes its gyration, resulting in an instantaneous gyroradius that changes through the particle's orbit. Such variations result in a 'hopping' motion of the particle, as shown in Figure 1.2, that causes the particle to drift. The velocity of the drift is given by

$$\mathbf{v}_{\nabla B} = \frac{mv_{\perp}^2}{2qB^3}\left(\mathbf{B} \times \nabla B\right). \tag{1.15}$$

The presence of the charge, q, in Equation 1.15 describes the oppositely directed drift velocities seen in Figure 1.2 for ions and electrons, which produces a net current that flows perpendicular to both the magnetic field and its gradient.

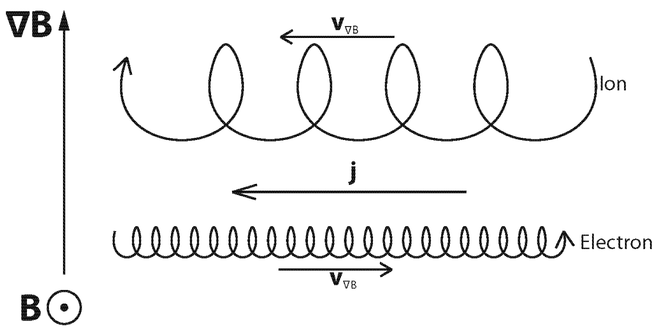

Figure 1.2: Sketch showing the trajectories of oppositely charged particles in a region where gradients in the magnetic field exist perpendicular to **B**. Figure from Sandhu [2016].

1.3 Magnetohydrodynamics

In Section 1.2, the motion of individual constituent particles is considered in describing the behaviour of a plasma. A more holistic approach, magnetohydrodynamic (MHD) theory, describes the entire plasma as a conducting, quasi-neutral fluid using its macroscopic, bulk properties, such as average velocity, temperature and density.

1.3.1 General MHD Equations

In order to discuss the bulk motions of a plasma, some basic properties must first be defined, with the assumption of quasi-neutrality such that the number density, n, of ions and electrons (subscripts i and e respectively) is equal, and taking the electron mass, m_e to be negligible compared to the mass of the ions, m_i:

$$n = n_i = n_e \tag{1.16}$$

$$m = m_i + m_e \approx m_i \tag{1.17}$$

$$\rho = n_i m_i + n_e m_e \tag{1.18}$$

$$\mathbf{V} = \frac{m_i n_i \mathbf{V}_i + n_e m_e \mathbf{V}_e}{n_i m_i + n_e m_e} \approx \mathbf{V}_i, \tag{1.19}$$

where m is the fluid mass, ρ is the mass density, and $\mathbf{V}$ is the bulk velocity of the plasma. $\mathbf{V_i}$ is the bulk velocity of the ions, defined as the average velocity of all ions, and an equivalent definition applies to $\mathbf{V_e}$. Equation 1.19 indicates that because of the low electron mass relative to the mass of the ions, the fluid velocity, which is defined as the centre-of-mass velocity, is carried almost entirely by the ion motions.

The *mass continuity equation* shows that mass is conserved across a classical, non-relativistic plasma:

$$\frac{\partial \rho}{\partial t} + \nabla \cdot (\rho \mathbf{V}) = 0, \tag{1.20}$$

where the right hand side reflects the assumption that there are no source or loss regions present in the plasma.

In addition to the conservation of mass shown in Equation 1.20, the total momentum of a plasma must also be conserved. The contributions to momentum changes are combined in Equation 1.21 to produce the *general equation of motion* for a plasma:

$$\rho \frac{d\mathbf{V}}{dt} = \rho \mathbf{g} - \nabla P + \rho_q \mathbf{E} + \mathbf{j} \times \mathbf{B}, \tag{1.21}$$

where $\mathbf{g}$ is acceleration due to gravity, P is the summed electron and ion pressure, ρ_q is the charge density introduced by any departures from quasi-neutrality in the plasma. The current density, $\mathbf{j}$, is defined as

$$\mathbf{j} = ne(\mathbf{V}_i - \mathbf{V}_e), \tag{1.22}$$

where $-e$ is the charge of an electron.

The first term on the right of Equation 1.21 represents the contributions from gravitational forces, and can be neglected for most space plasmas. The second term is the summed electron and ion pressure acting on the plasma. The third term is the electric force, which can also be neglected for non-relativistic plasmas when compared to the Lorentz force, $\mathbf{j} \times \mathbf{B}$.

1.3.2 Ohm's Law

The evolution of the current density can be related to other plasma properties through the generalised Ohm's Law. In most space plasmas, as with the equation of motion (Equation 1.21), several of the terms are negligible. However, near the magnetopause in the reconnection diffusion region, large currents exist perpendicular to the magnetic field, and there is a significant contribution from each term. In all other scenarios, the generalised Ohm's law can be reduced and simplified for a plasma moving with respect to an external observer:

$$\mathbf{j} = \sigma \left(\mathbf{E} + \mathbf{V} \times \mathbf{B} \right), \tag{1.23}$$

where σ is the conductivity of the plasma, defined as

$$\sigma = \frac{n_e e^2}{m_e \nu_c}. \tag{1.24}$$

The frequency of collisions between ions and electrons is included in this expression as ν_c. However, ideal MHD plasmas are collisionless, such that $\sigma \to \infty$, and Ohm's law therefore leads to

$$\mathbf{E} = -\mathbf{V} \times \mathbf{B}. \tag{1.25}$$

1.3.3 Magnetic Pressure and Tension

Equation 1.21 contains the Lorentz force, $\mathbf{j} \times \mathbf{B}$, which is also present in the generalised Ohm's law but taken to be a negligible term in producing the simplified version given in Equation 1.23. Using Ampère's Law (Equation 1.4) in its non-relativistic form this force can be rewritten as

$$\begin{aligned}\mathbf{j} \times \mathbf{B} &= \frac{1}{\mu_0} (\nabla \times \mathbf{B}) \times \mathbf{B} \\ \mathbf{j} \times \mathbf{B} &= \frac{1}{\mu_0} (\mathbf{B} \cdot \nabla) \mathbf{B} - \nabla \left(\frac{\mathbf{B}^2}{2\mu_0} \right) \end{aligned} \tag{1.26}$$

The first term on the right of Equation 1.26 is the *magnetic tension force*, T_{mag}, which acts to straighten out any curvature in the magnetic field lines, with a radius of curvature R_c:

$$\mathbf{T}_{mag} = -\frac{B^2}{\mu_0} \frac{\hat{\mathbf{R}}_\mathbf{c}}{R_c}. \tag{1.27}$$

By comparison with the pressure gradient in Equation 1.21, the second term in Equation 1.26 can be interpreted as the force due to *magnetic pressure*, P_{mag}:

$$P_{mag} = \frac{B^2}{2\mu_0}. \tag{1.28}$$

1.3.4 Plasma Beta

The total pressure in a magnetised plasma comes from the combination of the magnetic pressure in Equation 1.28 and the particle pressure indicated in Equation 1.21. For a plasma in equilibrium, the particle pressure gradient is balanced by the magnetic pressure, such that

$$\nabla \left(P + \frac{B^2}{2\mu_0} \right) = 0. \tag{1.29}$$

The plasma beta is a useful parameter for describing the nature of the plasma that can be defined from this equation, enabling comparison of the relative strengths of the plasma and magnetic pressure.

$$\beta = \frac{k(n_i T_i + n_e T_e)}{B^2/2\mu_0}, \tag{1.30}$$

where k is the Boltzmann constant, and $T_{i,e}$ denotes the ion and electron temperature. When $\beta \ll 1$, the magnetic pressure dominates and the plasma is described as being *low-beta*; and a *high-beta* plasma is one in which the particle pressure dominates, such that $\beta \geq 1$.

1.3.5 Diffusion and the Frozen-in Flow Approximation

In a magnetised plasma, any changes in the magnetic field can have important consequences for the properties and behaviour of the plasma. Starting from Faraday's law and Ohm's law (Equations 1.3 and 1.23), the temporal evolution of the magnetic field is shown to be

$$\frac{\partial \mathbf{B}}{\partial t} = \nabla \times \left(\mathbf{V} \times \mathbf{B} - \frac{\mathbf{j}}{\sigma} \right). \tag{1.31}$$

Substituting Ampère's law (Equation 1.4) for the final term and rearranging using a vector identity then yields the *magnetic induction equation*:

$$\frac{\partial \mathbf{B}}{\partial t} = \nabla \times (\mathbf{V} \times \mathbf{B}) + \frac{1}{\mu_0 \sigma} \nabla^2 \mathbf{B}. \tag{1.32}$$

The two terms on the right-hand side represent the *convection* and *diffusion* of the magnetic field:

$$\frac{\partial \mathbf{B}_{conv}}{\partial t} = \nabla \times (\mathbf{V} \times \mathbf{B}) \tag{1.33}$$

$$\frac{\partial \mathbf{B}_{diff}}{\partial t} = \frac{1}{\mu_0 \sigma} \nabla^2 \mathbf{B}. \tag{1.34}$$

In ideal space plasmas, $\sigma \to \infty$, and the spatial scale of magnetic field variations is generally very large in comparison with the gyroradii of the particles, therefore the diffusion term becomes negligible compared to the convection term. In this instance, magnetic field cannot diffuse through the plasma and its temporal variability is represented by Equation 1.33. This implies that the motions of the magnetic field and the plasma are intricately linked together through the *frozen-in flow* condition. If the magnetic energy dominates, then the particles will continue to gyrate around the moving magnetic field lines in such a way that the bulk velocity, which is defined by the average particle motions, carries the plasma with the magnetic field and the particles remain connected to the same flux tube. Conversely, a plasma with particle energy dominating will cause the magnetic flux tubes to follow the plasma bulk motion. As a consequence of this frozen-in condition, two plasmas of different origins, and their associated magnetic fields, cannot mix under convection-dominated conditions.

1.3.6 Magnetic Reynolds Number

Although the frozen-in flow condition applies to most space plasmas, in some scenarios the diffusion term is sufficiently large that it becomes important. The relative importance of the two terms can be expressed through a dimensionless quantity known as the *magnetic Reynolds number*,

$$R_M = \frac{|\nabla \times (\mathbf{V} \times \mathbf{B})\,|}{|\nabla^2 \mathbf{B}/\mu_0 \sigma|} \approx \frac{VB/L}{B/\mu_0 \sigma L^2} = \mu_0 \sigma V L, \tag{1.35}$$

where V is the typical velocity of the plasma perpendicular to the magnetic field, and L is the typical length scale over which $\mathbf{B}$ varies. For highly conducting plasmas with small spatial gradients in the magnetic field, it can be seen from Equation 1.35 that $R_M \gg 1$, indicating that the frozen-in flow approximation is valid and the plasma is dominated by convection. However, when $R_M \sim 1$, this approximation breaks down and the diffusion term becomes important. This can occur at current sheets that form between two oppositely directed magnetic fields, such as at a planetary magnetopause or the magnetotail current sheet.

1.3.7 Magnetic Reconnection

The assumption of frozen-in flow can break down at the boundary between a planetary magnetic field and its associated plasma, and a field and plasma of solar origin. This boundary is known as the *magnetopause.* In this region, there are often steep spatial gradients due to oppositely-directed magnetic fields, and as a result the magnetic Reynolds number approaches unity and the diffusion term in Equation 1.32 becomes important.

Figure 1.3 shows a schematic of the magnetic field geometry at a region of oppositely directed magnetic fields. Plasma flowing perpendicular to $\mathbf{B}$ drives spatial gradients in the magnetic field that have similar length scales to the gyroradii of the particles. This forms two diffusion regions; the larger of which exists on a similar

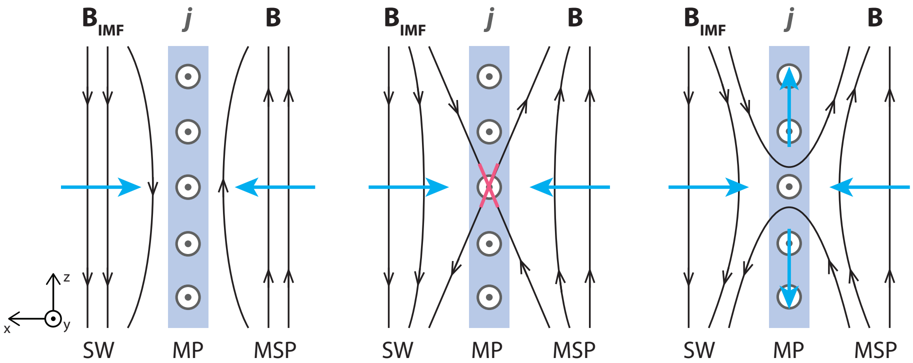

Figure 1.3: Sketch showing the configuration of magnetic field lines during reconnection. The solar wind (SW) carries with it magnetic field of solar origin ($\mathbf{B_{IMF}}$), which is oppositely directed to the planetary field **B** in the magnetosphere (MSP). Reconnection therefore occurs at the magnetopause (MP), along which a current, **j**, flows due to grad-B drift (Section 1.2.4). The pink cross shows the location of the reconnection X-line, and the motion of magnetic field lines and plasma is indicated by the blue arrows. Figure from Raymer [2018].

scale to the ion gyroradius, allowing ions from both sides of the current sheet to mix, and due to their smaller gyroradii the electrons mix in the smaller diffusion region. The magnetic field lines on both sides of the current sheet are also able to diffuse through the plasma, where they can merge together in a process known as *reconnection*. This occurs at a location termed the *X-line* due to its geometry, as shown in Figure 1.3. This process produces two newly reconnected field lines that are highly kinked, and are therefore accelerated away from the X-line by the magnetic tension force (Equation 1.27).

The conditions required for reconnection to occur at the magnetopause, and the subsequent features that form in the reconnection process, are fundamental to this thesis, and will be discussed in greater detail in Chapter 2.

1.4 The Solar Wind

Many of the dynamic processes in the space environment of inner solar system planets are driven by interactions with magnetic field and plasma of solar origin. The Sun has an internally produced magnetic field that can generally be approximated as dipolar, although the Solar Cycle of activity variations introduces higher order terms at the most active times, known as solar maximum. However, this internal field does not retain its dipolar nature away from the surface of the Sun. The outer atmosphere of the Sun, known as the corona, exists at an extremely high temperature of over 10^6 K, and therefore consists of completely ionised gas at a much higher pressure than can be contained by the Sun's gravitational pull. Plasma therefore streams constantly outwards from the corona, propagating throughout the solar system in the form of the *solar wind.* This plasma is highly conducting, and obeys the frozen-in flow condition established in Equation 1.32 that leads to it stretching the solar magnetic field out of its dipolar configuration and through the heliosphere, where it becomes the *interplanetary magnetic field* (IMF).

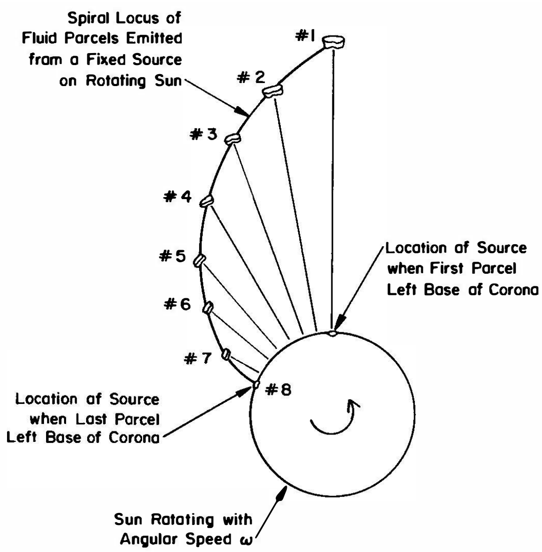

Figure 1.4: A sketch showing the generation of the azimuthal component of the IMF due to solar rotation. Figure from Kivelson & Russell [1995].

Figure 1.4 shows how the orientation of the IMF is strongly driven by the rotation of the Sun, and varies with heliocentric distance. All plasma parcels originating from the same point on the surface of the Sun are frozen-in to the same magnetic flux tube, and propagate radially outwards. However, the rotation of the Sun means each of these parcels is ejected at a different heliocentric longitude, yielding the *Parker spiral* [Parker, 1958] structure of IMF near the ecliptic plane, where the IMF becomes more azimuthal at greater heliocentric distances. As the Sun's dipolar field is stretched outwards into this spiral structure, a large shear is produced at the magnetic equator, resulting in the formation of the *heliospheric current sheet.* The radial direction of the IMF reverses across this current sheet, therefore the IMF direction can vary considerably on short timescales as an observer crosses between northern and southern magnetic latitudes. Variations in the IMF orientation are also introduced due to the offset of the Sun's magnetic axis with respect to its axis of rotation and higher order terms in the Sun's magnetic field than the simple dipolar approximation, both of which contribute to the rippled and tilted *'ballerina's skirt'* configuration of the heliospheric current sheet seen in Figure 1.5.

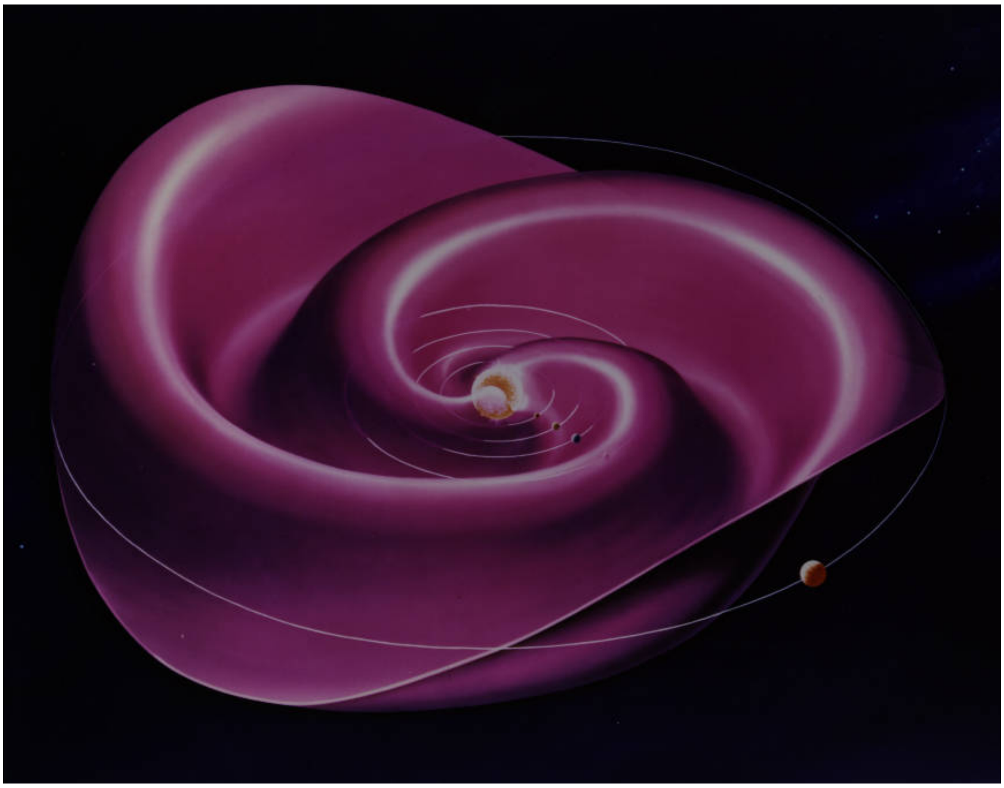

Figure 1.5: Artist's impression of the heliospheric current sheet, showing the 'ballerina's skirt' structure. Figure from NASA [2013].

1.5 The Magnetosphere

Intrinsic planetary magnetic fields can be approximated as dipolar in origin, and, due to the frozen-in flow condition prohibiting large-scale mixing of different plasma populations, carve out a cavity in the flow of the solar wind. This cavity, known as the *magnetosphere*, presents a large obstacle to the solar wind as it travels outwards through the solar system at an average velocity of $\sim$ 400 km s^{-1} [Baumjohann & Treumann, 1997]. The flow velocity is considerably greater than the speed of sound in the plasma, therefore the obstruction produced by the magnetosphere causes an extended *bow shock* to form upstream of the planet, slowing the solar wind flow to subsonic speeds, as well as heating and compressing the plasma. The shocked plasma and its accompanying magnetic field continue to propagate through the *magnetosheath*, the region of space between the bow shock and the outer extent of the planetary magnetic field. The two populations of solar and planetary origin are then separated by a boundary termed the *magnetopause*, which takes the form of a thin current sheet. A schematic of the magnetosphere is shown in Figure 1.6.

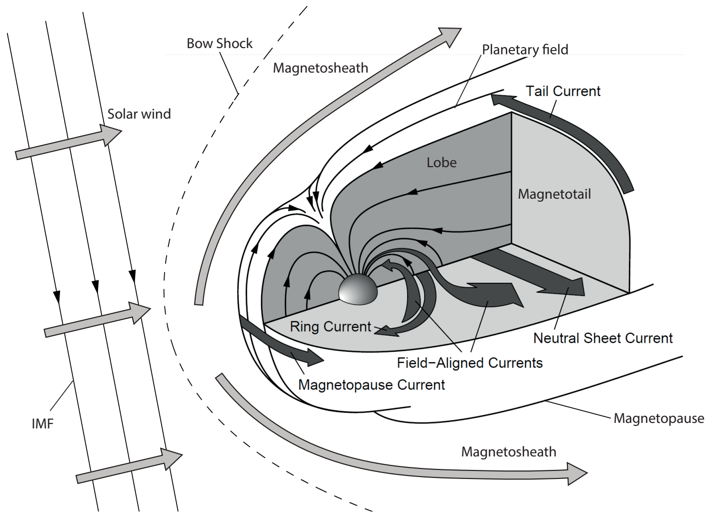

Figure 1.6: Sketch showing the configuration of the magnetosphere. The bow shock is indicated by the dashed line, and flow directions of the solar wind upstream and in the magnetosheath are shown by light grey arrows. Dark grey arrows indicate currents that form in the magnetosphere. Figure adapted from Baumjohann & Treumann [1997] and Hunt [2016].

1.5.1 Magnetopause

The exact location of the magnetopause depends on the pressure balance between oncoming solar wind and magnetic pressure due to the planetary dipole field. From Equation 1.29, it can be shown that

$$P_{SW} + \frac{B_{SW}^2}{2\mu_0} = P_{MSp} + \frac{B_{MSp}^2}{2\mu_0}, \tag{1.36}$$

where the subscripts SW and MSp refer to quantities in the solar wind and the magnetosphere just inside the magnetopause respectively. The first term on the right, the planetary plasma pressure, can be neglected in comparison to the magnetic pressure exerted by the dipolar field, denoted by the second term on the right. Similarly, the low strength of the IMF means the magnetic pressure term on the left can be neglected in comparison to the solar wind ram pressure, also referred to as the *dynamic pressure*, given by

$$P_{dyn} = n_{SW} m_i V_{SW}^2 = \rho V_{SW}^2. \tag{1.37}$$

Here, the thermal pressure and electron dynamic pressure can be neglected as the majority of the solar wind energy comes from the bulk ion motion. The total pressure exerted on the magnetospheric field by the solar wind will be twice the solar wind ion dynamic pressure due to reflection of the ions at the magnetopause, and it can be shown that the magnetospheric field strength just inside the magnetopause is twice the dipolar field strength ($B_{MSp} = 2B_{dip}$), where the dipolar field strength is given by

$$B_{dip} = B_{eq} \left(\frac{R_P}{R_{MP}} \right)^3, \tag{1.38}$$

where B_{eq} is the dipolar field strength on the equator, R_P is the planet's radius, and R_{MP} is the *subsolar standoff distance*, the planetocentric distance to the magnetopause in the equatorial plane.

By rearranging the above equations and removing the negligible terms in Equation 1.36 it can be shown that the subsolar standoff distance varies inversely with the sixth root of the dynamic pressure:

$$R_{MP} = \left(\frac{B_{eq}^2}{\mu_0 P_{dyn}} \right)^{\frac{1}{6}} R_P. \tag{1.39}$$

The location of the magnetopause is therefore reasonably steady during typical solar wind conditions, where, in the case of the Earth, values of $n_{SW} = 5$ cm^{-3}, $V_{SW} = 400$ km s^{-1}, $B_{eq} \sim 31000$ nT yield an approximate subsolar standoff distance of 10 R_E. For Mercury, where $n_{SW} = 50$ cm^{-3} [Blomberg *et al.*, 2007], $B_{eq} \sim 300$ nT, and all other parameters are the same as at Earth, Equation 1.39 yields a magnetopause standoff distance of 1.45 R_M.

Away from the subsolar point, the incoming solar wind impacts the magnetopause obliquely, thereby imparting a smaller force, with the result that the magnetopause flares outwards around the flanks. At the dawn-dusk terminator, the distance to the magnetopause is found to be approximately 14 R_E, and the distance increases further anti-sunward as the solar wind flow direction tends towards parallel to the magnetopause. This produces the bullet-shaped magnetopause shown in Figure 1.6, with an extended magnetotail forming due to the circulation of magnetic flux that will be discussed in the following section.

1.5.2 Dungey Cycle and Magnetospheric Flows

The above picture of the magnetopause assumes that there is no mixing of the planetary and solar populations, but as discussed in Section 1.3.7, large gradients in the magnetic field can cause a breakdown of the frozen-in flow approximation. At the nose of the magnetopause, such gradients can exist on spatial scales similar to the particle gyroradii when the IMF in the magnetosheath has a southward component.

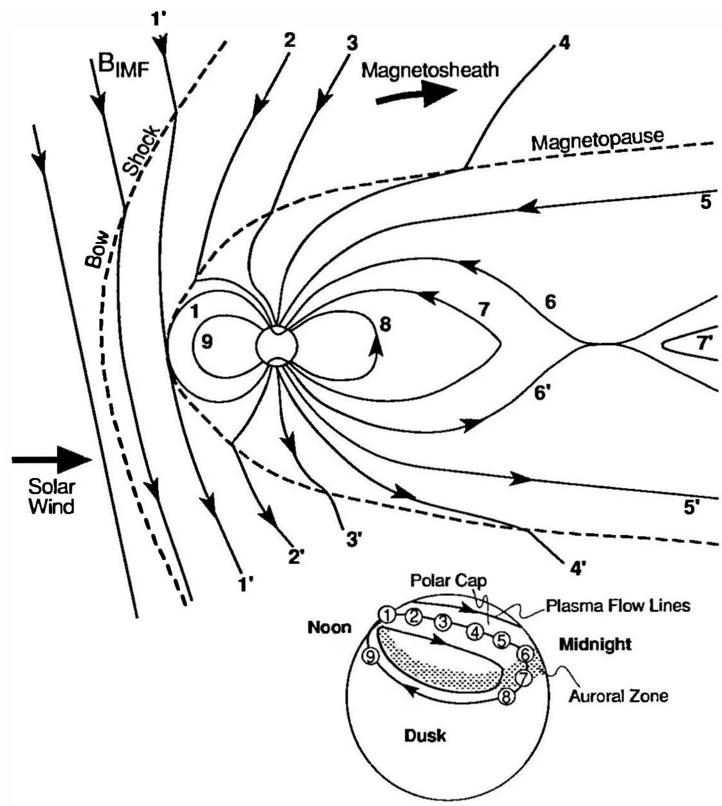

Figure 1.7: Schematic showing the Dungey cycle of magnetic flux circulation due to reconnection at the nose of the magnetopause during southward IMF. Figure from Kivelson & Russell [1995].

Figure 1.7 shows the evolution of magnetic flux in the magnetosphere during a prolonged period of dayside reconnection in the simplest case of southward IMF, as proposed by Dungey [1961]. As the IMF approaches the nose of the magnetopause, it enters the diffusion region and reconnects with the *'closed'* planetary field line **1** at the neutral point. Closed field lines are defined as those having a magnetic footprint at both poles of the planet, whereas *'open'* field lines have only 1 footprint on the planet as the other end is connected to the IMF. Following reconnection, the IMF and dipolar field line form two open field lines, **2** and **2'**, one connected to each hemisphere. As the solar wind propagates anti-sunward, these field lines are carried tailward, and their footprints convect across the polar cap.

The open field lines continue to stretch tailward due to the magnetosheath flow, as shown by field lines **3-5**, where the pile-up of magnetic flux forms the *northern* and *southern magnetospheric lobes*. Continued dayside reconnection adds further open flux to the tail lobes, where the field lines are oppositely directed. Another reconnection site therefore forms, closing field lines **6** and **6'** in the magnetotail. Magnetic tension forces due to the kinked field through the X-line then release the unconnected field line **7'** anti-sunward, as well as causing the newly closed field line **7** to become more dipolar as it moves towards the planet. The continues (**8**) before the closed field lines convect around the flanks of the planet and return to the dayside (**9**) to complete the Dungey cycle.

1.6 Coordinate Systems

In the following chapters, a number of different coordinate systems will be utilised to discuss the data and results; these will be introduced below for reference.

1.6.1 Mercury Solar Magnetospheric

The most common coordinate system used to describe Mercury's magnetosphere is Mercury Solar Magnetospheric (MSM), which has its origin at the centre of Mercury's dipolar field. The X axis points towards the Sun, the Z axis is aligned with the dipolar magnetic north, and Y completes the right hand set, such that positive-Y is opposite to Mercury's orbital direction around the Sun. It is also useful to convert this coordinate system into one that takes into account the changing orbital direction and velocity relative to the solar wind. The aberrated MSM′ system rotates the MSM X and Y coordinates by a varying amount as Mercury completes its elliptical orbit, such that X′ is antiparallel to the average solar wind direction. In this thesis, we assume an average solar wind velocity of 400 km s^{-1} in calculating the aberration angle.

1.6.2 Boundary Normal

When considering measurements near the magnetopause, a magnetopause boundary normal coordinate system is used to compare features at different points on the surface. This coordinate system is defined as follows: N is the outward normal to the magnetopause at that location, the M direction is obtained by taking the cross product of N and the MSM Z′ axis, and L completes the right hand set as the cross product of M and N.

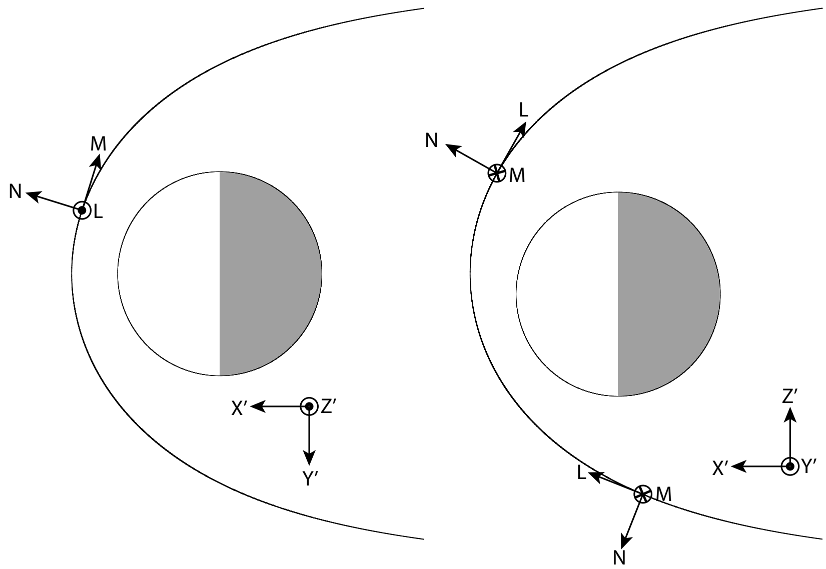

Figure 1.8: Schematic showing the magnetopause boundary normal coordinate system, with cuts through the plane of the magnetic equator (left) and noon-midnight meridian (right). The aberrated MSM’ axes are indicated for reference.

1.6.3 Minimum Variance

As magnetic features move away from the magnetopause, they may retain their shape but change orientation such that the boundary normal coordinates defined above are no longer suitable. This can be the case for flux transfer events (FTEs), which will be introduced in detail in Chapter 2. In this instance, the minimum variance coordinate system can be helpful, and is defined by an orthogonal set of eigenvectors describing the directions of maximum, intermediate, and minimum variance of a time series of magnetic field data [Sonnerup & Cahill, 1967; Sonnerup & Scheible, 1998]. The interpretation and application of minimum variance analysis (MVA) will be discussed in greater detail in Chapters 2 and 5.

1.6.4 Magnetic Local Time

Any point in the magnetosphere can be described by a radial distance from the centre of the dipolar field, its magnetic latitude and the magnetic local time (MLT). Similar in concept to longitude, lines of constant magnetic local time connect both magnetic poles. There are 24 hours of MLT, which is defined here with respect to the aberrated MSM′ coordinate system to identify symmetries and asymmetries either side of the nose of the magnetopause. As a result, 12 (noon) points along the X′ MSM axis, and 18 (dusk) is along the positive Y′ MSM direction. This MLT system therefore stays fixed with respect to the incoming solar wind as the planet rotates underneath it.

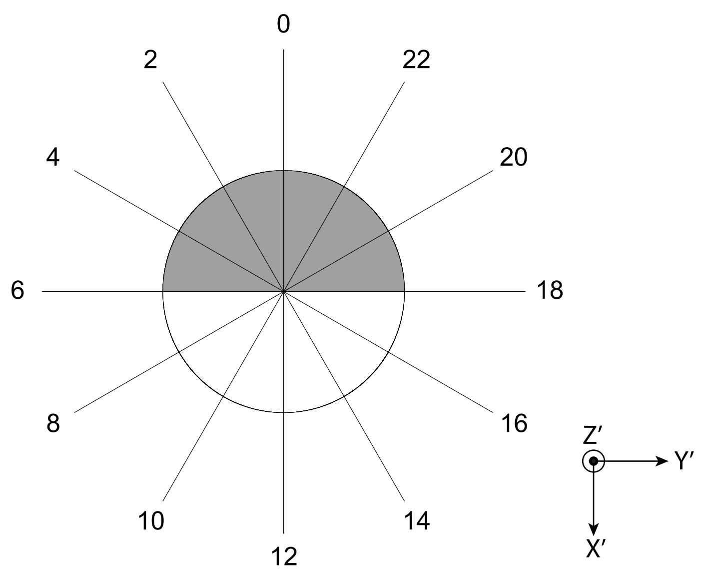

Figure 1.9: Schematic showing magnetic local time, viewed from above the north pole, with the solar wind incoming from the bottom. The aberrated MSM’ axes are indicated for reference.

1.6.5 Clock Angle

The orientation of the IMF has important consequences on magnetospheric dynamics, particularly in the rate and location of reconnection at the dayside magnetopause. The *clock angle* is therefore an important descriptor of the angle between the IMF and magnetic north in the MSM′ Y-Z plane, where 0° indicates the IMF is directed northwards and 90° is due eastward, such that

$$\theta = \tan^{-1}\left(\frac{B_{Y'}}{B_{Z'}}\right), \tag{1.40}$$

where the IMF components are defined in MSM′ coordinates.

Chapter 2

Literature Review

This chapter presents a review of the literature relevant to the work in this thesis, providing a basis for the studies in Chapters 4-6. The process of magnetic reconnection, introduced in Section 1.3.7, is explored in more detail, with specific consideration of how it is influenced by conditions in the solar wind and interplanetary magnetic field. Flux transfer events are then discussed in the context of reconnection at Earth, providing a basis for later comparison with those seen at Mercury. The Mercury system is then introduced, detailing the properties of its orbit and how this affects the conditions in the space environment. An overview of Mercury's magnetosphere is provided, including a discussion of the internal magnetic field and its interaction with the solar wind. Finally, the previous studies identifying and analysing flux transfer events at Mercury are summarised.

2.1 Magnetic Reconnection

The dynamics of the space environment of the magnetised inner Solar System planets, Mercury and Earth, are strongly driven by the interaction between the magnetosphere and the solar wind. Two theories were proposed to explain how magnetospheric convection is influenced by the solar wind. Axford & Hines [1961] suggested that the anti-sunward solar wind flow has a viscous interaction with closed magnetospheric flux tubes at the magnetopause, causing them to be dragged tailward. At the same time, Dungey [1961] postulated the open magnetosphere model elucidated in Chapter 1.5.2 to explain the circulation of magnetic flux by invoking magnetic reconnection at the nose of the magnetosphere between a southward IMF and the northward planetary field. Subsequent reconnection in the magnetotail closes open field lines, with return flows completing the cycle on a timescale of around 12 hours, albeit with considerable variability depending on the upstream conditions. It was later shown by Cowley [1982] that although both processes could contribute to magnetospheric convection, the dominant process is the reconnection-driven Dungey Cycle.

2.1.1 Quantifying the Rate of Reconnection

The original theory for magnetic flux circulation by Dungey [1961] proposed a steady-state process wherein reconnection at the dayside magnetopause and in the magnetotail occurs at the same rate. However, dayside reconnection is driven by properties of the IMF and solar wind upstream, as will be discussed in Section 2.1.2, and nightside reconnection is governed by conditions in the magnetotail. Although conditions in the magnetospheric lobes can be influenced through the addition of open flux during prolonged dayside reconnection, there is inevitably some time delay due to the propagation of those flux tubes anti-sunward, and as such the rate of reconnection can vary between the dayside and nightside. If the reconnection rate is greater on the dayside then the magnetopause will be eroded planetward and the total open flux content of the magnetosphere increases. Conversely, the open flux decreases when nightside reconnection dominates. The state of the magnetosphere at any given time therefore depends strongly on the relative strength of reconnection at each location, and in order to understand this a method for quantifying the rate of reconnection is required.

Direct observations of reconnection are difficult to obtain as the spacecraft needs to be located exactly at the reconnection site, however various parameters external to the diffusion region can be used to provide an estimate of reconnection rates. The simplest forms of these estimates exist as dimensionless ratios of either the flow velocities or magnetic field components. Petschek [1964] defined the reconnection rate as V_{in}/V_A, comparing the inflow velocity (V_{in}) of plasma towards the reconnection X-line to the outflow speed, given by the Alfvén velocity, V_A:

$$V_A = \frac{B}{\sqrt{\mu_0 \rho}}, \tag{2.1}$$

where ρ is the plasma density in the inflow region. The velocity ratio used by Petschek [1964] requires antiparallel magnetic fields of equal magnitude, and yields values of 0.1-0.2 for the reconnection rate [Sonnerup, 1974]. Similar values have been observed at the dawn magnetopause by Phan *et al.* [2001], although several authors have reported values considerably lower than 0.1 [e.g. Phan *et al.*, 1996; Fuselier *et al.*, 2005].

Sonnerup *et al.* [1981] proposed an alternative to the method of using reconnection jet velocities to calculate a reconnection rate by considering the geometry of a reconnection event. At an X-line, where the field diffuses across the current sheet, the magnetic field orientation changes from one parallel to the magnetopause boundary to one with a significant normal component. The reconnection rate can therefore also be defined using the strength of the magnetic field component along the outward normal to the magnetopause relative to the total field strength just inside the magnetopause, B_N/B_{MSp}, yielding a value of ~ 0.1.

Although the above methods yield similar values, there are difficulties associated with both. The average inflow velocity of ~ 25 km s^{-1} is comparable to the velocity of the moving magnetopause [Phan & Paschmann, 1996], making accurate measurements of V_{in} difficult to obtain. Additionally, determining the inflow velocity requires a well-defined magnetopause normal, which is difficult given the fluctuations in field strength and orientation near a moving magnetopause. Further biases may be introduced to the reconnection rate as determined from magnetic field components by only obtaining B_N on occasions where the normal component is large enough to be accurately measured.

2.1.2 Conditions Influencing Reconnection

The polar cap defines the area of the polar ionosphere containing open magnetic flux, and its size therefore changes as reconnection rates at the dayside magnetopause and in the magnetotail vary. Several authors have described the temporal variations in polar cap size as a function of differing dayside and nightside reconnection rates [e.g. Cowley, 1982; Siscoe & Huang, 1985; Milan *et al.*, 2007]. Numerous functional forms have been proposed to quantify dayside reconnection as a function of a range of upstream properties. The most critical property is the clock angle of the IMF, as seen by Fairfield & Cahill [1966] and Perreault & Akasofu [1978], who observed interaction between the Earth's magnetosphere and the solar wind primarily when the IMF was oriented southward.

The reconnection rate described by the ratio of inflow velocity to Alfvén velocity was suggested by Petschek [1966] and Russell & Atkinson [1973] to vary as $\sin(\theta/2)$, where θ is the magnetic shear angle across the magnetopause. For reconnection near the subsolar point, where the magnetospheric field is directed northward, this is equivalent to the IMF clock angle. When considering the reconnection electric field, however, a range of different relationships have been suggested for the effect of the IMF clock angle. Milan *et al.* [2012] fitted a functional form to observations of the polar cap boundary and determined a dependence of $\sin^{9/2}(\theta/2)$, whereas Sonnerup [1974] established the upper limit on the rate of reconnection to be proportional to $\sin^2(\theta/2)$. However, this upper limit applies only in the case of symmetric reconnection, where the plasma density and magnitude of the magnetic fields are equal on either side of the boundary.

When the field strength and plasma density vary considerably across the current sheet, asymmetric reconnection occurs. Simulations by Cassak & Shay [2007] and Pritchett [2008] have shown that in such scenarios the rate of reconnection is 2-3 times lower than for symmetric reconnection. This has important implications for magnetopause reconnection rates at different planets, as the higher IMF strength and lower Alfvén Mach number in the inner Solar System leads to more symmetric conditions at Mercury than the outer planets, therefore enabling reconnection at a greater range of clock angles. Slavin & Holzer [1979] predicted that the low Alfvén Mach number, and low plasma beta, at Mercury would result in significantly higher reconnection rates than seen at Earth, and more recently Masters *et al.* [2012] have shown that the high beta magnetosheath at Saturn inhibits reconnection unless the fields are anti-parallel.

The effects of different values of plasma beta have also been observed at Earth by Phan *et al.* [2013], who observed reconnection across a wide range of magnetic shear angles for magnetopause crossings with a low $\Delta\beta$, whereas only high-shear reconnection was observed when there was a large gradient in β across the magnetopause. This is in agreement with earlier work by Swisdak *et al.* [2003], who showed that the X-line can advect along the magnetopause at the electron diamagnetic drift velocity. As the electrons and ions drift in opposite directions, if the relative drift velocity approaches V_A, fast ion outflow from the diffusion region will not be possible on one side of the X-line and reconnection is suppressed. For a sufficiently large pressure gradient, the drift velocity becomes high enough that only anti-parallel fields are able to reconnect.

2.1.3 X-line Location and Orientation

When the conditions are suitable for reconnection, the process does not necessarily occur at a fixed position on the magnetopause. Instead, reconnection can take place along an extended X-line, the orientation and location of which varies with clock angle. During intervals of northward IMF, the X-line is located on the magnetospheric lobes, anti-sunward of the cusp, where the draping of the IMF results in anti-parallel fields [Dungey, 1963]. For southward IMF, reconnection occurs near the sub-solar point, but the X-line can extend a significant azimuthal distance away from this point in both directions. Measuring the length is extremely difficult due to the need for multiple spacecraft observing reconnection at the same time across a wide range of magnetic local times (MLT), however Walsh *et al.* [2014] observed two reconnection events linked to the same X-line, separated by 1.5 h in MLT, and Dunlop *et al.* [2011] reported sub-solar reconnection events consistent with an X-line that extended $\sim 9\ R_E$.

Although the X-line lies primarily azimuthally, passing through the subsolar point, during southward IMF reconnection, its location and orientation are less clearly defined when the IMF has a significant B_Y component. In this instance, if reconnection proceeds in regions of anti-parallel fields, two separate X-lines will form. In the case of positive B_Y, reconnection will take place duskward of the northern cusp and dawnward of the southern cusp, and vice versa for negative B_Y [Crooker, 1979]. Alternatively, component reconnection could take place, whereby reconnection is initiated at the subsolar point and propagates away continuously along the dayside magnetopause to produce an X-line that maps the position of maximum magnetic shear [e.g. Sonnerup, 1970; Gonzalez & Mozer, 1974].

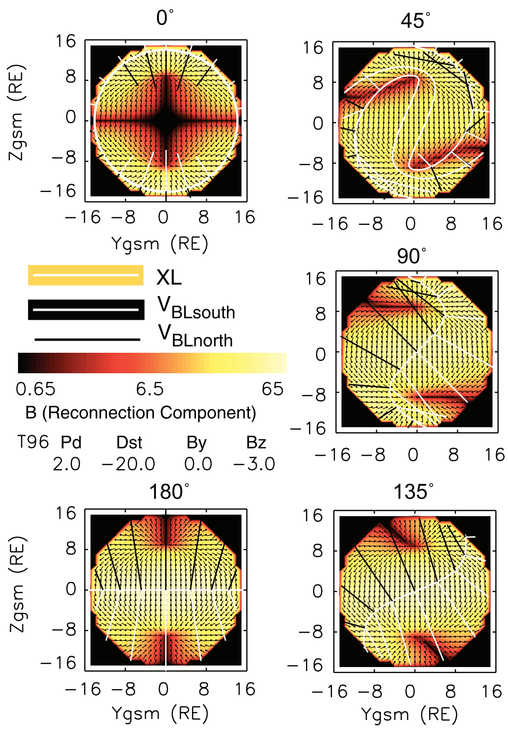

Figure 2.1: Flow direction, field configuration and X-line orientation for a range of magnetosheath clock angles. The small black arrows show the magnetospheric field direction just inside the magnetopause, the continuous white line indicates the X-line, and the white and black vectors represent the flow direction for newly reconnected boundary layer magnetic field lines. The colour scale indicates the magnitude of the reconnecting component, as defined in the text. Figure from Moore *et al.* [2002].

Moore *et al.* [2002] calculated the expected orientation of the X-line using component reconnection for a range of clock angles, as shown in Figure 2.1. During southward IMF, as indicated in the bottom left panel, the X-line lies in the equatorial plane, passing through the subsolar point, but as the Y-component increases there is a clear poleward rotation of the X-line in the dusk sector. The opposite is true for negative B_Y, although this is not shown here. The resultant flow vectors in the magnetopause boundary layer change from near-poleward in the case of a horizontal X-line to have a significant component directed towards the flanks of the magnetosphere as the clock angle decreases from 180° to 45°, until for northward

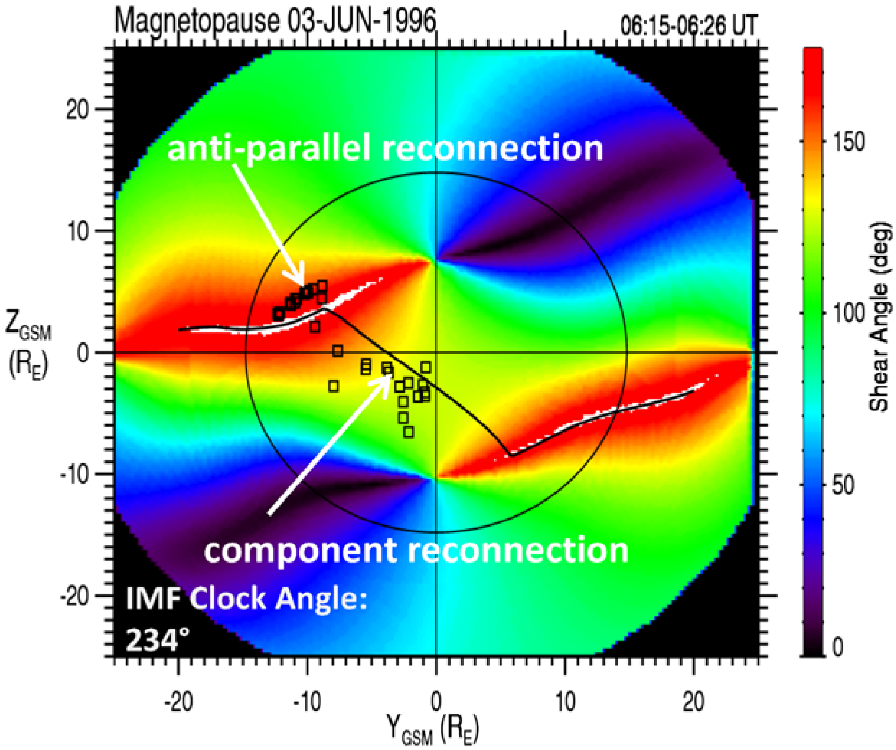

Figure 2.2: Observed locations of reconnection, indicated by black squares, and the modelled magnetic shear at the magnetopause, indicated by the colour shading. Red indicates regions of high magnetic shear, and the white line traces locations where the shear is 180° ± 3°. The black line marks the largest magnetic shear, and therefore represents the tilted component reconnection line. Figure from Fuselier & Lewis [2011], adapted from Trattner *et al.* [2007].

IMF the X-line forms a closed circle passing near the cusps and the reconnected flow vectors point equatorward. The reconnection component represented by the colour scale of the plots is defined as the magnitude of the dot product of the boundary layer magnetic field with the unit vector normal to the X-line.

Trattner *et al.* [2007] observed reconnection events in locations that in general were in agreement with the component reconnection model that produces an extended X-line across the magnetopause, as shown in Figure 2.2. Reconnection locations are observed in both the anti-parallel region on the dawn side, and along a tilted component X-line near the subsolar point. During periods where the IMF had a strong sunward or anti-sunward component, reconnection was found to favour the anti-parallel model at high latitudes.

2.1.4 Magnetospheric Flows

Following reconnection at the dayside magnetopause, the newly-opened magnetic flux is transported across the pole of the planet into the magnetotail. As this convection represents a large contribution to the Dungey cycle of magnetic flux, the nature of the dayside magnetospheric flow is crucially important in describing the state and conditions of the magnetosphere. Assuming a stagnation point exists at the subsolar point, the magnetosheath flow will propagate radially outwards from this point in the magnetopause plane, but magnetic tension due to the presence of kinked magnetic field lines following reconnection distorts this simple picture. The relative importance of the radial flow and magnetic tension depends on the velocity of the magnetosheath plasma [Cowley & Owen, 1989]. When the Alfvén Mach number in the magnetosheath is low, magnetic tension will dominate, whereas for high Mach numbers the magnetosheath flow is dominant.

In the case of anti-parallel reconnection at the subsolar point, the magnetosheath flow and magnetic tension force both act poleward, such that the newly-opened flux tube travels directly over the polar cap in the noon-midnight plane. However, away

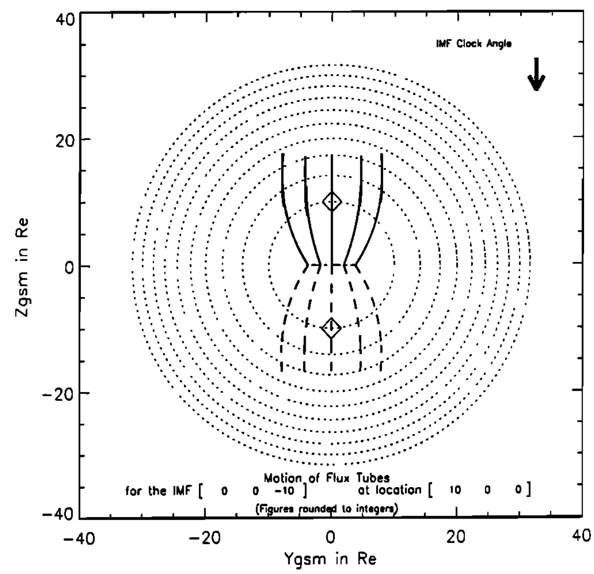

Figure 2.3: Motion of flux tubes following reconnection at an extended X-line passing through the subsolar point during southward IMF. Flux tubes connected to the northern hemisphere are shown in solid black lines, and dashed lines mark the motion of flux tubes connected to the southern hemisphere. The diamonds mark the location of the magnetospheric cusps. Figure from Cooling *et al.* [2001].

from local noon, the radially-directed magnetosheath flow acts perpendicularly to the initial meridional tension force, creating a Y-component in the open field flow direction [e.g. Crooker *et al.*, 1984; Cowley & Owen, 1989].

Cooling *et al.* [2001] constructed a model to describe the motion of flux tubes across the magnetosphere, under a variety of IMF conditions. The simple case of southward IMF and reconnection at an extended X-line passing through the subsolar point is shown in Figure 2.3. The solid lines indicate the motion of flux tubes that are anchored in the northern hemisphere, and whose footprints therefore move anti-sunward over the northern polar cap, whilst dashed lines show the motion of open flux tubes connected to the southern hemisphere.

At local noon, the flux tubes move directly anti-sunward, over the polar regions and into the magnetotail with their motion constrained to the noon-midnight meridian. Flux tubes opened by reconnection away from the subsolar point, however, exhibit some azimuthal motion due to the draping of the IMF just outside the curved magnetopause. The resultant flow pattern is symmetric both in the equatorial plane and around local noon.

When the IMF clock angle is not exactly 180°, however, such that the reconnecting fields are not anti-parallel and the X-line is tilted, the motion of the newly-opened flux tubes becomes more complicated. The magnetic shear angle across the magnetopause results in a tension force that points neither along the magnetospheric field nor the IMF direction, but rather somewhere between the two. Consequently, flux tubes passing through the subsolar point experience magnetic tension that does not align with the magnetosheath flow at that point, and the subsequent motion therefore has a dawn-dusk component, unlike in the case of anti-parallel reconnection.

Figure 2.4 shows the motion of a series of flux tubes opened by reconnection along an X-line that is tilted due to the 135° IMF clock angle. Flux tubes opened at the subsolar point do not travel directly poleward due to the dawn-dusk component of the magnetic tension force dominating over the magnetosheath flow. Newly-reconnected flux tubes at some distance from local noon along the tilted X-line exhibit asymmetries in their motion, contrary to the simple case of anti-parallel reconnection in Figure 2.3. At the dawnward edge of the X-line, the flux tube

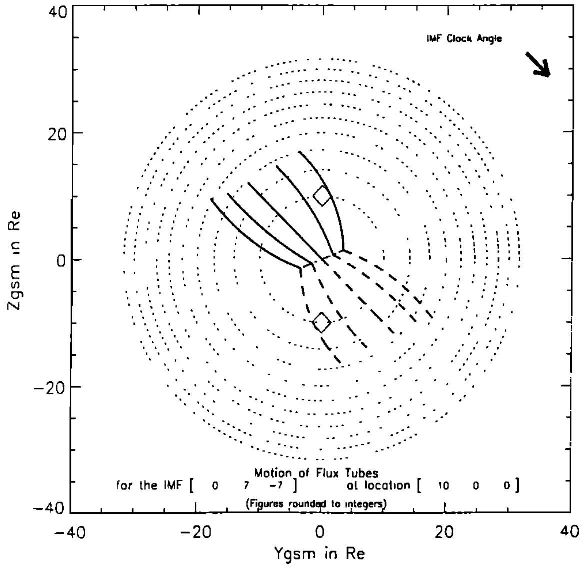

Figure 2.4: Motion of flux tubes following reconnection between magnetospheric field and IMF at a clock angle of 135° along a tilted X-line. The format is the same as in Figure 2.3. Figure from Cooling *et al.* [2001].

connected to the northern hemisphere (shown as a solid line) initially moves predominantly dawnward due to the radial magnetosheath flow and the dawnward component of the magnetic tension force. As the flux tube moves further north under magnetic tension, the radial magnetosheath flow also provides an additional northward acceleration, producing the observed path. Conversely, the duskward tension force opposes the radial magnetosheath flow for the flux tube connected to the southern hemisphere, such that its initial motion is roughly poleward. The radial flow therefore becomes less dawnward, resulting in a greater net duskward component to the motion. A similar effect occurs at the dusk edge of the X-line, producing the asymmetric flow pattern shown.

2.2 Flux Transfer Events

The quasi-steady state reconnection process discussed above sequentially creates pairs of open flux tubes at the dayside magnetopause, where one of the pair is connected to each magnetospheric polar region. Such reconnection can be identified on the basis of magnetic field components normal to the magnetopause [Sonnerup & Cahill, 1967], observations of plasma jets accelerated away from the reconnection site [Paschmann *et al.*, 1979], or more recently, direct encounters with the electron diffu-

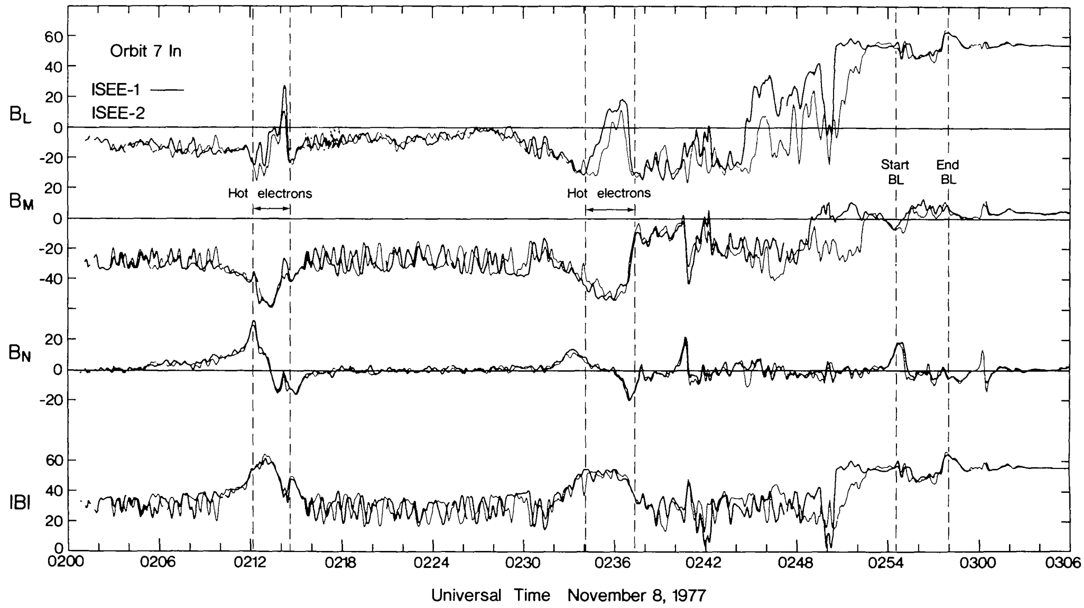

Figure 2.5: Magnetometer data from the ISEE-1 and ISEE-2 spacecraft shown in boundary normal coordinates. ISEE-1 data are shown with the dark line, and the light line indicates ISEE-2 data. Flux transfer events are observed at 0212 and 0236 UT. Figure from Russell & Elphic [1978].

sion region by satellite constellations such as Magnetospheric Multiscale (MMS) [e.g. Fuselier *et al.*, 2017]. However, signatures of reconnection have also been observed in the form of more complex magnetic structures known as flux transfer events (FTEs).

The first observations of FTEs were made by Russell & Elphic [1978] in International Sun-Earth Explorer-1 and 2 (ISEE) magnetometer data. The data are presented in Figure 2.5 in boundary normal coordinates. The increase in the B_L and $|B|$ components near 0212 and 0236 are indicative of brief entries into the magnetosphere, however the accompanying B_M and B_N signatures complicate this interpretation. The bipolar signature in B_N suggests that the spacecraft have encountered a bulge on the magnetopause, verifying the partial entry into the magnetosphere suggested by the B_L increase. However, just inside the magnetopause the B_M component is very close to zero, whereas at the two events shown there is a strong increase in B_M, indicative of magnetosheath field. FTEs have been observed to have a helical magnetic field inside the flux rope [Paschmann *et al.*, 1982], implying a magnetic flux rope-like structure. The signatures are then consistent with a flux rope moving perpendicular to its axis in a poleward and anti-sunward direction as a result of magnetic tension and magnetosheath flow, transporting magnetic flux into the magnetotail.

2.2.1 Formation Mechanisms for FTEs

Russell & Elphic [1978] postulated that the FTE signature first identified in ISEE data could be explained by patchy reconnection generating a kinked flux tube, that is then pulled out of the plane of the magnetopause once reconnection has ceased. As it is straightened out by magnetic tension, magnetosheath field is gathered around the flux rope, draping around it to create a bulge that produces the observed bipolar signature in B_N. Due to the requirement of reconnection at a single X-line, this model intrinsically results in the formation of a pair of flux ropes. One of the FTEs will be connected to, and therefore accelerated towards, the northern magnetic pole, whilst the other is similarly linked to the southern magnetic pole. Sonnerup [1987] suggested that the helicity of the magnetic field within the flux transfer event could be explained by the interaction of the flux rope with the magnetospheric field creating a current flowing along the axis of the FTE, that in turn generates a helical field.

An alternative formation mechanism was proposed by Lee & Fu [1985], invoking multiple X-lines. In the simplest case, reconnection is initiated at two extended parallel X-lines. Considering a series of open field lines generated at an X-line and connected to the northern hemisphere, subsequent reconnection along a parallel X-line at higher latitudes will close the open flux into a helical structure that forms between the two X-lines. For purely anti-parallel reconnection, however, a series of isolated magnetic loops or islands is produced. The magnetic field in the current sheet between the reconnecting magnetospheric and magnetosheath fields in this model therefore requires a component in the azimuthal direction, in the form of a *guide field*, in order to produce a flux rope structure. More generally, this model allows reconnection at n parallel X-lines, resulting in the formation of $n - 1$ FTEs.

Southwood *et al.* [1988] and Scholer [1988] independently proposed a third mechanism for the formation of FTEs, requiring reconnection at a single X-line. The requirement in this model is that the rate of reconnection is time-variable. A sudden increase in the rate of reconnection will heat the plasma inside the kink of the open flux, increasing its thermal pressure and causing an outward bulge in the magnetic field. A subsequent reduction in the reconnection rate reduces the angle between the reconnected field and the magnetospheric field, resulting in a spatially-limited bulge that propagates poleward. An internal core field component parallel to the X-line can be generated by magnetic shear that is not anti-parallel. Because of the single X-line, a pair of FTEs will always be produced by this model, as is the case with the 'elbow' FTE formed by the Russell & Elphic [1978] model.

A schematic of all three formation mechanisms is shown in Figure 2.6, from Fear *et al.* [2008]. Black arrows represent unreconnected magnetospheric field lines, and the unreconnected magnetosheath field is shown in red with a magnetic shear angle of 150°. The blue lines indicate reconnected field lines, and the edge of the FTE in each case is marked in green. The top row shows the field configuration for each model viewed along an axis normal to the magnetopause, whilst the bottom row

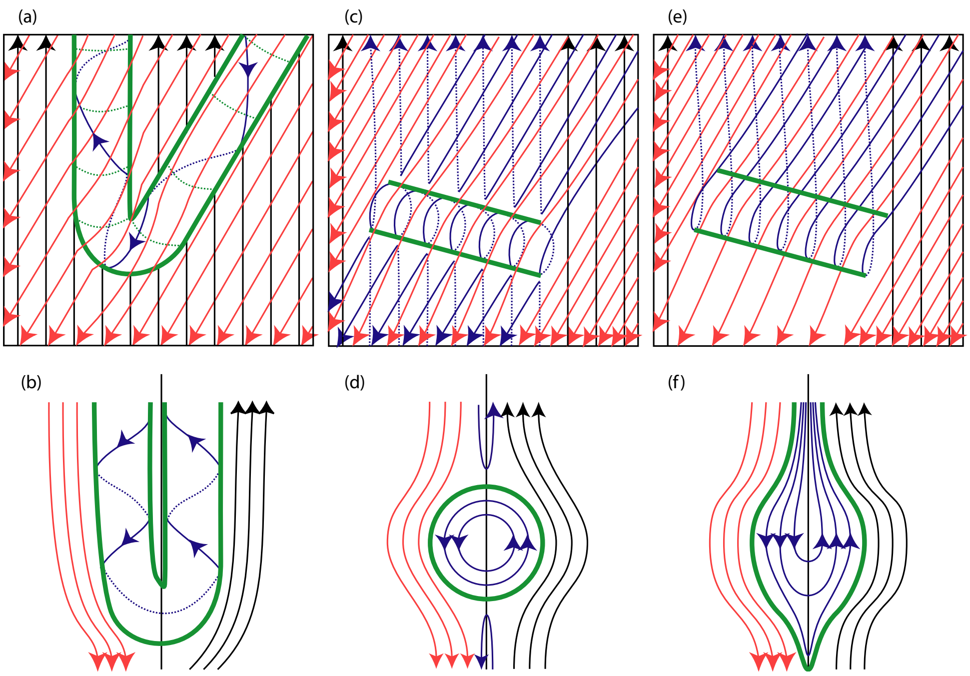

Figure 2.6: A schematic showing how an FTE is formed by each of the three mechanisms. The top row show magnetic field configurations in the plane of the magnetopause, and the bottom row is viewed along a magnetopause tangent. Panels (a) and (b) show the Russell & Elphic [1978] 'elbow' model, the Lee & Fu [1985] multiple X-line model is indicated in panels (c) and (d), and the single X-line model of Southwood *et al.* [1988] and Scholer [1988] is shown in panels (e) and (f). Magnetospheric and magnetosheath field lines are denoted by the black and red arrows respectively, whilst blue lines indicate magnetic field lines that have reconnected. The edge of the FTE in each case is marked in green. Figure from Fear *et al.* [2008].

is viewed along a tangent to the magnetopause, with the boundary itself indicated by the vertical black line. The Russell & Elphic [1978] highly kinked ‘elbow’ model of an FTE is shown in panels (a) and (b) to have a component of its axis aligned vertically on both sides of the magnetopause, whereas the Lee & Fu [1985] FTE in panels (c) and (d), and the single X-line model of Southwood *et al.* [1988] and Scholer [1988] in panels (e) and (f) have their axis aligned parallel to the X-line. In panels (c) and (d), pairs of open field lines are seen either side of the helical FTE, where in this case the green lines also mark the locations of the parallel X-lines. The bulge caused by heated plasma in bursty reconnection single X-line model is clearly visible in Figure 2.6f.

It has since been shown that the original proposal by Russell & Elphic [1978] is unlikely to produce the observed signatures of FTEs, however observations indicate that both other mechanisms may be responsible for generating FTEs at the dayside magnetopause [e.g. Fear *et al.*, 2008; Trenchi *et al.*, 2016].

2.2.2 Determining the Structure and Orientation of FTEs

Although the multiple X-line and bursty reconnection single X-line models result in the formation of FTEs with distinct magnetic topologies, as seen in Figure 2.6, they produce signatures in boundary normal magnetic field data that are almost indistinguishable. An FTE moving northwards along the magnetopause close to its formation site will produce a positive-to-negative (standard polarity) bipolar signature in the normal component of the magnetic field as it passes over a spacecraft [Russell & Elphic, 1978]. Conversely, a southward-moving FTE will produce a reverse polarity, negative-to-positive, bipolar signature, assuming in both cases that the FTE axis is aligned predominantly azimuthally. The axially-aligned core field in the centre of the FTE will therefore produce an enhancement in B_M. Additional signatures of FTEs can be observed in measurements from the interior of the flux ropes, where plasmas of both magnetospheric and magnetosheath origin are seen [Paschmann *et al.*, 1982], reflecting the mixing of populations on interconnected field lines.

Whilst the above scenario of an FTE with its axes aligned closely with magnetopause boundary normal coordinates is often applicable for events observed close to a formation site near the subsolar point, it is not always the case for flux ropes formed away from this location or observed some distance away from where they form. A tilted X-line will naturally lead to a core field that is also tilted with respect to the M direction, and motion of the FTE as a result of magnetosheath flows or magnetic tension forces can also cause rotations out of the magnetopause plane. A more general approach is therefore required to calculate the orientation of FTEs at all locations in the dayside magnetosphere.

Multi-spacecraft timing analysis [e.g. Schwartz, 1998] has been used on observations from the Cluster [e.g. Fear *et al.*, 2005] and MMS [e.g. Eastwood *et al.*, 2016; Dong *et al.*, 2017] missions to constrain the size and orientation of FTEs, and their velocity past the spacecraft. When only one spacecraft has observed an FTE signature, however, it is difficult to accurately determine the FTE structure. Minimum variance analysis (MVA) of the magnetic field [Sonnerup & Cahill, 1967; Sonnerup & Scheible, 1998] can therefore be used to estimate the principal axes of a flux rope. From a time series of magnetic field data, the directions of maximum, intermediate, and minimum variance of the field are calculated, however there has been some debate about which axis best represents the core direction of an FTE.

Sibeck *et al.* [1984] found that for flux ropes in the Earth's magnetotail, encountered close to the centre of the flux rope, the large amplitude of the core field meant that the axis was best described by the maximum variance direction. However, using observations of plasmoids made by the International Sun-Earth Explorer (ISEE 3) spacecraft in the magnetotail, Slavin *et al.* [1989] found that the axial direction was best described by the intermediate variance direction, as shown in Figure 2.7, due to the weak core field. In modelling the draping of magnetic fields around a flux rope, Farrugia *et al.* [1987] found that the component of the draped field along the flux rope axis was constant, so in this instance the minimum variance direction would lie either parallel or antiparallel to the axis.

These conclusions are supported by Xiao *et al.* [2004], who modelled flux ropes encountered by a single spacecraft and found that when the spacecraft remains outside the flux rope the minimum variance direction provides the best estimate

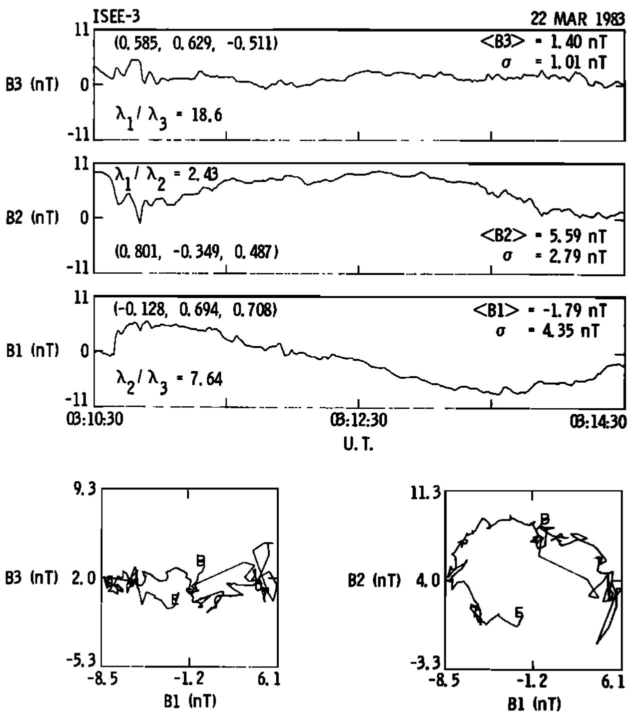

Figure 2.7: A time series of ISEE 3 magnetometer data showing a plasmoid passing over the spacecraft. The data are shown in the directions of minimum (B_3), intermediate (B_2) and maximum (B_1) variance. The core field is visible in the intermediate variance direction. The bottom two panels show hodograms of the minimum-maximum and intermediate-maximum variance direction, with a clear rotation visible in the $B_2 - B_1$ hodogram, evidence for the flux rope structure. Figure from Slavin *et al.* [1989].

of the axial direction. For a magnetic force-free flux rope, like those observed by Slavin *et al.* [1989], the intermediate variance direction lies closest to the true axis of the flux rope, although there may be a difference of up to 20° between the two directions. The best descriptor of the axial direction for a non-force free flux rope, with a large axis-aligned current, depends on the *impact parameter* of the encounter, defined as the closest distance between the spacecraft trajectory and the axis of the flux rope. For small impact parameters, Xiao *et al.* [2004] found that the maximum variance direction was the closest match to the flux rope axis, but the intermediate variance direction provides the best estimate for large impact parameter encounters with force-free flux ropes.

2.2.3 Review of FTE Observations at Earth

Since the first observation by Russell & Elphic [1978], flux transfer events have been seen across the dayside magnetosphere at Earth, during a range of IMF conditions. Rijnbeek *et al.* [1984] conducted a survey of FTEs identified by the ISEE-1 and ISEE-2 spacecraft both in the magnetosheath and inside the magnetopause, and found that in both locations the majority of events seen in the northern hemisphere had a standard bipolar signature in the magnetic field component normal to the magnetopause (B_N), indicating that they were travelling northwards. Conversely, most southward-moving events were seen in the southern hemisphere or close to the equatorial plane. Furthermore, a strong magnetosheath B_Z dependence was seen in observations of FTEs. The vast majority of FTEs were seen during intervals when the IMF had a negative Z-component, and of the 61 magnetopause crossings where no events were identified only 5 occurred during southward-directed IMF. The conclusions were therefore twofold: not only are FTEs observed predominantly whilst the magnetosheath field has a southward component, but when such an orientation is present it is rare for FTEs not to be seen.

The first part of this result was confirmed by [e.g. Berchem & Russell, 1984; Kawano & Russell, 1997b], who identified FTEs almost exclusively during southward IMF intervals. However, Berchem & Russell [1984] observed events on only $\sim 25\%$ of passes, although this rises to 45% when the IMF has a southward component. The location of the identified FTEs again showed a clear ordering by direct or reverse bipolarity. Figure 2.8 shows the distribution of both types of event in the Geocentric Solar Magnetospheric (GSM) $Y - Z$ plane, where the GSM coordinate system is oriented similarly to the MSM system, but centred instead on Earth. Most of the events in the northern hemisphere are travelling northwards, and conversely in the southern hemisphere. The exception is at southern dawn, where FTEs have a standard bipolar signature. However, during the period examined here, there was a duskward bias in the IMF, leading to an anti-clockwise rotation of the dayside reconnection X-line, such that those events are still moving northwards away from the reconnection site. The inset at the top of Figure 2.8 shows the occurrence of FTEs with IMF orientation, normalised by the number of magnetopause crossings

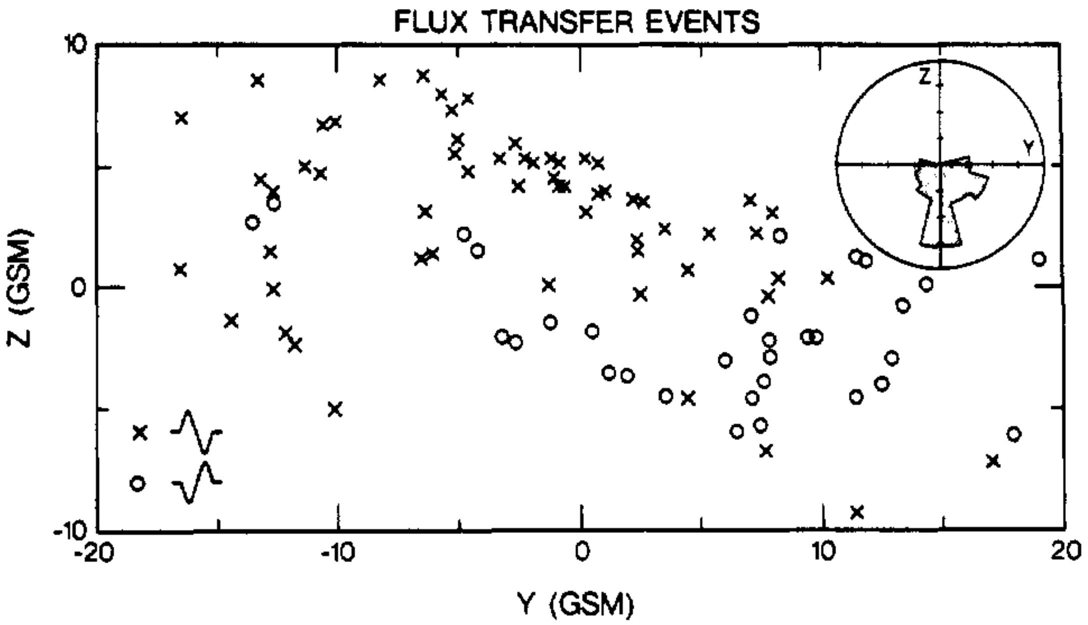

Figure 2.8: The location and polarity of FTE signatures seen in ISEE-1 and ISEE-2 data, shown in the GSM $Y - Z$ plane. Standard polarity FTEs are denoted by a cross, whereas an open circle indicates reverse polarity. The majority of events in the northern hemisphere have a standard bipolar signature, indicating they are moving northwards, whilst the opposite is true in the southern hemisphere. The inset shows the occurrence of FTEs with IMF clock angle, normalised by the number of magnetopause crossings during each orientation. Figure from Baumjohann & Paschmann [1987], adapted from Berchem & Russell [1984].

during each orientation.

The rotation of the line dividing northward- and southward-moving FTEs that indicates a tilted X-line was also observed by Korotova *et al.* [2012], in a study of Interball-1 data. By separating the FTEs into those seen during either duskward ($B_M < 0$) or dawnward ($B_M > 0$) magnetosheath field, they inferred a tilting of $\sim 45°$ in both cases, as shown in Figure 2.9. Such a tilting suggests that component reconnection is important at the subsolar magnetopause, although a strong tendency for events to occur during southward IMF was again seen.

Further away from the subsolar magnetopause, however, the southward preference is not so clear. FTEs on the flanks of the magnetosphere were observed during both northward and southward magnetosheath fields, indicating two possible origins for these events. Korotova *et al.* [2012] suggested that these FTEs were consistent with formation either through component reconnection along an extended X-line that passes through the subsolar point for all IMF orientations, or through a combination of component reconnection along a subsolar X-line and anti-parallel

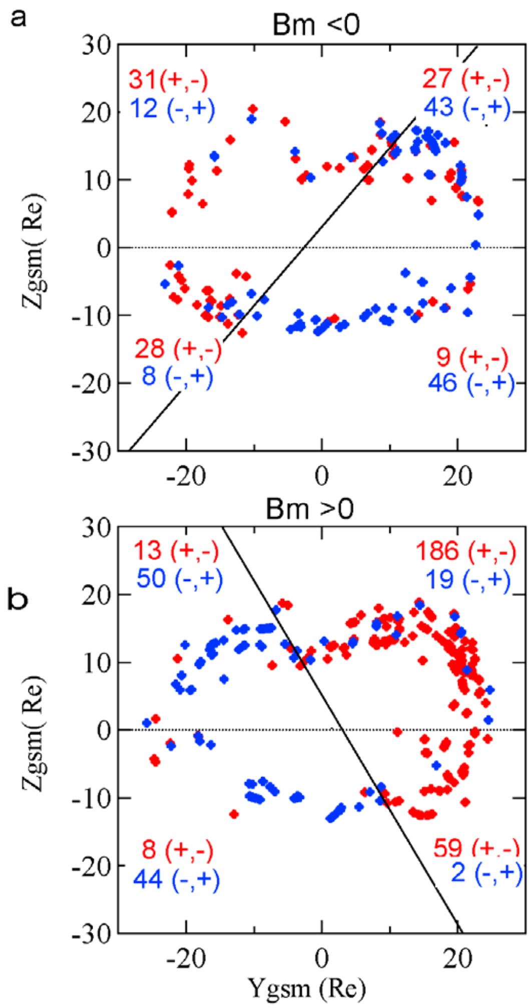

Figure 2.9: The locations of FTEs encountered in the magnetosheath by Interball-1, projected onto the GSM $Y - Z$ plane. Red points indicate standard polarity FTEs, and blue denote reverse polarity. The events are split into those seen whilst the magnetosheath field had a duskward ($B_M < 0$) and dawnward ($B_M > 0$) component. A reconnection X-line is indicated by the tilted solid black line. The numbers given in the corners of each panel indicate the number of events in each sector bounded by the equator and the X-line. Figure from Korotova *et al.* [2012].

reconnection at high latitudes during northward IMF. The latter had previously been proposed by Kawano & Russell [1997a], and Fear *et al.* [2005] calculated velocities of FTEs seen near the magnetopause flanks by the Cluster spacecraft that were in agreement with high-latitude reconnection producing FTEs that then move equatorward as a result of super-Alfvénic flow at the X-line.

FTEs have also been observed near the magnetospheric cusps during both northward and southward IMF. Sibeck *et al.* [2005] attributed the events seen in the cusps to poleward motion of FTEs formed near the subsolar magnetopause during southward IMF. FTEs seen poleward of the cusp showed no clear dependence on IMF orientation, indicating that they comprise a combination of events formed at the subsolar magnetopause during southward IMF that then move poleward, and locally-generated FTEs formed by bursty anti-parallel reconnection poleward of the cusp during northward IMF.

The motion of FTEs generated at low latitude was investigated by Sibeck & Lin [2010, 2011] for a range of IMF clock angles. Using the Cooling *et al.* [2001] model for tracing flux tube motions, Sibeck & Lin [2010] generated a series of FTEs at 1 R_E intervals along a reconnection line passing through the subsolar point, an example of which for duskward IMF is shown in Figure 2.10. The subsequent locations of each of these events are shown every 100 s, and the FTEs are seen in this case to move northward and dawnward, or southward and duskward, depending on the hemisphere to which they are connected. In the case of southward IMF, FTEs were generated along an equatorial X-line and moved rapidly anti-sunward over the polar regions of both hemispheres, whereas a northward component in the IMF resulted in a strongly tilted X-line, producing FTEs that propagate slowly around

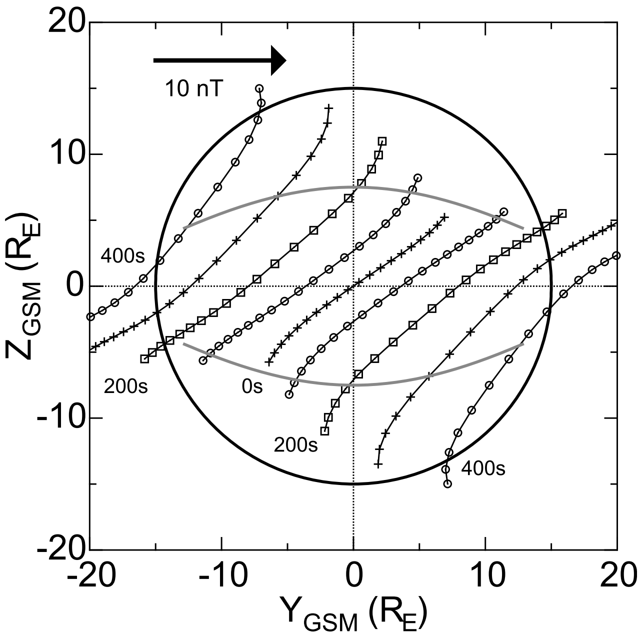

Figure 2.10: Modelled motion of FTEs away from a tilted reconnection line passing through the subsolar point. Crosses, circles and squares on the lines show the location of points separated initially by 1 R_E, at 100 s timesteps. The orientation and strength of the IMF is indicated by the large black arrow. Figure from Sibeck & Lin [2010].

the magnetospheric flanks. In all cases, the FTEs retained an orientation very close to that of the initial reconnection line along which they formed. This result was also seen in Cluster data by Fear *et al.* [2012a], who estimated the axial orientation of FTEs to lie approximately azimuthally, as would be expected for high magnetic shear reconnection.

Other factors influencing the location of FTEs at Earth, in addition to the IMF clock angle, have also been investigated [e.g. Kuo *et al.*, 1995]. Both the upstream and downstream β were found to have no significant control over the formation of FTEs, as was the upstream dynamic pressure of the solar wind. However, Kuo *et al.* [1995] found that FTEs were observed with a higher probability when the upstream magnetosonic Mach number was lower, albeit with only a weak effect.

Kawano & Russell [1996] surveyed 1246 FTEs identified in ISEE-1 data, and found that the majority of events were seen within $1R_E$ of the magnetopause, although some are seen several R_E away from the magnetopause on both sides of the boundary. Additionally, the FTEs encountered closest to the magnetopause have a higher peak-to-peak amplitude of the bipolar signature than those seen further away, with only the longest duration events being observed deep into the magnetosphere, suggesting that the smallest FTEs decay more rapidly with increasing distance from the magnetopause.

The nature of the bipolar signature was also analysed by Fear *et al.* [2010], to investigate asymmetries in the B_N component of 213 FTEs identified at high latitude or on the magnetospheric flanks by all four Cluster spacecraft. Figure 2.11 shows an example of the magnetic field signature of an FTE observed at each of the four spacecraft. Fear *et al.* [2010] applied a low-pass filter to the B_N trace, and calculated the regions where the amplitude exceeded 25%, 50%, and 75% of the maximum amplitude of that peak. In all three width measurements, they found the trailing peak to have a longer duration for the majority of signatures, but the amplitude of the leading peak is larger than that of the trailing peak. This was attributed to a compression of magnetic flux at the leading edge of the FTE, and a rarefaction behind it. The interpretation is supported by the asymmetries being less clear for FTEs seen close to the subsolar point, where the magnetosheath flow speed is lower.

2.3 The Mercury System

The planet Mercury is both the smallest planet in the Solar System, and the closest to the Sun. As will be discussed in the following sections, it is also in many ways anomalous amongst the terrestrial planets, and therefore represents a fascinating testing ground for the understanding of planetary physics. Despite being one of the Earth's closest neighbours, Mercury's proximity to the Sun makes it a challenging destination for spacecraft, such that only 2 spacecraft have so far visited the planet, although the BepiColombo mission [Benkhoff *et al.*, 2010], launched in October 2018, will insert two spacecraft into orbit around Mercury in 2025. In 1974-75, Mariner 10 performed 3 fly-bys, providing the first in-situ observations of the surface and space environment, but it was not until 2011 that MErcury Surface, Space ENvironment,

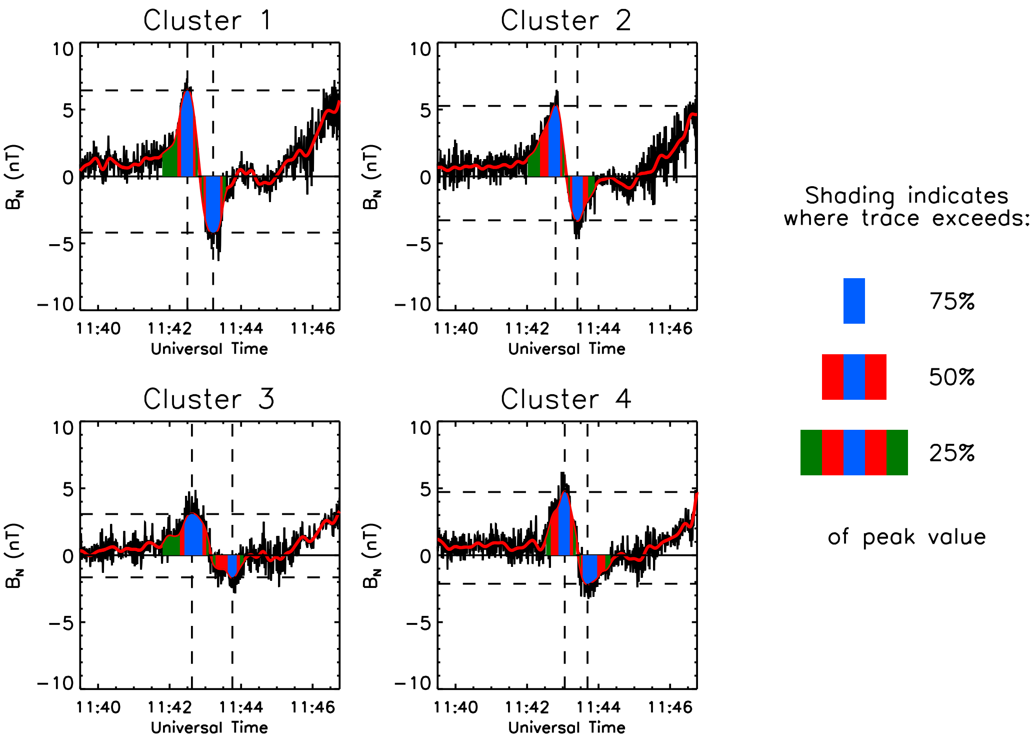

Figure 2.11: The B_N signature of an FTE seen by all four Cluster spacecraft. The black lines show the observed B_N, and the trace after applying a low-pass filter is overplotted in red. For each peak, the regions where the amplitude exceeds a quarter-/half-/three-quarters of the maximum amplitude are shown in green/red/blue. Figure from Fear *et al.* [2010].

GEochemistry and Ranging (MESSENGER) [Solomon *et al.*, 2007] became the first orbiting spacecraft around Mercury, remaining in orbit until 2015. Further details of this mission and its instrumentation will be discussed in Chapter 3.

Despite being the lightest planet, with a mass of 3.3×10^{23} kg, in addition to the smallest, with a radius (R_M) of 2440 km, Mercury's density is higher than all other planets except Earth. This is due to the large molten metal core, which extends to a radius of 2020 ± 30 km [Hauck *et al.*, 2013], thereby occupying a significantly larger fraction of its planet than any other planetary cores do.

Mercury rotates extremely slowly, such that a sidereal day lasts 58.65 Earth days. This long rotation period means Mercury is the only planet with a spin-orbit resonance of 3:2, as one year on Mercury lasts 88 days. A further consequence of the slow rotation, combined with the short year, is that one day on Mercury lasts 176 Earth days, or 2 Mercury years. Considering also that the lack of a planetary atmosphere means there is no redistribution of temperature around the planet, a large gradient exists across the terminator, with temperatures reaching ~ 700 K on the dayside surface yet dropping to ~ 95 K at night [NASA, 2018].

2.3.1 Orbital Characteristics

Mercury's spin axis is offset only 2° from its orbital plane, and it therefore does not experience seasons in the Earth sense due to tilting. However, the highly eccentric elliptical orbit around the Sun produces seasonal variations in the solar wind conditions between Mercury's perihelion at a heliocentric distance of 0.31 AU and aphelion at 0.47 AU. Although the average solar wind velocity remains close to 450 km s^{-1} throughout Mercury's orbit [Burlaga, 2001], the plasma density and IMF strength vary considerably during a year. Using a scaling of $1/R^2$ from measurements at 1 AU, Slavin & Holzer [1981] calculated the expected plasma number density to decrease from 73 cm^{-3} at perihelion to 32 cm^{-3} at aphelion, values that were corroborated by Helios 1 observations [Burlaga, 2001]. As a result, the ram pressure of the solar wind decreases by more than a factor of two during a Mercury year, from $\sim 26.5 - 11.0$ nPa [Fujimoto *et al.*, 2007].

The IMF strength at Mercury is ~ 5 times greater than that at Earth, but the decrease with heliocentric distance results in a factor of 2 difference between Mercury perihelion ($\sim$ 30 nT) and aphelion ($\sim$ 15 nT) [James *et al.*, 2017]. In addition to the variation in average field magnitude, the expected Parker spiral angle increases from 17° at perihelion to 25° at aphelion [Slavin & Holzer, 1981; James *et al.*, 2017], although the actual orientation of the IMF at Mercury depends on the location of the planet relative to the heliospheric current sheet, with short-term variability also contributing. James *et al.* [2017] showed further that the orientation of the IMF is less stable at perihelion, evidenced by a higher probability of the clock angle rotating no more than 20° within a 5 minute interval at aphelion.

2.3.2 The Hermean Magnetosphere

As the only other terrestrial planet with an internally generated dipolar field, Mercury shares many similarities to Earth, however significant differences also exist between the two systems. These can be attributed in part to the contrasting solar wind conditions at the two planets, but internal factors are also extremely important.

2.3.2.1 Mercury's Internal Dipolar Field

Magnetometer data from the first Mercury flyby of Mariner 10 confirmed the existence of an intrinsic planetary dipolar magnetic field at Mercury. Ness *et al.* [1974] initially interpreted these data as evidence of a southward-directed dipole, like the Earth's, but offset substantially from the centre of the planet and with a dipole moment $\sim$ 2500 times weaker than Earth. Later observations from the second Mariner 10 flyby [Ness *et al.*, 1975] led to a suggestion of a planet-centred dipole with a small tilt relative to the rotation axis of the planet.

MESSENGER data have since shown that the dipole is aligned with the rotation axis to within 1° and offset northwards along this axis by a distance of 484 ± 11 km ($\sim 0.2\ R_M$) [Alexeev *et al.*, 2010; Anderson *et al.*, 2011; Johnson *et al.*, 2012]. The weak dipole moment of 190 nT ${R_M}^3$ produces a surface magnetic field only 1% of the Earth's [Ness *et al.*, 1974]. However, the northward offset means the dipolar surface field strength varies considerably between hemispheres, from $\sim$ 250 nT in the south to $\sim$ 700 nT at the north pole [Johnson *et al.*, 2012].

2.3.2.2 Shape and Location of the Magnetopause

The high solar wind ram pressure at Mercury's orbit acting on the weak planetary dipolar magnetic field results in the formation of a very small and rigid magnetosphere. The highly compressed nature of the dayside magnetosphere was shown by Ness *et al.* [1974], who initially calculated a magnetopause standoff distance at the subsolar point of only 1.6 R_M from Mariner 10 data. Later work by Slavin *et al.* [2009b] included the first MESSENGER flyby and concluded that the magnetopause was compressed even closer to the surface of the planet, at an altitude of just 0.4 R_M.

Winslow *et al.* [2013] used a significantly larger dataset of magnetopause crossings from the first 3 Mercury years of the MESSENGER mission. Multiple magnetopause crossings can be observed on a single spacecraft pass, due either to motion of the magnetopause back and forth over the spacecraft location, or a trajectory that grazes along the magnetopause and therefore repeatedly dips in and out of the magnetosphere. Winslow *et al.* [2013] therefore identified the innermost and outermost magnetopause crossing on each inbound and outbound pass of MESSENGER, and took the midpoint between the two to be the magnetopause location for the purpose of fitting a model magnetopause shape. The best fit was found to a model proposed by Shue *et al.* [1997], given in aberrated MSM′ coordinates by

$$R = \sqrt{X^2 + \rho^2} = R_{SS} \left(\frac{2}{1 + cos\theta} \right)^{\alpha}, \tag{2.2}$$

where R is the distance from the centre of the dipole, R_{SS} is the subsolar standoff distance of the magnetopause, $\theta = \tan^{-1}(\rho/X)$, and α describes the flaring of the magnetopause in the magnetotail, such that $\alpha < 0.5$ defines a closed magnetotail and an open magnetotail is denoted by $\alpha \geq 0.5$. The final parameter in Equation 2.2 defines the distance from the axis of revolution for a cylindrically symmetric magnetopause:

$$\rho = \sqrt{Y^2 + Z^2}, \tag{2.3}$$

The best fit to Equation 2.2 yielded a subsolar standoff distance of 1.45 R_M, and a flaring parameter $\alpha = 0.5$.

However, as these data were obtained from 3 Mercury years, the eccentric orbit means there is a wide range of magnetosphere sizes due to the variable solar wind

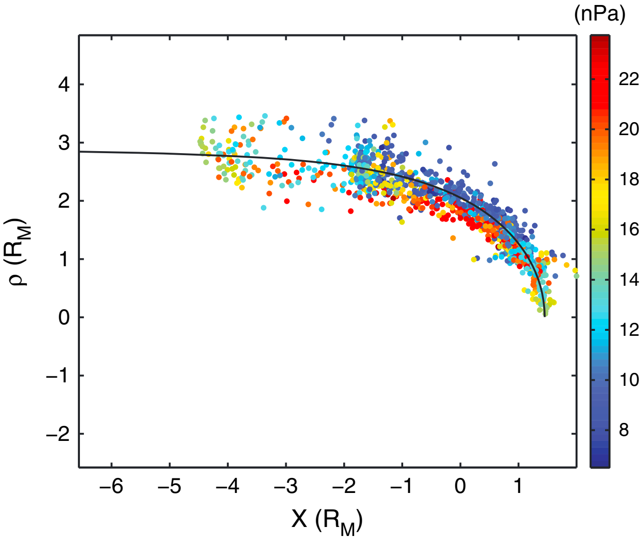

Figure 2.12: The midpoint of inner and outer magnetopause crossings from each pass, colour-coded based on the solar wind ram pressure. The Shue *et al.* [1997] model fit to the entire dataset is indicated by the solid black line. Higher ram pressures result in a magnetopause that is closer to the planet, as expected. Figure from Winslow *et al.* [2013].

ram pressure. Fixing the flaring parameter at 0.5, R_{SS} decreases from $1.55-1.35$ R_M as P_{ram} increases from $\sim 9-22$ nPa. This variability is shown in Figure 2.12, where the best fit Shue model for the entire dataset is indicated by the solid black line. The midpoints of the inner and outer magnetopause crossings on a pass are indicated by the coloured dots. The flaring parameter of 0.5 indicates that the magnetotail is at the transition between open and closed, evidenced by the almost cylindrical magnetopause at a downtail distance of only $\sim 2-3$ R_M, compared to a distance of ~ 100 R_E before the Earth's magnetopause stops flaring [Slavin *et al.*, 1983].

One of the consequences of such a compressed dayside magnetosphere, combined with the offset dipole, is the potential for direct solar wind impact on the surface of Mercury in the southern hemisphere during extreme solar wind events. Slavin & Holzer [1979] suggested that intense erosion could, in rare cases, lower the magnetopause altitude to such an extent that it intersects the planetary surface. Zhong *et al.* [2015] used 3 Earth years of MESSENGER observations to model the magnetopause including indentations at the northern and southern cusps, and concluded that these depressions could expose not only the southern hemisphere, but also the northern hemisphere surface at mid-latitudes, to the solar wind directly during periods of high solar wind pressure.

Analysing specific cases of extreme solar wind dynamic pressure events, Slavin *et al.* [2014] identified an interplanetary coronal mass ejection (ICME) encountering Mercury. The magnetopause crossing during this event was consistent with a magnetopause standoff distance of just 1.03 R_M, following the Winslow *et al.* [2013] magnetopause model, with the result that the magnetopause at high latitudes in the southern hemisphere would intersect the surface. Further, Johnson *et al.* [2016] proposed that such direct exposure of some of the planetary surface to the solar wind could occur $1.5 - 4\%$ of the time at Mercury.

2.3.2.3 Induced Magnetic Fields

Due to Mercury's large, electrically conducting core, changes in the external magnetic field are expected to take $10^4 - 10^5$ years to diffuse into the centre of the planet [Glassmeier, 2013]. The core can therefore be taken to act as a perfectly conducting sphere that will react to the short timescale changes in solar wind pressure. Hood & Schubert [1979] suggested that the currents induced by a step increase in the ram pressure would generate magnetic fields that opposed the pressure change sufficiently that the magnetopause would remain at an altitude of at least ~ 0.2 R_M, however reconnection was not considered in this calculation.

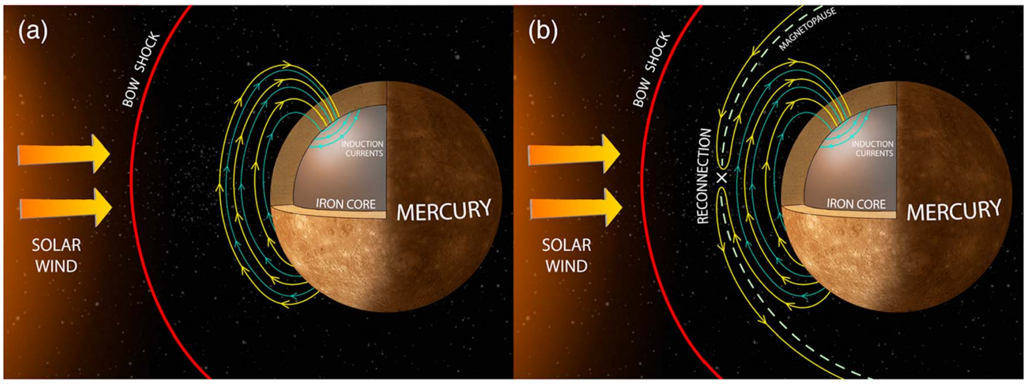

Figure 2.13: (a) Schematic showing the generation of induction currents (green loops) at the top of Mercury's core, that act to oppose the compression of intrinsic magnetospheric field lines (yellow) towards the planet through the generation of addition field lines (green). (b) Magnetic reconnection at the dayside magnetopause continues to erode the magnetospheric field, thereby counteracting some of the induction effect by opening magnetic flux and transporting it into the magnetotail. Figure from Slavin *et al.* [2014].

Johnson *et al.* [2016] observed increases in the dipole moment of $\sim 5\%$ as a result of induced fields, which serve to oppose the compression of the dayside magnetosphere by increased ram pressure. However, the effectiveness of these induced fields is reduced by reconnection at the dayside magnetopause. In their study of extreme solar wind events at Mercury, Slavin *et al.* [2014] observed the magnetopause at lower altitudes than would be expected when considering the enhancement of the dayside magnetic field by induced fields alone, and attributed this negation of the induction effect to enhanced reconnection rates during the intervals examined. This effect is shown in Figure 2.13, where the induction currents and associated magnetic fields are shown to enhance the magnetic dipole moment and increase the amount of closed magnetic flux in the dayside magnetosphere (panel a). Panel b then shows the erosion of the dayside magnetopause towards the planetary surface by reconnection, opening some of the increased magnetic flux and transporting it into the magnetotail.

Despite the negating effect of reconnection on the bolstering of magnetic field by induction, erosion of the dayside magnetopause at Mercury is much less effective than at Earth. Heyner *et al.* [2016] calculated a planetward erosion of the magnetopause of only 4% during extreme solar wind events, compared to a maximum value of 22% at Earth, reinforcing the understanding that the small magnetosphere of Mercury is much more rigid. They also suggest that dayside compression is not always the dominant factor in the size of the induced magnetic fields. As reconnection loads increased open flux into the magnetotail, the tail current is enhanced, subsequently creating a perturbation that decreases the magnetic field strength close to the planet in the magnetotail. To oppose this change, further currents are induced in the core, with the resultant magnetic field enhancement representing $15 - 27\%$ of the total increase in the magnetospheric field near the subsolar magnetopause during average solar wind conditions.

2.3.2.4 Quantifying Reconnection at Mercury

Many of the methods used to describe the rate of reconnection at Earth make use of upstream measurements of solar wind properties in defining coupling functions that describe how the reconnection voltage varies, as discussed in Section 2.1.2. At Mercury, there is no such upstream monitor, therefore complex functions including these properties cannot be used in the same way. However, the cross-polar cap potential, which provides a measure of the amount of open magnetic flux that is transferred into the magnetotail via reconnection, can still be estimated by a variety of methods.

Using measurements of the magnetic field component normal to the magnetopause on MESSENGER's second flyby of Mercury, Slavin *et al.* [2009a] calculated a cross-polar cap potential of ~ 30 kV, a value in good agreement with the 29 kV mean value obtained by DiBraccio *et al.* [2013] using the same method for multiple magnetopause crossings. Imber *et al.* [2014] calculated the magnetic flux content of large flux transfer events at Mercury to determine a maximum contribution from a FTE of 25 kV to the total cross-polar cap potential, suggesting that the mean contribution could be ~ 12 kV from each event. A different approach was taken by DiBraccio *et al.* [2015a], who used the dispersion of proton velocities in the plasma mantle to calculate a potential of 23 kV and 29 kV on two case studies. However, a later study by Jasinski *et al.* [2017] applied the same method on a larger sample of 94 mantle traversals to calculate a mean potential of just ~ 19 kV.

Reconnection has also been quantified at Mercury using the dimensionless ratio B_N/B_{MSp}. From data obtained during the second MESSENGER flyby, Slavin *et al.* [2009a] estimated a reconnection rate of 0.13, about an order of magnitude higher than similar measurements at Earth. On a larger survey of 43 dayside magnetopause crossings with well-defined values of B_N, DiBraccio *et al.* [2013] calculated a mean ratio of 0.15 ± 0.02. Interestingly, they found no clear variation in the reconnection rate with magnetic shear angle, as shown in Figure 2.14. This suggests that, unlike previous observations at Earth, reconnection can occur across a wide range of magnetic shear angles at the dayside magnetopause of Mercury.

The lack of a clear dependence on shear angle in reconnection rates was attributed by DiBraccio *et al.* [2013] to the low β plasma in the magnetosheath of Mercury, as predicted by Slavin & Holzer [1979]. As magnetosheath field is compressed and draped around the magnetopause, the plasma within the flux tubes is accelerated away from the subsolar point and out along the draped field lines, creating a *plasma depletion layer* of low plasma density [Zwan & Wolf, 1976]. The thickness of this depletion layer scales as ${M_A}^{-2}$, where M_A is the Alfvén Mach number, so that for the low M_A solar wind in the inner heliosphere near Mercury's orbit, the plasma depletion layer should occupy a larger fraction of the magnetosheath than at Earth. Gershman *et al.* [2013] showed that strong plasma depletion layers form regularly at Mercury, reducing the plasma pressure. The resultant low β magnetosheath can lead to symmetric magnetic fields either side of the magnetopause, with fields differing in some cases by less than 10% [DiBraccio *et al.*, 2013]. Consequently, reconnection is possible at low magnetic shear angles when there is a guide field, a component parallel to the X-line of equal magnitude on both sides of the magnetopause, as discussed by Sonnerup [1974].

2.3.2.5 Magnetospheric Dynamics at Mercury

The small size of Mercury's magnetosphere combined with the strong interaction with the solar wind in the form of high reconnection rates results in a very dynamic magnetosphere with rapid circulation of magnetic flux. Slavin *et al.* [2009a] esti-

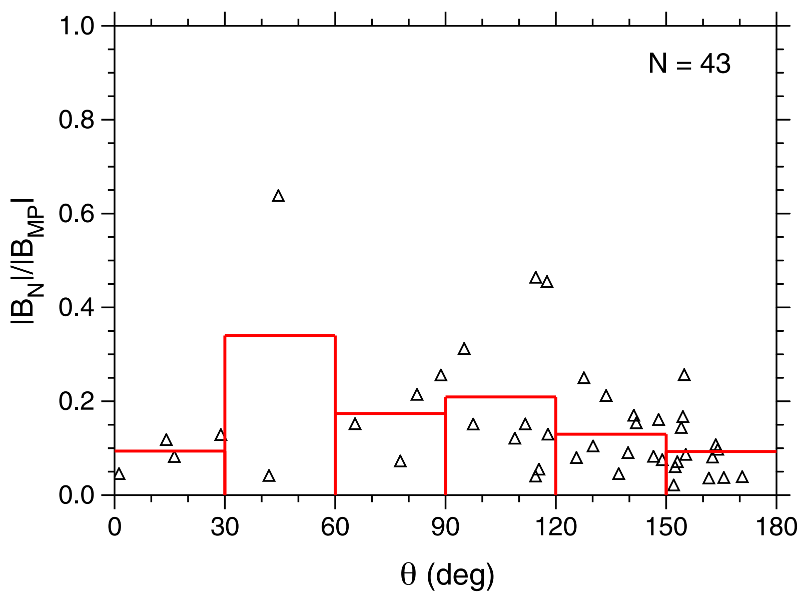

Figure 2.14: Dimensionless reconnection rates calculated for 43 magnetopause crossings under a range of magnetic shear angles. Individual crossings are denoted by the triangles, whilst the mean in each 30° shear angle bin is shown by the red lines. Figure from DiBraccio *et al.* [2013].

mated a Dungey cycle at Mercury of only a few minutes, based on calculations of a ~ 2 minute drift time for plasma to move tailward across the polar cap using measurements of B_N during dayside reconnection. This short timescale was supported by later observations of 2-3 minute duration increases in the magnetic flux content of the magnetotail [Slavin *et al.*, 2010a]. This is analogous to the substorm growth phase at Earth, in which dayside reconnection opens magnetic flux and transfers it in to the magnetotail on timescales of ~ 1 hour. Imber & Slavin [2017] analysed similar tail loading events throughout the MESSENGER mission and calculated that during substorms at Mercury the magnetotail lobe field strength increases by almost 25%, meaning that each lobe contains $\sim 33\%$ of the total magnetic flux in the magnetosphere. Compared to the maximum contribution of $\sim 12\%$ at Earth [Milan *et al.*, 2004], this further enhances the picture of Mercury's magnetosphere as a small, strongly solar wind-driven magnetosphere with rapid flux circulation.

The addition of open flux into the magnetotail lobes increases the magnetic gradient across the tail current sheet, between the sunward-directed northern lobe and anti-sunward southern lobe fields. Rapid closure of the large quantity of magnetic flux in the magnetotail produces high-velocity, low plasma density, bursty bulk flows that travel sunward and are often accompanied by a region of magnetic field that more closely resembles a dipolar configuration than the usual stretched tail, therefore termed a dipolarization [e.g. Angelopoulos *et al.*, 1992]. Such dipolarization fronts have been observed extensively at Mercury [Sundberg *et al.*, 2012], but are found more commonly in the post-midnight sector [Sun *et al.*, 2016; Dewey *et al.*, 2017].

This dawn-dusk asymmetry is also seen in the observations of magnetic flux ropes in the magnetotail of Mercury [Sun *et al.*, 2016; Smith *et al.*, 2017]. Similar to the formation of flux transfer events at the dayside magnetopause, magnetic structures can be created between two parallel X-lines in the magnetotail. For perfectly antiparallel lobe fields, a plasmoid will form as a magnetic loop, with no axial field. However, there is often a shear across the tail current sheet, resulting in a component of the magnetic field in the Y direction [Cowley, 1981]. Structures formed in this scenario will therefore exist as flux ropes, with a strong axial core field. The flux rope will be ejected from the dominant X-line either planetward or anti-sunward, creating a bulge as the surrounding lobe field drapes around it to form a *travelling compression region* [Slavin *et al.*, 2009a]. DiBraccio *et al.* [2015b] observed flux ropes moving in both directions along the Sun-planet line in the magnetotail of Mercury, with a typical radius of $\sim 0.18\ R_M$ and core fields of ~ 40 nT, implying that the planetward-moving plasmoids may provide a substantial contribution to the total return flow of magnetic flux that completes the Dungey cycle.

The magnetotail is separated from the dayside magnetosphere by the cusp regions, through which magnetosheath plasma can propagate towards the planetary surface. Zurbuchen *et al.* [2011] observed enhanced fluxes of heavy ions such as Na^+, Mg^+, Si^+ and O^+ near the northern polar region, indicating that solar wind access to the planetary surface is responsible for the sputtering of neutral atoms that are subsequently ionised. However, variability in the fluxes observed on different spacecraft passes suggests that the size and location of the cusp is highly dependent on the orientation of the IMF. Winslow *et al.* [2012] observed the northern cusp between local times of 7.2-15.9 h, and ranging from latitudes of 56-84° in Mercury Solar Orbital (MSO) coordinates, which are similar to the MSM coordinates defined previously but with the origin at the centre of Mercury rather than centred on the dipole. During periods of anti-sunward IMF, reconnection just tailward of the cusp increases the latitudinal extent, and results in higher plasma pressures than are seen during sunward IMF. The northward offset of the planetary dipole led Winslow *et al.* [2012] to suggest that the southern cusp could see fluxes a factor of 4 higher, over a region of twice the latitudinal extent, than the northern cusp, representing a much greater source of planetary ions than in the northern hemisphere.

Raines *et al.* [2014] showed that the low-energy $(100 - 300$ eV$)$ Na^+ group ions (Na^+, Mg^+, Si^+) travel upwards from the surface in the cusp, whereas high-energy ions of ≥ 1 keV are seen to have been ionised near the dayside magnetopause and then swept into the cusp region on reconnected field lines. As these open field lines travel anti-sunward, the presence of gyrating particles increases the plasma pressure and creates a general decrease in the magnetic field intensity in the cusp. However, additional extreme reductions in field strength have been observed to last for a few seconds at a time across a wider latitudinal range than the main cusp [Slavin *et al.*, 2014]. Termed *cusp plasma filaments*, these decreases are diamagnetic in origin, caused by gyrating magnetosheath plasma injected into discrete flux tubes following reconnection. Poh *et al.* [2016] observed some filaments with a twisted, flux rope-like structure, suggesting that the filaments are low-altitude extensions of flux transfer events formed by localised reconnection at the dayside magnetopause.

2.4 Flux Transfer Events at Mercury

Flux transfer events were first seen at Mercury in magnetometer data from the Mariner 10 flybys [Russell & Walker, 1985], as shown in Figure 2.15. The ~ 1 s duration of the events led the authors to estimate the diameter of Mercury FTEs to be ~ 400 km, a spatial scale $\sim 8\%$ of the width of the magnetosphere in the terminator plane. This is a similar relative scale to FTEs in Earth's magnetosphere, but the low peak magnetic field amplitude observed by Russell & Walker [1985] of ~ 40 nT suggested a total flux content of just 5 kWb, implying that FTEs make only a very small contribution to the total flux circulation within the magnetosphere.

Later data from the MESSENGER flybys of Mercury provided contrasting observations, however. Slavin *et al.* [2010b] identified 6 FTEs during the first two flybys, with a large range of sizes. Whilst the smallest event was of similar scale to those identified by Russell & Walker [1985], with a diameter of ~ 400 km and a flux content of ~ 1 kWb, a number of larger events were also observed. Two FTEs were identified with durations greater than 6 s, implying a diameter of $\sim 1\ R_M$, 6 times larger than seen previously at Mercury. Furthermore, the maximum core field of > 100 nT seen in one of the events suggests a total magnetic flux content of 0.2 MWb, a contribution of $\sim 5\%$ towards the total flux contained within one lobe of the magnetotail.

Flux transfer events at Mercury have also been found to be far more prevalent than at Earth. Slavin *et al.* [2012] observed a *flux transfer event shower* of 163 FTEs on a single MESSENGER pass through the southern magnetotail lobe and surrounding magnetosheath, as shown in Figure 2.16. Of these, 66 were identified

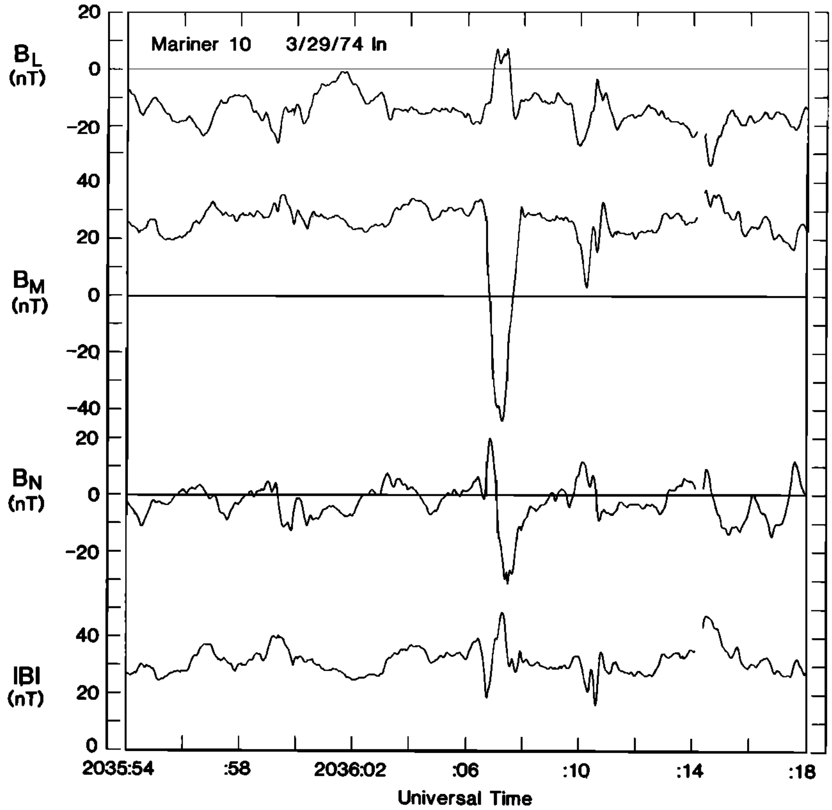

Figure 2.15: Mariner 10 magnetometer data from the first Mercury flyby, showing a flux transfer event at 20:36:07, as indicated by the bipolar signature in B_N and the large increase in B_M. Figure from Russell & Walker [1985].

on the basis of a flux rope signature in the magnetometer data, whilst the remainder produced a travelling compression region (TCR) signature. All of the events were seen in a 25 minute interval, with a mean separation between each event of $\sim$ 8-10 s, significantly lower than the $\sim$ 8 min separation seen at Earth [Rijnbeek *et al.*, 1984]. However, the mean duration of Mercury FTEs was confirmed by these observations to be $\sim$ 2-3 s, compared to $\sim$ 1 min at Earth [e.g. Fear *et al.*, 2007].

The dayside magnetosphere of Mercury is also rife with FTEs, as shown by Imber *et al.* [2014] in a study of 90 passes through the dayside magnetopause within 1 R_M of $Y' = 0$. In this time, 58 FTEs were identified with core fields larger than the amplitude of the dipolar field just inside the magnetopause, highlighting the extremely high flux content of Mercury FTEs. An example event from this study is shown in Figure 2.17, in aberrated MSM coordinates. Additionally, hodograms of the maximum-minimum and maximum-intermediate variance components show

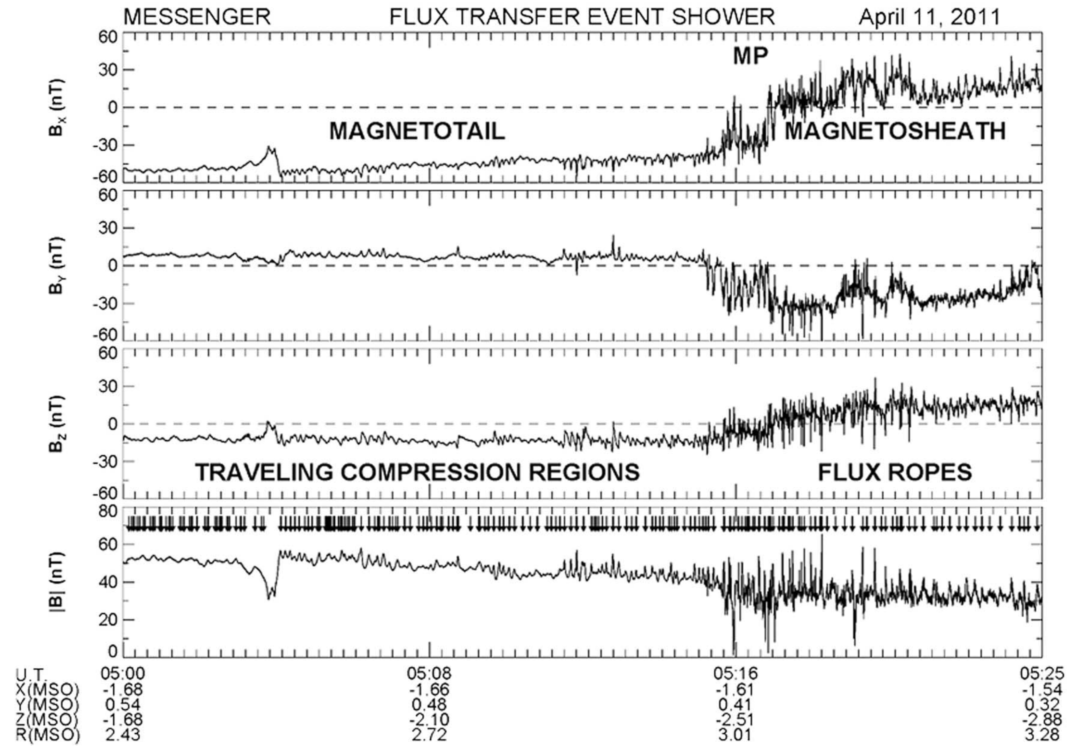

Figure 2.16: Magnetometer data from a MESSENGER traversal of the magnetopause in the southern magnetotail. Vertical arrows in the bottom panel indicate the locations of travelling compression regions inside the magnetotail, and flux transfer events in the magnetosheath. Figure from Slavin *et al.* [2012].

a clear rotation, evidence of a flux rope structure. The core field of this particular event is 280 nT, significantly greater than the background field amplitude. Although the identified FTEs were the largest events during the interval examined, assuming a mean flux content for Mercury FTEs of half that calculated for these events gives a total of $\sim$ 0.03 MWb of magnetic flux contained within each FTE. Given the repetition time suggested by Slavin *et al.* [2012], this led Imber *et al.* [2014] to estimate that FTEs may be responsible for transporting 30% of the flux required for the substorm loading phase.

The magnetosphere of Mercury has been shown to be extremely dynamic, due to its small spatial scale and strong solar wind driving. Flux transfer events at Mercury are proportionally larger and transfer more of the total flux available than their counterparts at Earth, and are therefore important factors in the magnetospheric dynamics, providing the motivation for the large-scale investigations presented in this thesis.

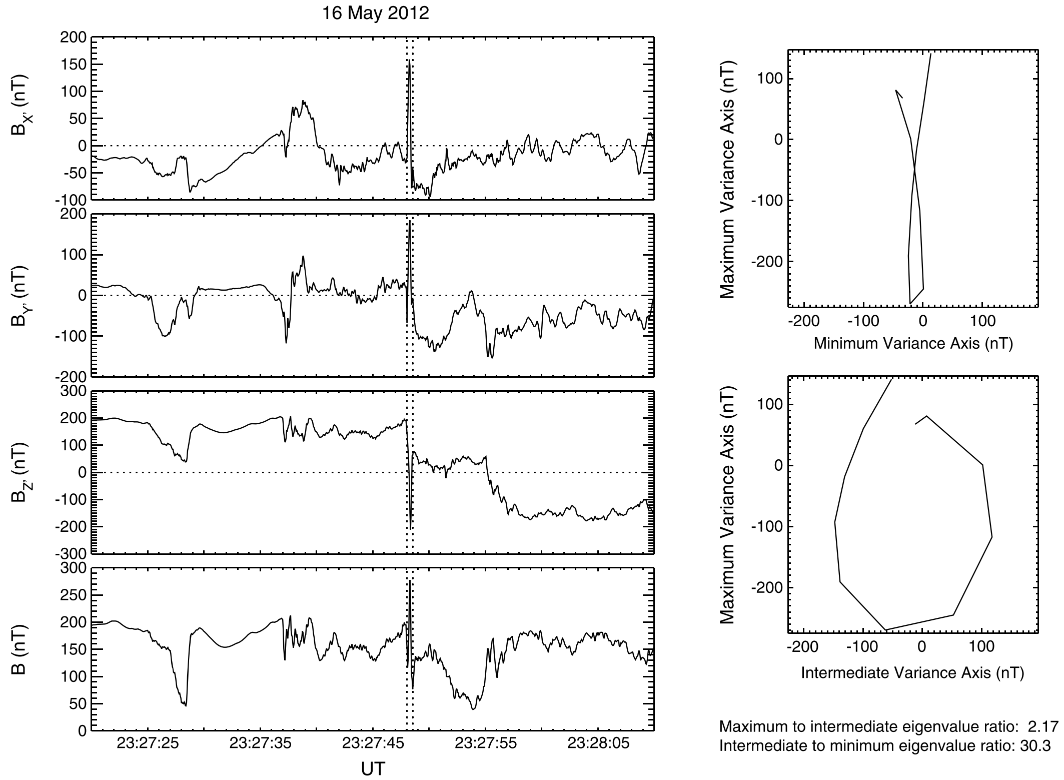

Figure 2.17: An example of magnetometer data showing a clear flux transfer event signature in aberrated MSM' coordinates. Also shown are hodograms of the maximum-minimum and maximum-intermediate variance components. Figure from Imber *et al.* [2014].

Chapter 3

Instrumentation

The work presented in Chapters 4-6 has been performed using data obtained by instruments onboard the MErcury Surface, Space ENvironment, GEochemistry and Ranging (MESSENGER) spacecraft. This chapter provides an overview of the mission, including details of its orbit around Mercury and the instrumentation that has been fundamental to completing this thesis.

3.1 The MESSENGER Mission

NASA's MESSENGER mission was launched on 3 August 2004, beginning a seven year journey to Mercury. Its trajectory included one Earth flyby, two flybys past Venus, and three encounters with Mercury before orbital insertion on 18 March 2011. The nominal mission was scheduled to last 1 Earth year, until 18 March 2012, although two subsequent mission extensions enabled in situ observations to continue until MESSENGER impacted Mercury's surface on 30 April 2015.

The mission was designed to answer six main scientific goals, aimed at exploring the formation, evolution and history of Mercury and its space environment [Solomon *et al.*, 2001, 2007]. These ranged from questions regarding the planetary formation processes that led to the highest fractional metal content of any Solar System planet and understanding the nature and origin of Mercury's large core, through to investigating the geological history of the contracting planetary surface and explaining the presence of radar-bright features located in the polar regions. Moving further outwards, MESSENGER was also commissioned to investigate the sources and sinks of volatile elements in the exosphere, and describe the nature and origin of the intrinsic magnetic field. A suite of seven instruments was therefore present onboard MESSENGER, a schematic of which is shown in Figure 3.1. A brief outline of each instrument is given in Table 3.1.

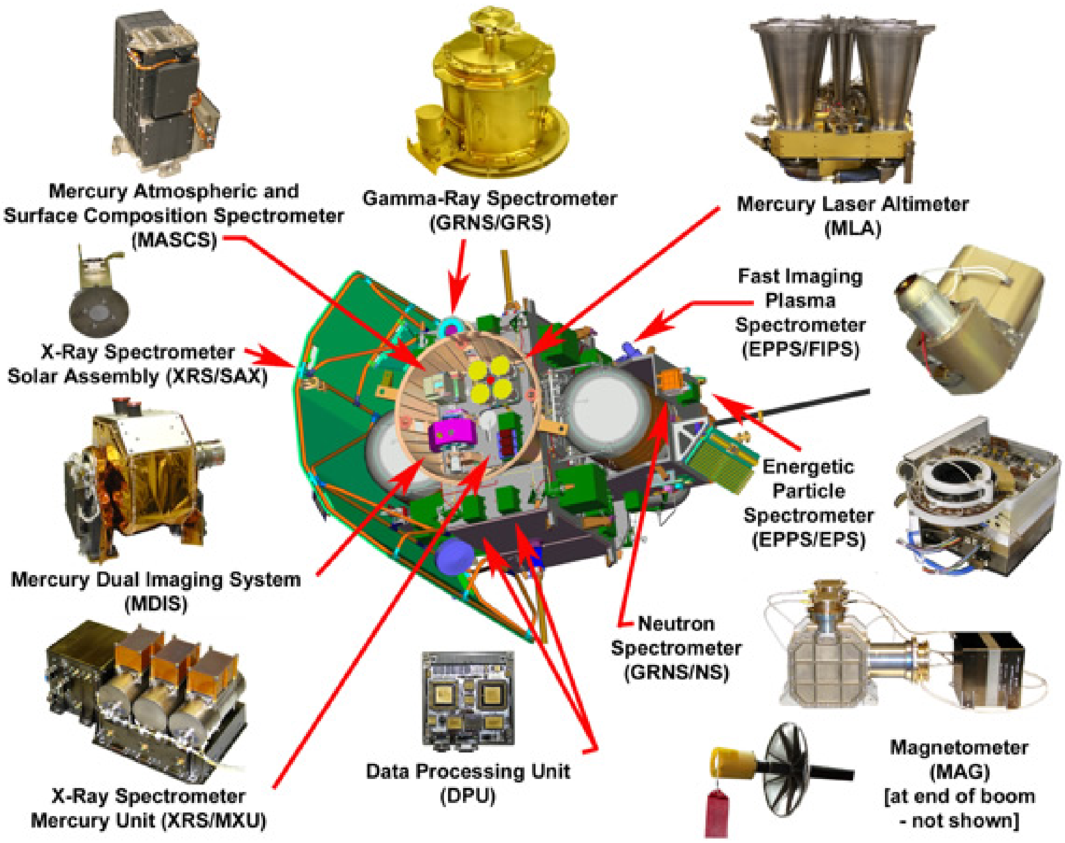

Figure 3.1: A schematic showing the location of the scientific instruments on MESSENGER. The magnetometer (MAG) is situated at the end of a 3.6 m boom that extends anti-sunward. Figure from JHU/APL.

The MESSENGER spacecraft itself was three-axis stabilised, and remained in a fixed orientation with respect to the Sun, with all of the instruments protected from solar heating by a sunshade [Santo *et al.*, 2001]. Power was provided by two solar panels, which were able to rotate about an axis in the ecliptic plane. Different viewing angles could be achieved for the instruments through rotation about the Sun-spacecraft line, as shown in Figure 3.2.

Instrument		Brief Description
EPPS (Energetic Particle and Plasma Spectrometer)	EPS (Energetic Particle Spectrometer)	Energetic ions (up to ~ 3 MeV) and electrons ($\sim 20 - 400$ keV)
	FIPS (Fast Imaging Plasma Spectrometer)	Scans $0 - 15$ keV/q range (thermal ions) in 1 min (10s steps)
GRNS (Gamma-Ray and Neutron Spectrometer)		Observes surface chemistry and polar deposit composition
MAG (Magnetometer)		3-axis fluxgate, on 3.6 m boom
MASCS (Mercury Atmospheric and Surface Composition Spectrometer)	UVVS (Ultraviolet-Visible Spectrometer)	Exospheric emissions on the limb with 1 nm spectral resolution
	VIRS (Visible-Infrared Spectrograph)	Surface reflectance at 0.3-1.45 μm with 4 nm spectral resolution
MDIS (Mercury Dual Imaging System)	Wide-angle Camera (WAC)	10.5° FOV, colour imager
	Narrow-angle Camera (NAC)	1.5° FOV, black and white
MLA (Mercury Laser Altimeter)		8 Hz pulsing, maps northern topography to 30 cm precision
XRS (X-Ray Spectrometer)		0.7-10 keV, X-ray surface fluorescence

Table 3.1: A list of the scientific payload onboard MESSENGER [Gold *et al.*, 2001; Solomon *et al.*, 2007].

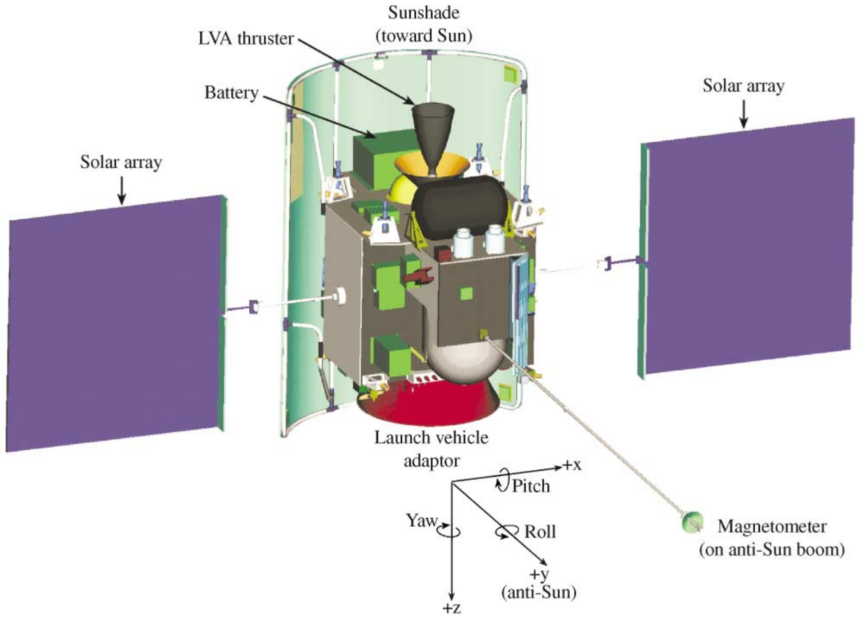

Figure 3.2: Diagram showing the orientation of MESSENGER, including the sunshade and solar panels extending away from the spacecraft in the ecliptic plane. Figure from Santo *et al.* [2001].

3.2 The Magnetometer Experiment

Data obtained by the Magnetometer (MAG) instrument were fundamental in completing the work presented in this thesis. A comprehensive overview of the specifications and operations of MAG are given in Anderson *et al.* [2007], but a summary of the physical and operational details relevant to the work in this thesis is provided here. The scientific goals of the mission required an operational range covering the expected ∼600 nT surface magnetic field at the poles, with a precision high enough to resolve features seen on a small spatial and temporal scale. As such, the range of operations for use in orbit around Mercury provided measurements covering ± 1530 nT on each of three orthogonal axes, with a resolution of 0.047 nT. Data were sampled at 20 s^{-1}, and filtered digitally to provide a range of output rates between $1 - 10$ s^{-1}. An additional burst mode allowed data collection at the full 20 s^{-1} rate for 8 contiguous minutes. This mode was active for intervals when MESSENGER was inside the dayside magnetosphere or within the vicinity of the dayside magnetopause, when the temporal variability of the magnetic field measurements was expected to be at its highest.

The measurement capabilities are achieved through the use of three fluxgate

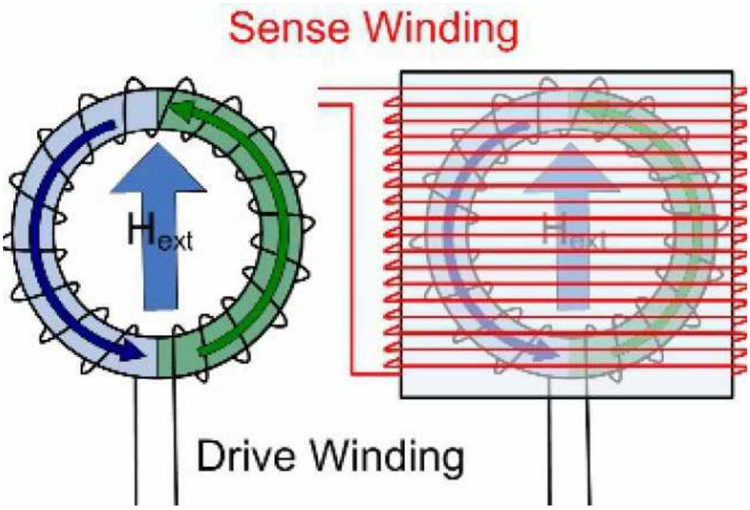

Figure 3.3: Sketch of a single-axis fluxgate. The diagram on the left shows the drive winding wrapped around the ring core, and the diagram on the right shows this setup enclosed within the sense winding, indicated in red. The blue and green arrows indicate the fields generated by the drive winding. This orientation enables measurement of an external field in the direction of H_{ext}. Figure from Imperial College, London.

sensors, mounted orthogonally to ensure full directional coverage. A fluxgate consists of a ring core of highly magnetically permeable material, wrapped in a drive winding, and in turn enclosed within the sense winding, as shown in Figure 3.3. As a square waveform current is applied to the drive winding, a magnetic field is generated in each half of the ring core with a component either parallel or anti-parallel to the direction of H_{ext}, indicated in Figure 3.3 by the green and blue colouring respectively. The material in each half core is therefore driven through its hysteresis loop, going in and out of saturation symmetrically in the absence of any external field. As a result, there is no change to the net flux through the sense winding, so no voltage is induced. In the presence of an external field, however, the half core with a parallel component (green) will come out of saturation later and the half core with an anti-parallel component (blue) will come out of saturation sooner, producing a net flux in the sense winding. This in turn drives a voltage through the sense winding, the nature of which describes the magnitude and direction of the external magnetic field.

3.3 MESSENGER Orbital Properties

Following Mercury orbital insertion, MESSENGER was placed into a highly eccentric orbit with a periapsis of ∼200 km and apoapsis of ∼15200 km. The orbital plane was inclined at 82.5° to Mercury's equator, such that the closest approach of MESSENGER to the surface occurred in the northern hemisphere at a latitude of ∼60°, and was initially closely aligned with the dawn-dusk terminator. However, the orbital plane was fixed in inertial space, and therefore precessed around the planet throughout a Mercury year. Figure 3.4 shows MESSENGER's orbital inclination along with an example of the dawn-dusk and noon-midnight orbits.

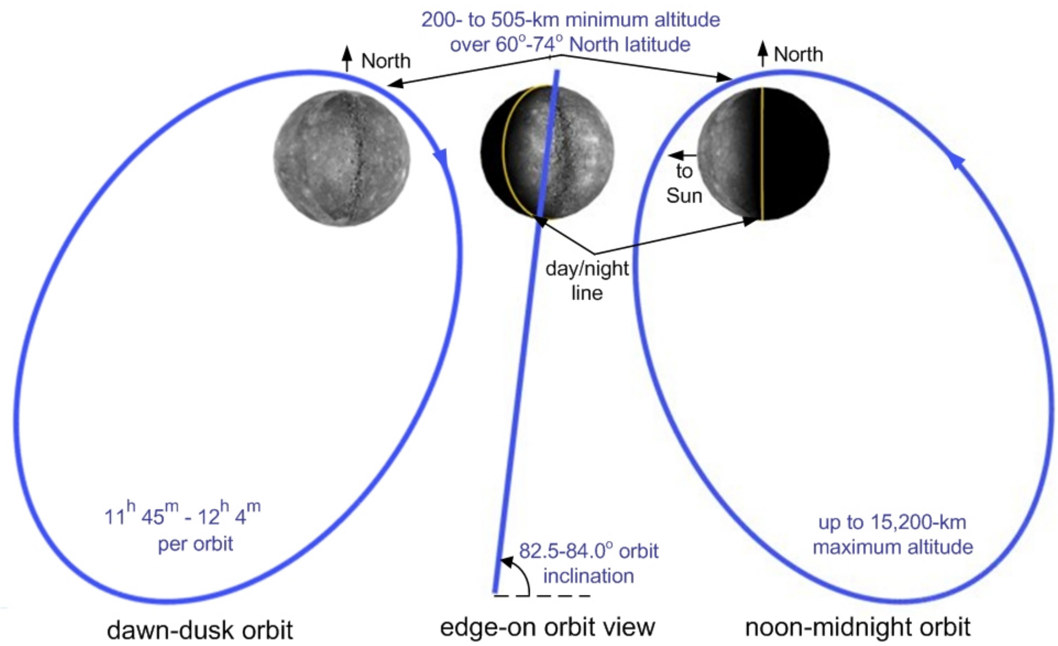

Figure 3.4: MESSENGER's orbital trajectory, shown in the dawn-dusk and noon-midnight planes. The high inclination of the orbit is also indicated. Figure from JHU/APL.

Following completion of the first Earth year of observations, the early period of the first extended mission saw MESSENGER's initial ∼12 hour orbit reduced to 8 hours. This was done through two orbit correction manoeuvres (OCM), as indicated in Figure 3.5. The initial orbit is shown in red, transitioning through the purple trajectory as an intermediate orbit before a second correction reduced the apoapsis further to ∼10300 km during the 8 hour orbit shown in green. MESSENGER remained in this orbital configuration until the end of mission, giving a total of ∼3300 orbits in the 8-hour configuration to supplement the ∼800 orbits lasting 12

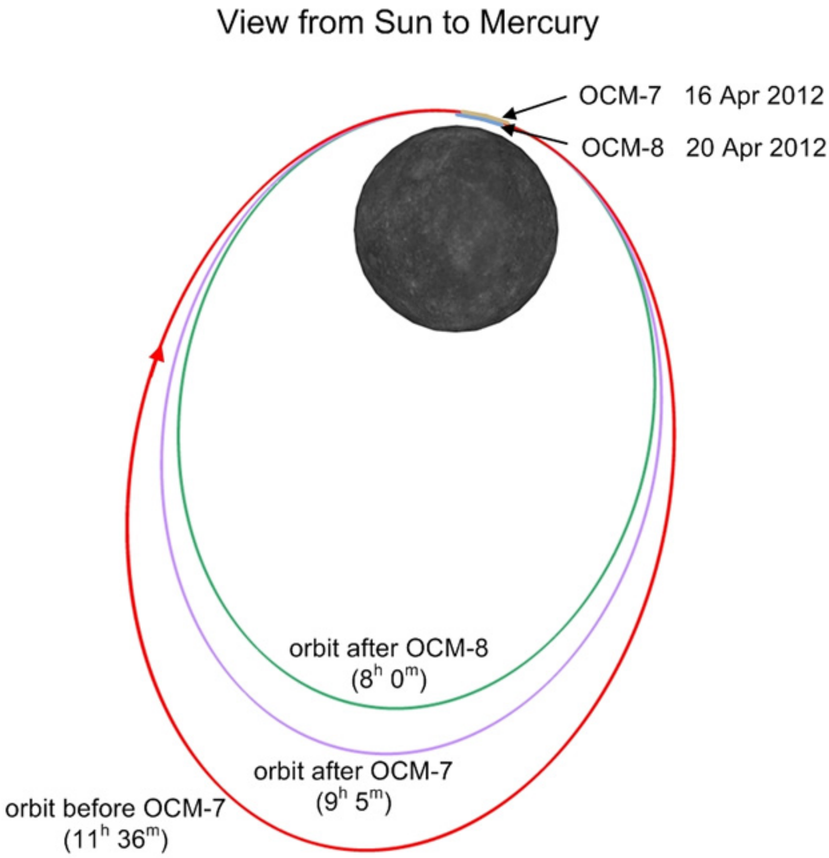

Figure 3.5: Diagram showing the transition from the initial 12 hour orbit of MESSENGER during its first year of operations at Mercury to the 8 hour orbit it occupied for the extended mission. Figure from JHU/APL.

hours each.

As a result of MESSENGER's orbital precession during a Mercury year, all magnetic local times were sampled equally. Orbits where periapsis occurred near local noon were categorised as '*hot seasons*', due to the substantial heating of spacecraft components at low altitude by the sunlit surface, despite shielding from direct sunlight. The instruments were therefore switched off during the first hot season, spanning 19 orbits between 24 May and 2 June 2011, to protect against damage early in the mission. Aside from this brief interval, data were available from the magnetometer throughout the duration of MESSENGER's operations, providing the basis of the work presented in the following chapters.

Chapter 4

IMF Clock Angle Influence on Observation of Flux Transfer Events

4.1 Introduction

As discussed in Chapter 2, much work has been done at Earth to investigate the factors influencing the rate of reconnection at the dayside magnetopause, and the subsequent formation of reconnection signatures such as flux transfer events. In both cases, it was found that the orientation of the IMF plays a crucial role, with enhancements to both the reconnection rate and the number of FTE observations during periods of southward IMF, where a large shear angle exists across the magnetopause.

At Mercury, the low Alfvén Mach number of the inner heliosphere solar wind produces greater reconnection rates than are seen at Earth [e.g Slavin & Holzer, 1979; Slavin *et al.*, 2009a; DiBraccio *et al.*, 2013], with no discernible IMF orientation effect observed in studies of a small sample size of magnetopause crossings. The investigation presented in this chapter therefore seeks to perform a large statistical study of FTEs in Mercury's dayside magnetosphere, and determine whether their formation depends on IMF orientation as is the case at Earth, or whether this proxy for reconnection shows the same clock angle-independence as seen by DiBraccio *et al.* [2013].

Section 4.2 introduces the dataset used to perform this work, and the identification of both magnetopause crossings and FTEs. The spatial distribution of these events is then discussed in Section 4.3, along with the effect of the IMF clock angle on FTE formation. Finally, these results are used to explain some differences between the distribution of FTEs observed during the early phase of MESSENGER's orbit around Mercury and a longer timespan including the first 3 Earth years.

4.2 Observations

On 18 March 2011, MESSENGER orbital insertion placed the spacecraft into an eccentric, high-inclination orbit about Mercury with an initial period of 12 h, although this was later reduced to 8 h as described in Chapter 3. The orbital plane was fixed in inertial space such that the periapsis precessed completely around the planet once every Hermean year (88 days). In this study, we have used data obtained by the Magnetometer (MAG) onboard MESSENGER, which at full resolution provided 20 samples/s [Anderson *et al.*, 2007], during the interval spanning orbital insertion until 11 February 2014. Including exactly 12 Hermean years ensured approximately even coverage of all magnetic local time (MLT) sectors over the duration of this study, with the exception of 19 orbits between 24 May and 2 June 2011, when the Magnetometer collected no data near the dayside magnetopause traversals. These orbits are symmetric about 12 h MLT and confined to a small MLT range, however, so no dawn-dusk bias is introduced by the lack of data in this period. Furthermore, the number of missing passes is small compared to the total number of passes in the affected MLT sectors, so no significant biases have been introduced. Data are presented in the aberrated MSM coordinate system (MSM′), introduced in Chapter 1.

The focus in this study is the dayside magnetosphere, therefore the magnetic field data have been examined for every encounter of MESSENGER with the magnetopause sunward of X′ = -0.5 R_M. An example of a complete 12 hour MESSENGER orbit is shown in Figure 4.1(e-f), with model locations for the bow shock and magnetopause as given by Winslow *et al.* [2013], indicated in blue and green respectively. The arrow indicates the direction of MESSENGER's trajectory during the interval shown. The components of the magnetic field measured by the MESSEN-

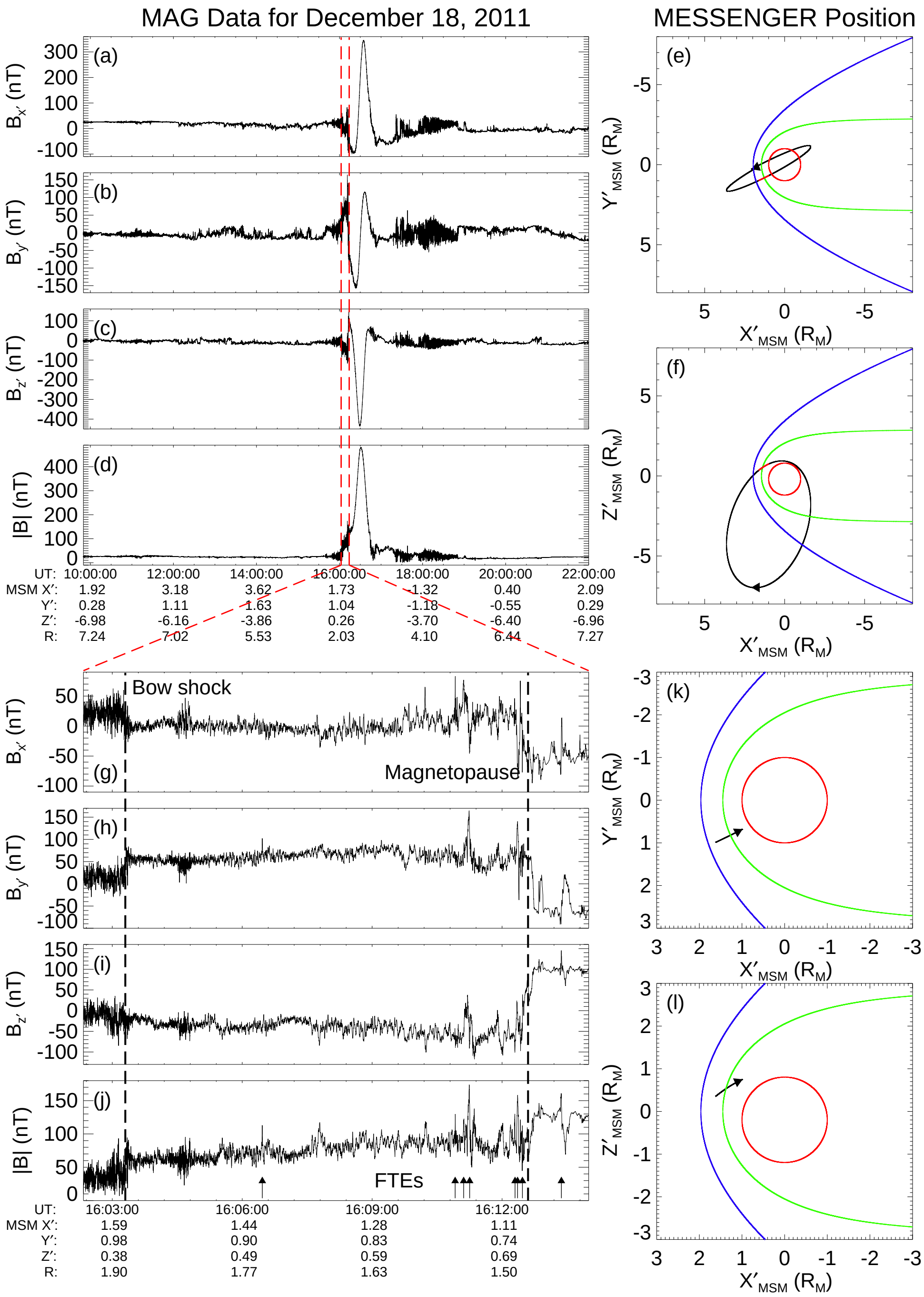

Figure 4.1: Magnetic field data in MSM′ coordinates for a complete MESSENGER orbit. Panels (a-d) show $B_{X'}$, $B_{Y'}$, $B_{Z'}$ and $|B|$ respectively. The spacecraft trajectory during the course of this orbit is projected onto the (e) Y'-X' and (f) Z'-X' planes, with the direction indicated by the arrows. Model locations of the bow shock (blue) and magnetopause (green), as given by the Winslow *et al.* [2013] models, are also shown. Panels (g-l) show a subset of the data in (a-f) above, as indicated by the dashed red lines, spanning the inbound bow shock and magnetopause crossings with some FTE signatures visible, as indicated by the arrows. From Leyser *et al.* [2017].

GER magnetometer are shown in panels (a-d), in MSM′ coordinates. Panels (g-l) show a subsection of these data, spanning the inbound crossings of the bow shock and magnetopause on this orbit. Several large amplitude FTEs are present in the data, as indicated by the arrows in Figure 4.1j.

4.2.1 Identifying magnetopause crossings and flux transfer events

Every spacecraft pass through the dayside magnetopause during the time interval considered was visually inspected for individual magnetopause crossings and FTE signatures in the magnetic field data. A pass here refers to a traversal of the magnetopause region, during which multiple individual magnetopause crossings may be observed. A single orbit close to the X′ = 0 plane will therefore contain both an inbound and outbound pass, as defined here; one for the magnetopause traversals near each of the dawn and dusk terminator.

Identification of magnetopause crossings can vary considerably between passes, due to changing conditions in the upstream magnetosheath field. On passes where the magnetic fields either side of the magnetopause are highly asymmetric, individual crossings can be identified on the basis of the large step change in $|\mathbf{B}|$, as seen in Figure 4.1j at ∼16:12:40 UT. The higher plasma density normally seen in the magnetosheath compared to inside the magnetosphere also manifests itself in MAG data as increased short-term variability in the magnetic field components. This is evident in Figure 4.1(g-j), where all components exhibit high-frequency oscillations in the magnetosheath, compared to a much smoother field after crossing the indicated magnetopause into the magnetosphere.

Magnetopause crossings are more difficult to accurately identify when the fields are symmetric across the boundary, as no step-change is present in $|\mathbf{B}|$. An example of such a pass is shown in Figure 4.2, where the format follows that of Figure 4.1a-f. Although the total field strength is seen in panel (d) to be steadily decreasing as MESSENGER travels outwards through the magnetopause, there is no large jump that can be used to identify crossings as discussed previously. However, there is still a

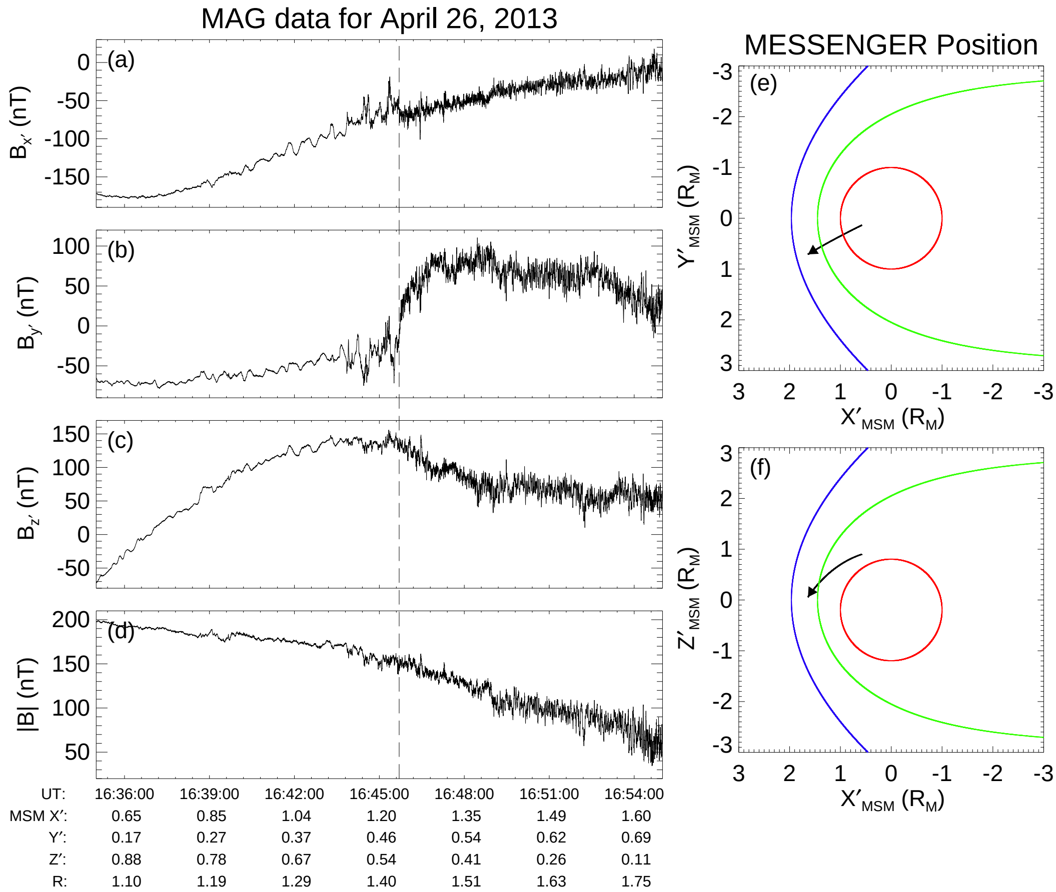

Figure 4.2: MAG data in MSM′ coordinates for a traversal of the magnetopause with symmetric field strength either side of the boundary. The format of the panels is the same as in Figure 4.1(a-f). The magnetopause crossing identified on the basis of magnetic field vector rotation is indicated by the vertical dashed line.

clear variation in the level of magnetic field fluctuations seen in all components either side of ∼16:45:00 UT, indicating a transition from magnetosphere to magnetosheath has occurred. A rotation of the magnetic field vector is also seen in panels (b-c), changing from a $B_{Z'}$-dominated magnetospheric field to a magnetosheath where the magnitude of each component is similar just outside the magnetopause.

Flux transfer events were catalogued manually on the basis of three concurrent features in the MAG data. Initially, $|\mathbf{B}|$ was inspected for short-duration large amplitude increases, as seen in the example FTE shown in Figure 4.3. This field enhancement must be accompanied by a similar signature in at least one of the MSM′ coordinates, plotted in Figure 4.3(a-c). In this instance, the component increase due to the core field of the FTE lies in $B_{Y'}$. For a field signature to be counted as an FTE, a bipolar signature must also be present in at least one component. $B_{X'}$ in

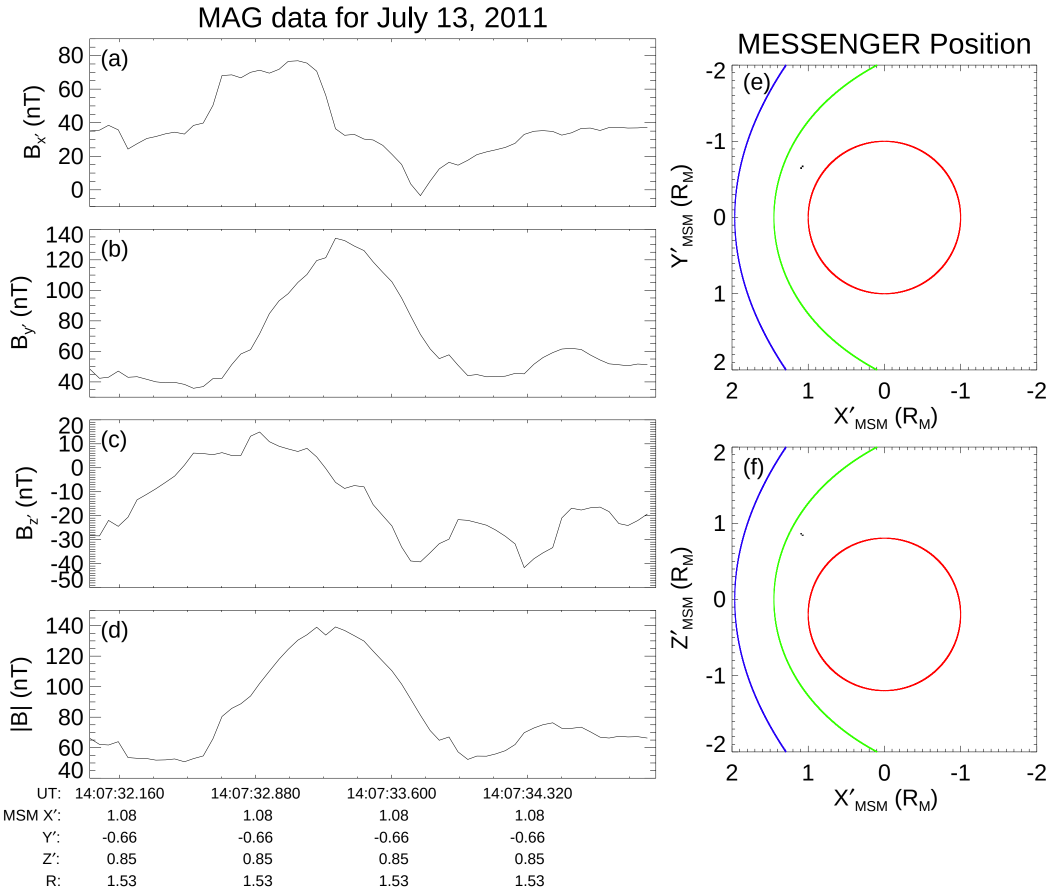

Figure 4.3: MAG data showing a flux transfer identified on July 13, 2011, where the format is the same as Figure 4.2.

Figure 4.3a exhibits just such a feature from ∼14:07:32.60 - 14:07:33.96 UT, where an initial increase is followed by a decrease, with the peak and trough falling either side of the core enhancement in $B_{Y'}$ and $|\mathbf{B}|$. A similar signature is also present in $B_{Z'}$, further confirming this feature as a flux transfer event.

Throughout the period of 12 Hermean years considered here, in 3085 passes during which the magnetopause was traversed sunward of X′ = -0.5 R_M, a total of 12133 individual magnetopause crossings and 2898 FTEs were identified using the above criteria.

4.3 Results

4.3.1 Magnetopause and FTE locations

The location of each of the 12133 magnetopause crossings identified in this work is projected into the MSM $X' - Y'$, $X' - Z'$ and $X' - \rho'$ planes in Figure 4.4(a-c). Due to the highly elliptical polar orbit of the MESSENGER spacecraft, the inbound portion of warm season orbits through the dayside magnetosphere often passes through the northern magnetic cusp. The spacecraft therefore regularly skims the magnetopause at high northern latitudes, resulting in multiple detectable magnetopause crossings on a single orbit. Additionally, ongoing reconnection or variable solar wind conditions can result in a magnetopause that repeatedly moves back and forth over the spacecraft, again leading to the observation of multiple crossings on a single pass.

Figure 4.4a shows that crossings were observed approximately equally in all MLT sectors in the dayside magnetosphere, and that on average the magnetopause crossings occurred near to the location given by the Winslow *et al.* [2013] model for the majority of orbits considered here. This average agreement with the model location is seen more clearly in Figure 4.4c, where $\rho' = \sqrt{Y'^2 + Z'^2}$ removes any latitudinal effects from the distribution seen in Figure 4.4a. Despite the model magnetopause lying close to the centre of the distribution, there is a substantial spread about the model location. This is due in part to crossings occurring during a range of Hermean seasons, resulting in significant changes to the compression of the magnetosphere by the solar wind between aphelion and perihelion [Zhong *et al.*, 2015].

The location of the FTEs identified in this study are presented in panels (d-f) as red circles, with the magnetopause crossings indicated in grey for context. Although FTEs are also seen across all MLT sectors, there is a less even spread than seen for magnetopause crossings, with the majority of events observed close to local noon. Additionally, whilst FTEs are observed in both the magnetosheath and magnetosphere, more events are seen inside the model magnetopause location, due in part to chains of FTEs that extend to low altitude near the northern cusp region.

Figure 4.5a shows a histogram of the distribution of FTE observations in MLT,

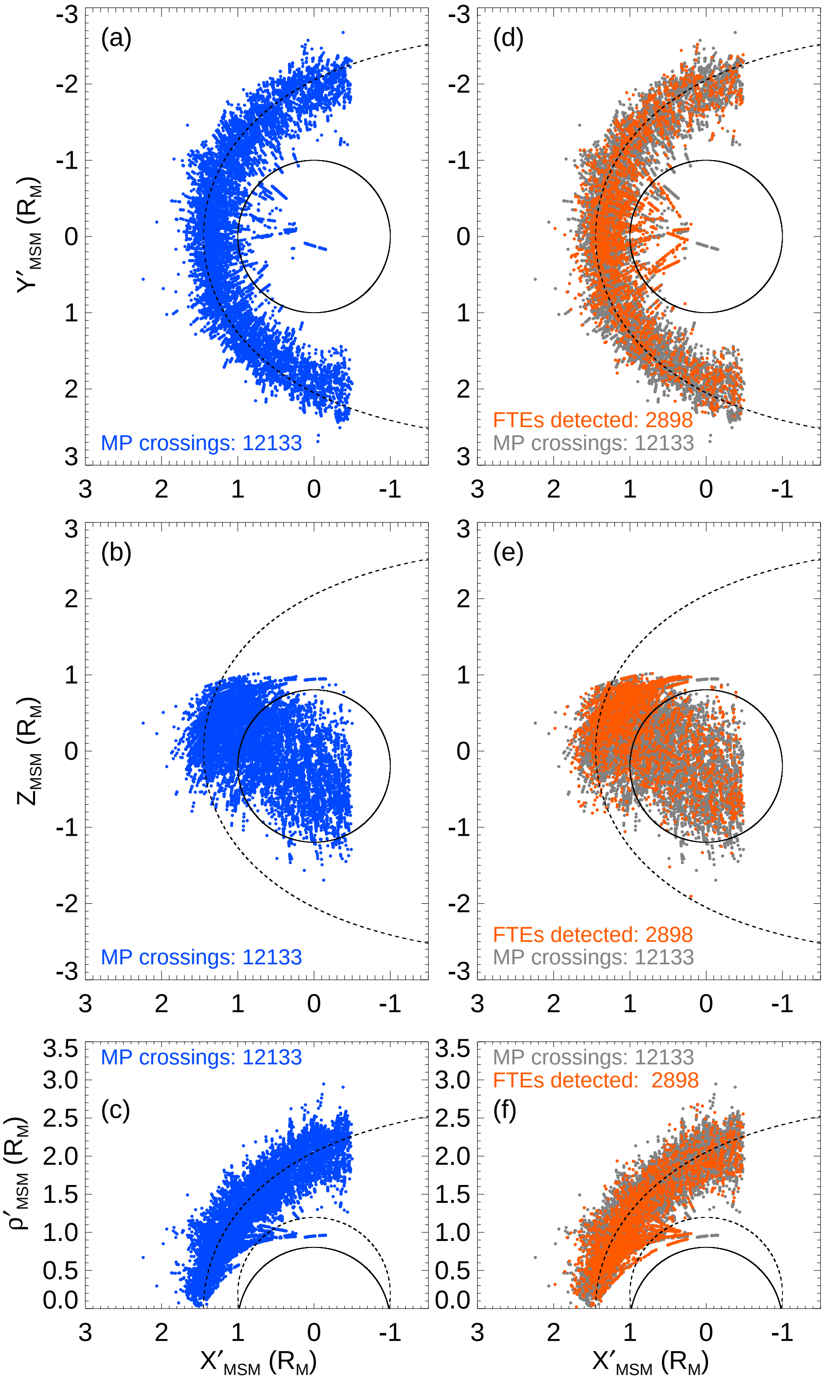

Figure 4.4: Locations of the magnetopause crossings in this study, projected onto the (a) $X'_{MSM} - Y'_{MSM}$, (b) $X'_{MSM} - Z'_{MSM}$ and (c) $X'_{MSM} - \rho'_{MSM}$ planes, where $\rho' = \sqrt{Y'^2 + Z'^2}$. The locations of the identified FTEs are shown in the same projections in panels (d-f), with the magnetopause crossings also indicated in grey for comparison. The model magnetopause location predicted by Winslow *et al.* [2013] is indicated by the dashed line.

highlighting the preference for observation near local noon. The strong peak at 12 MLT is to be expected for two reasons. Firstly, reconnection at the dayside magnetopause occurs most strongly near the sub-solar point. As discussed in Chapter 2, in cases where the reconnecting fields are not anti-parallel, a southward component in the magnetosheath field produces a tilted X-line that passes through the sub-solar point. As a result, FTEs in this MLT sector can be seen in the regions of the magnetopause covered by MESSENGER during a range of IMF orientations. Although FTEs can still form at all MLT, they may be at higher latitude towards the flanks, and therefore at locations not sampled by MESSENGER. Secondly, as the FTEs are transported anti-sunward over the poles of the planet, those formed further away from local noon at the northern edge of tilted X-lines move towards near-noon MLT sectors, where MESSENGER provided the best coverage at high latitude. Therefore, even those FTEs formed towards the flanks of the magnetosphere could still be observed by MESSENGER near local noon, during the high-latitude portions of its orbit.

In a previous study of a smaller number of events over a different time period, Imber *et al.* [2014] observed a larger number of FTEs in the dawn sector than the dusk, a bias that is only present to a small extent in these data. Figure 4.5a shows that between 8-16 h MLT, FTEs are seen approximately symmetrically about a central peak occurrence at 12 h MLT, where the main exception is between 11 and 13 h MLT. This asymmetry will be investigated and discussed in Section 4.4.

4.3.2 Influence of IMF clock angle on FTE formation

Many studies have investigated the parameters influencing dayside reconnection rates at Earth [e.g. Akasofu, 1981; Mozer & Retinò, 2007; Milan *et al.*, 2007, 2012; Newell *et al.*, 2007], however there has only been one such study at Mercury. DiBraccio *et al.* [2013] analysed the magnetic field data from 43 magnetopause crossings to determine a dimensionless reconnection rate, and concluded that for their dataset there was no significant variation with magnetic shear angle. The FTEs observed in this study were formed by reconnection on the dayside magnetopause, and given the high velocities of these structures observed at Earth, and the small spatial scale of the Hermean magnetosphere, it is reasonable to assume that the IMF direction had not changed significantly from the time of formation of the FTEs to their observa-

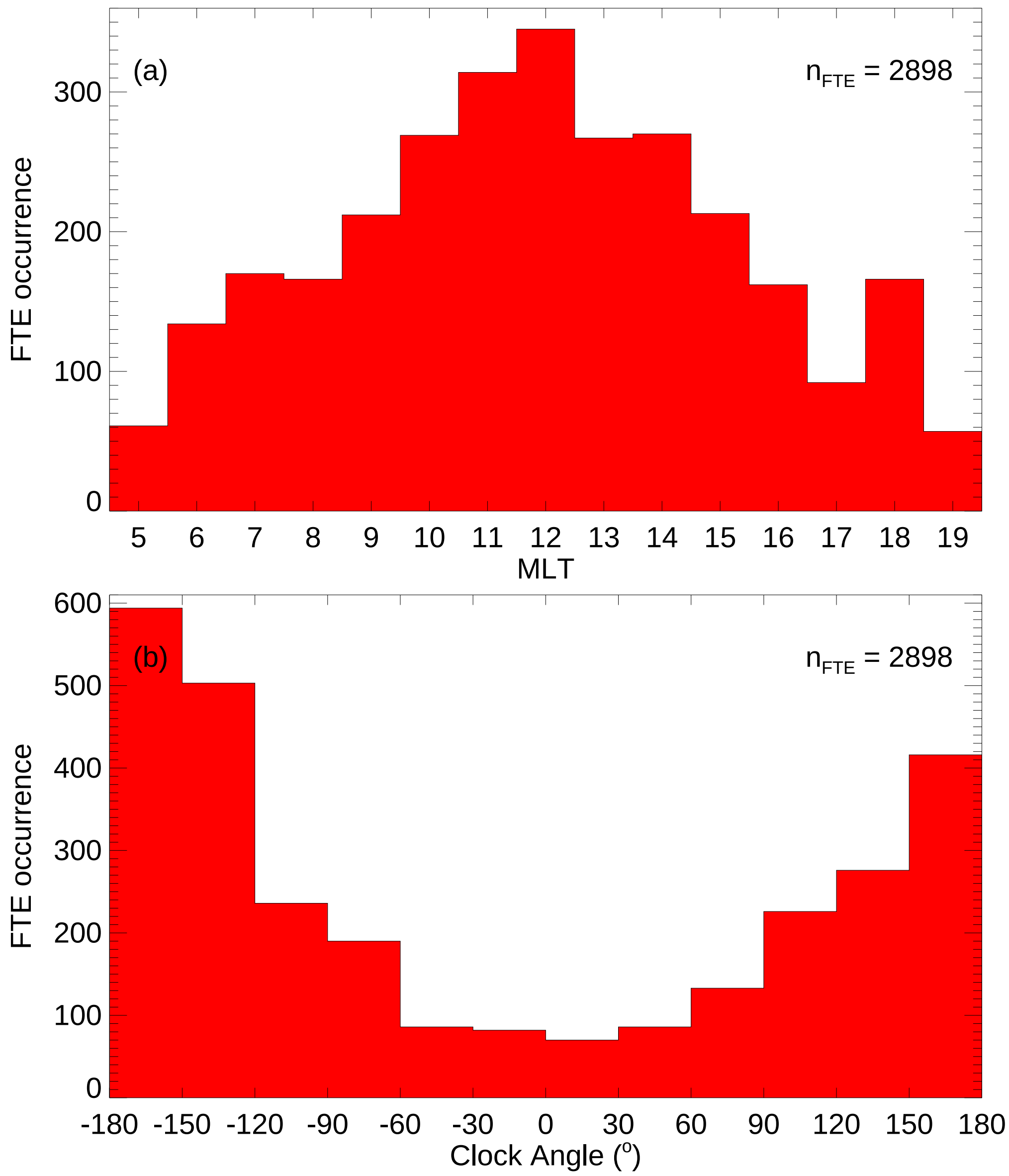

Figure 4.5: Histograms showing (a) the locations of the observed FTEs in MLT and (b) how the total number of FTEs observed varies with the clock angle of the IMF in the magnetosheath. The total number of events, n_{FTE}, is also indicated.

tion. Indeed, James *et al.* [2017] showed that on timescales on the order of minutes, the mean difference between magnetopause crossing and FTE detection, there is only a very small probability of a rotation in IMF angle of greater than 20°.

The orientation of the magnetosheath field was recorded over 1 minute just outside the outermost magnetopause crossing on each orbit to give a measurement of the clock angle in the magnetosheath, where 0° is directed northwards and +90° is directed towards $+B_{Y'}$. The total number of FTEs in each 30° bin has been plotted in Figure 4.5b. In agreement with studies at equivalent locations in the Earth's magnetosphere [Kawano & Russell, 1997b; Sibeck *et al.*, 2005, e.g.], this shows a clear general trend towards greater FTE occurrence during intervals of near-southward IMF, and therefore nearly anti-parallel fields, although any potential statistical bias introduced by multiple FTEs in a single pass or an uneven distribution of observed IMF orientations needs to be accounted for.

A histogram of the occurrence frequency of the magnetosheath clock angle for every pass on which at least 1 FTE was observed is presented in Figure 4.6a. Multiple FTEs observed on a single pass are therefore grouped into a single event, resulting in a similar distribution to that presented in Figure 4.5 with some asymmetries removed. FTEs were observed on 1197 of the 3085 total passes inspected, during which 12133 magnetopause crossings were detected, and Figure 4.6b shows the distribution of clock angles observed across all magnetopause encounters. The approximately equal coverage of all clock angle orientations indicates that large variations in observation rates cannot be attributed to a bias introduced by small sample size. By dividing the values in Figure 4.6a by those in Figure 4.6b the percentage occurrence of at least 1 FTE is obtained for each clock angle, as indicated in Figure 4.6c.

For clock angles close to zero, indicating a magnetosheath magnetic field pointing approximately along the positive $B_{Z'}$ axis, FTEs have been detected on only $\sim$15% of passes, whereas for near-southward IMF the observation rate increases to $\sim$65%. During periods of northward IMF, the reconnection X-line is expected to exist tailward of the cusp regions, therefore we would not expect to observe any FTEs generated at low latitudes near the dayside magnetopause. However, MESSENGER's orbit samples significant portions of the high latitude magnetosphere, so we would still expect to observe FTEs that have formed under northward IMF if reconnection is taking place in these locations. The distribution seen in Figure 4.6 can therefore again not be attributed to sampling bias, but represents a true indication of the formation preference for FTEs at Mercury during near-southward magnetosheath conditions.

Out of a total of 3085 passes, events exhibiting the required magnetic field sig-

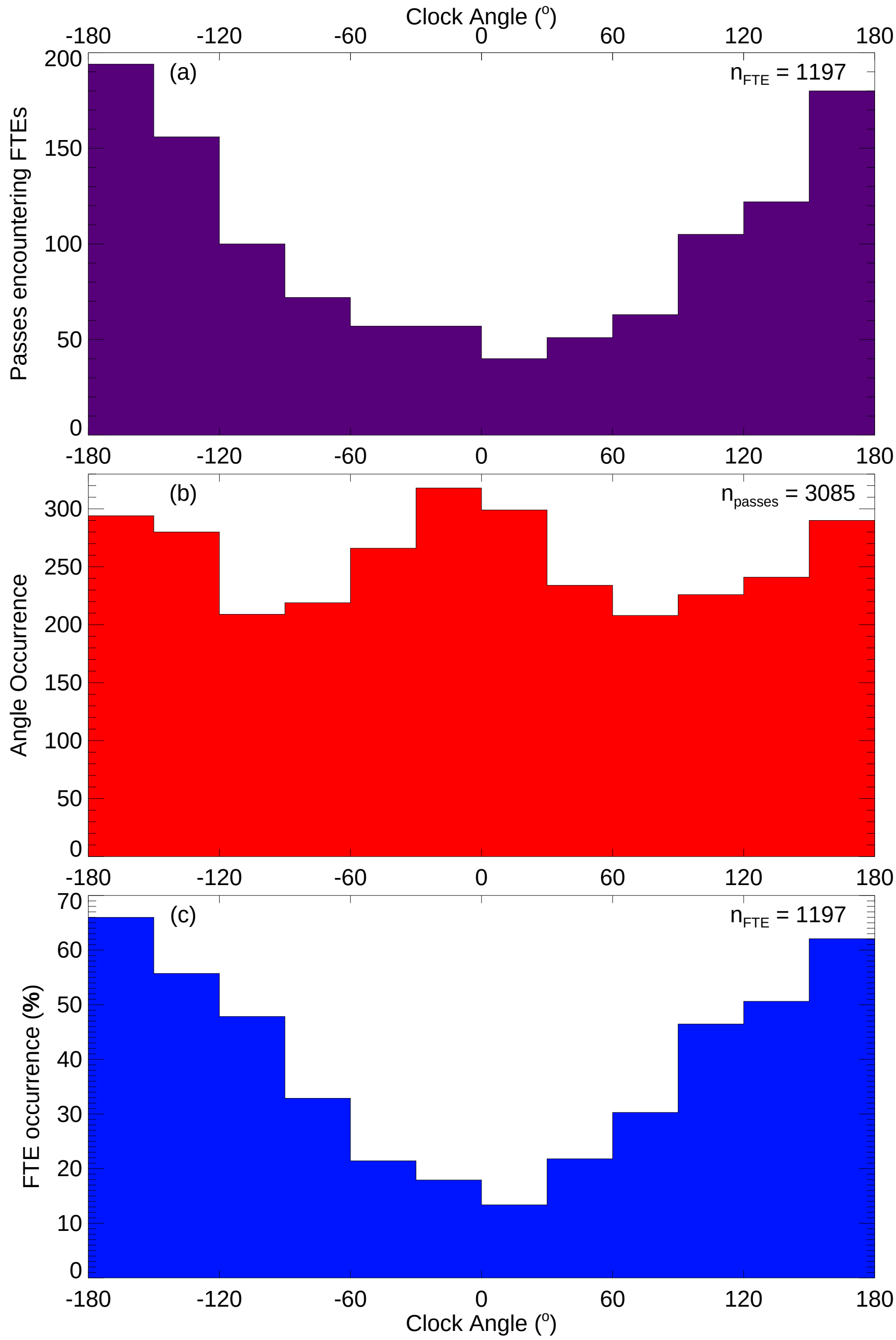

Figure 4.6: Histograms showing (a) the number of passes during each IMF orientation for which at least 1 FTE was observed, (b) the occurrence of each clock angle, and (c) percentage of magnetopause crossings under each IMF orientation during which at least 1 FTE was observed. The number of passes with at least 1 FTE, n_{FTE}, is indicated, along with the total number of passes examined, n_{passes}.

nature were observed on 1197, although many passes contained multiple events. Considering how ubiquitous FTEs have been found to be at Mercury in previous studies [Slavin *et al.*, 2012; Imber *et al.*, 2014], this ratio is perhaps lower than expected. However, the formation of FTEs at the dayside magnetopause has been shown to be significantly less likely during northward IMF, and these orientations contribute a substantial portion of the data examined here, as shown in Figure 4.6b. Therefore, the higher ratios seen in previous studies could be explained by an IMF orientation during those periods that is more favourable for FTE formation. Furthermore, in requiring a clear increase in the core field component, the sample has been restricted to those events for which MESSENGER entered the flux rope directly. As a result, many events exhibiting similar features have not been included, such as the travelling compression regions identified by Slavin *et al.* [2012].

There are several reasons why the results presented here contrast so strongly with those observed by DiBraccio *et al.* [2013]. First of all, although the formation of FTEs requires reconnection, the reconnection rate itself is not measured here, so it is difficult to directly compare the results. Secondly, the sample size used by DiBraccio *et al.* [2013] was considerably smaller than that utilised here. The large dataset investigated over a long time interval in this study is likely to have averaged out the effects of other parameters, thereby producing a more accurate reflection of how the IMF orientation alone influences the observation rate of FTEs at Mercury. Furthermore, the analysis performed by DiBraccio *et al.* [2013] utilised only crossings with a well defined normal direction to the magnetopause, as determined from minimum variance analysis of the magnetic field data. During strong reconnection at high shear angles, if an FTE is present at the magnetopause crossing the normal may be poorly defined, resulting in that crossing being excluded from the analysis. The high shear angle data included by DiBraccio *et al.* [2013] may therefore comprise mainly crossings during which other factors, such as a high plasma beta, inhibit the rate of reconnection. As a result, the high-shear reconnection rate calculated in that study may not represent the true rate of reconnection for such IMF orientations, which in general would be much higher. On the other hand, the low-shear reconnection rates calculated by DiBraccio *et al.* [2013] may represent an upper limit on the general values, due to those particular crossings occurring during favourable conditions such as a low plasma beta enabling reconnection across a wider range of shear angles.

4.4 Comparison of MESSENGER orbital phases

The analyses in this chapter were initially performed on data obtained only during the early phase of MESSENGER's orbit, and although the results presented in Figure 4.6 show very little variation from that initial period, the same is not true for the distribution of FTE observations in MLT. Figure 4.7 shows the same distribution as in Figure 4.5a in red, for the full 12 Hermean years included in the above analysis, and the blue histogram shows a subset of those data, containing results from the first 5 Hermean years of MESSENGER's orbit, up to 6 June 2012.

Despite a large sample size of 1111 FTEs, and an integer number of Hermean years ensuring approximately even coverage of all MLT sectors, the distribution of events shown in blue from the initial period of the mission does not exhibit the same clear peak near local noon as is seen for the larger dataset. Whilst significantly more FTEs are seen between 9-15 h MLT than further tailward, there is no obvious trend in the distribution within these sectors. Given the clear dependence on IMF orientation evidenced by Figure 4.6c, the slightly smaller sample size could be susceptible to certain more favourable IMF orientations occurring at 10 h or 15 h MLT, therefore producing the larger observation rates in these sectors than would be expected.

Figure 4.8 demonstrates the differences between the first 5 Hermean years and the entire dataset, with a further breakdown into cases for which the IMF had a positive or negative B_Z component. Figure 4.8a shows the total time spent in each MLT bin by MESSENGER during the two periods, where dark blue and light blue indicate passes for which the magnetosheath field had a northward or southward component respectively, during the initial phase, and the red and orange bars differentiate likewise for the full 12 Hermean year dataset. The axes have been scaled to allow for more direct comparison across the range of MLT sectors, but whilst some small proportional differences exist both between the two time intervals and the northward-southward distinction within an interval, they are mostly insufficient to explain the temporal and spatial differences seen in Figure 4.7.

Panel (b) indicates the number of FTEs observed in each MLT bin, similar to

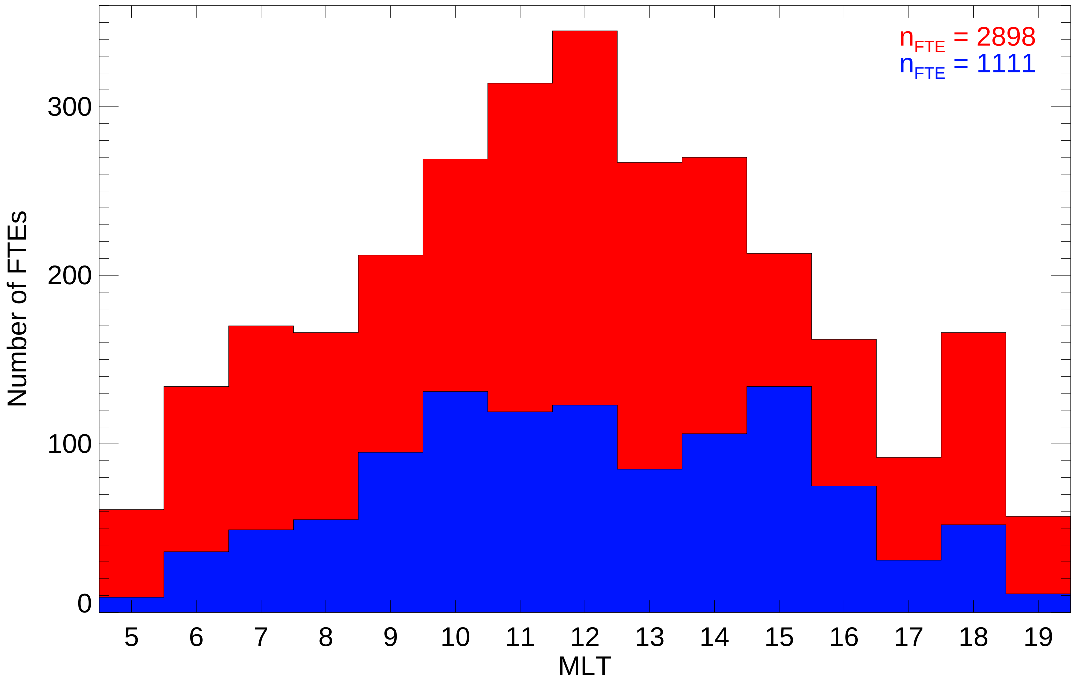

Figure 4.7: Histogram showing the distribution of FTEs in MLT. The full dataset is included in red, replicating the results shown in Figure 4.5a, and a subset including only the first 5 Hermean years of the MESSENGER mission, up to 6 June 2012, is overplotted in blue. The total number of FTEs in each dataset is indicated by n_{FTE}.

Figure 4.7, but separating out into the counts on passes with either a northward or southward IMF. This further highlights the clear preference for FTE formation when the magnetosheath B_Z is negative. Given the slight variability in dwell time at each MLT, the FTE counts have been normalised to produce the histogram of FTE observations per hour dwell time, shown in Figure 4.8c. Here, the Y-axes for the two intervals have the same scaling, indicating no significant change in overall observation rates throughout the dataset, but some important spatial differences exist between the two intervals.

Considering initially the FTEs seen during northward IMF, two bins stand out as exhibiting clear temporal variations. Although the count rate in most MLT sectors is no higher than 0.7 h^{-1}, at 14-15 h MLT during the years 1-5 of the mission, the mean observation rate increases drastically. These statistics are skewed entirely due to a single spacecraft pass that traversed both MLT bins. On 22 September 2011, an interplanetary coronal mass ejection (ICME) encountered Mercury, compressing the dayside magnetosphere very close to the planet such that the MESSENGER's

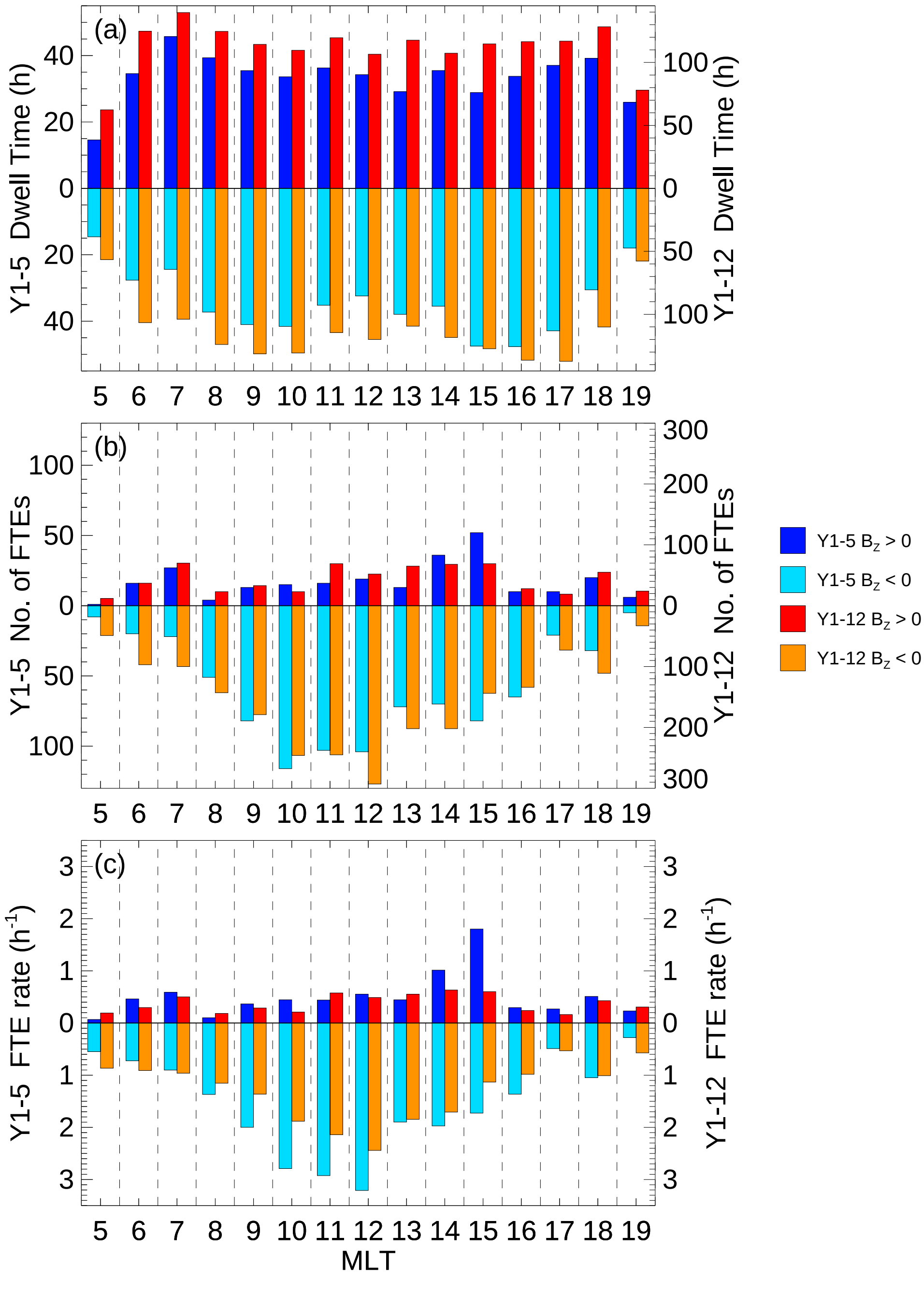

Figure 4.8: Histograms showing (a) the total time spent in each MLT sector by MESSENGER, (b) the number of FTEs observed, and (c) the mean rate of FTE observations per hour spent in each bin. In each panel, the dark blue and light blue bars indicate the values for IMF with a positive and negative B_Z component respectively, for the first 5 Hermean years, whilst red and orange bars indicate the same breakdown of IMF orientation for the entire 12 year dataset analysed in this chapter. The left axis in all plots therefore applies for dark and light blue values, whilst the red and orange values are counted on the right axis.

trajectory carried it directly into the northern magnetospheric cusp, with significantly enhanced magnetosheath field strength. On this one pass alone, 45 FTEs were identified, therefore producing the disproportionately large peaks in the blue histogram of Figure 4.7 at 14-15 h MLT compared to the full years 1-12 distribution.

The high count rates at 9-11 h MLT during the first 5 years can be explained by Figure 4.8c, without any anomalous results. The rate of FTE observations during southward IMF during this period is considerably greater than the mean rate over the full 12 year interval, despite most other MLT bins very closely resembling the full mean rate. During the interval spanning MESSENGER orbital insertion to 6 June 2012, the IMF orientation in the inner heliosphere was biased strongly towards clock angles of -90° [James *et al.*, 2017; Lockwood *et al.*, 2017]. This has important consequences for the observation of FTEs at Mercury, particularly given the orbital characteristics of MESSENGER. Although the strong bias in the IMF is somewhat reduced by rotation of the magnetic field vector across the bow shock, the subsequent magnetosheath field still exhibits a preference for negative $B_{Y'}$, an effect that is still seen in the total angle occurrence shown in Figure 4.6b for the entire dataset, wherein the left hand side has slightly higher count rates than the corresponding $B_{Y'} > 0$ clock angles on the right. The preference for a negative $B_{Y'}$ component leads to fields that are more anti-parallel at the pre-noon high northern latitude (and post-noon high southern latitude) magnetopause during periods of southward magnetosheath field. The tilted X-line therefore also passes through those MLT sectors at higher latitudes, also producing enhanced reconnection signatures, compared to a purely southward magnetosheath field. As MESSENGER's orbit samples almost exclusively the northern hemisphere of the dayside magnetosphere, it therefore encountered only the pre-noon region of enhanced reconnection, providing the optimum opportunity to observe the resultant FTEs. This causes the enhanced observation rates that skew the peak of the distribution towards pre-noon for the period up to 6 June 2012. The difference seen between 11 and 13 h MLT for the full dataset is due entirely to the pre-noon preference during the first 5 Hermean years, with the remaining 7 years seeing an approximately equal distribution in these locations.

4.5 Discussion

In this section, the main results of the chapter are discussed specifically in relation to previous work at Mercury. Additionally, context is provided in the form of a comparison with studies at Earth, discussing any similarities and differences between the results seen at the two planets.

Since the first observations of FTEs at Earth, numerous authors [e.g. Berchem & Russell, 1984; Kuo *et al.*, 1995; Kawano & Russell, 1997b] have shown that they occur more frequently when the upstream IMF has a southward component. This result is in agreement with the more general understanding of enhanced reconnection rates during periods of anti-parallel fields at the magnetopause between a southward IMF and the northward planetary magnetic field [e.g. Fairfield & Cahill, 1966; Perreault & Akasofu, 1978]. However, in the only previous investigation of IMF orientation influence at Mercury, DiBraccio *et al.* [2013] observed similar reconnection rates at all clock angles. The results presented in this chapter therefore provide important evidence in support of Mercury's magnetosphere exhibiting a similar response to different IMF clock angles as does Earth's, at least in regard to dayside reconnection and the production of FTEs. The discrepancy with the results seen by DiBraccio *et al.* [2013] can be explained by the small sample size in their study allowing for other factors having a greater effect, as discussed in Section 4.3.2.

The large sample size of FTEs examined in this chapter using 4 years of data has also enabled an investigation into the MLT distribution of FTEs in Mercury's magnetosphere. There have been very few studies investigating this at Earth, but Wang *et al.* [2005] observed a slight asymmetry between dawn and dusk, a result also observed at Mercury by Imber *et al.* [2014]. The work presented in this chapter shows a clear peak at local noon, although there is a slight asymmetry between the pre-noon and post-noon sectors. This is a Parker spiral effect, with a significant bias towards IMF $B_{Y'}$ during the first year of MESSENGER's orbit [James *et al.*, 2017; Lockwood *et al.*, 2017] resulting in increased FTE formation in the pre-noon sector during this period and also explaining the asymmetry seen by Imber *et al.* [2014].

4.6 Summary

This chapter has presented a statistical analysis of flux transfer events observed in the dayside magnetosphere of Mercury by the MESSENGER spacecraft during the first 12 Hermean years of its orbit. 3085 passes of magnetic field data taken by the MESSENGER spacecraft were visually inspected for FTE signatures near the dayside magnetopause encounters. Observation of FTEs is shown to be strongly dependent on the orientation of the IMF in the magnetosheath. FTEs with clear signatures were identified in 1197 of the 3085 passes through the magnetopause sunward of MSM $X' = -0.5\ R_M$, with a total of 2898 events observed. During periods of near-southward IMF at least 1 FTE was observed on $\sim$65% of passes, whereas during northward IMF the observation rate is only $\sim$15%.

The spatial distribution of the identified FTEs peaks strongly at a magnetic local time of 12 h, with an approximately symmetric distribution either side of local noon. The main asymmetry occurs between 11 and 13 h MLT, due to a preference for pre-noon formation of FTEs during the first 5 Hermean years of MESSENGER's orbit as a result of a duskward IMF bias leading to more closely anti-parallel fields in the northern hemisphere in the pre-noon sector.

The identified magnetopause crossings agree well with the Winslow *et al.* [2013] model for large parts of the dayside magnetosphere, albeit with significant spread in the observed crossing locations. This spread is attributed predominantly to seasonal effects caused by the eccentricity of Mercury's orbit around the Sun, whereby the magnetopause crossings occur at lower altitudes during perihelion as a result of stronger magnetospheric compression.

This study represents an important contribution to the investigation of factors influencing reconnection and flux transfer event formation, confirming that the observed clock angle dependence seen at Earth is also present at Mercury. The large dataset of events compiled for this investigation also provides an excellent opportunity for further investigations into the evolution of FTEs at Mercury after their formation, and how their subsequent motions are affected by the prevailing magnetosheath conditions.

Chapter 5

Orientation and Motion of Flux Transfer Events During Different IMF Orientations

5.1 Introduction

The motion of open magnetic field lines over the poles of the planet as part of the Dungey cycle following reconnection at the dayside magnetopause transports a large quantity of magnetic flux into the magnetotail. Because flux transfer events are generally magnetically connected to both the magnetospheric field and the IMF in the magnetosheath, they can therefore be extremely useful tools in determining the motion of field lines as they convect tailward. The magnetic field signature produced by an FTE as it passes over a spacecraft provides information about both its orientation and direction of motion, and therefore describes how flux ropes evolve as they are transported away from the reconnection site by the magnetic tension force and the anti-sunward motion of the IMF in the magnetosheath.

Previous work at Earth has shown that FTEs observed in the northern hemisphere move predominantly northward, and conversely in the southern hemisphere, as discussed in Chapter 2 [e.g. Baumjohann & Paschmann, 1987]. This indicates a reconnection X-line lying azimuthally near the magnetic equator, however for strongly dawnward or duskward IMF the X-line is seen to tilt clockwise or anti-clockwise respectively [e.g. Korotova *et al.*, 2012]. In this chapter, the FTEs identified in Chapter 4 are investigated similarly, providing the first analysis of X-line location and orientation at Mercury.

Section 5.2 introduces two different methods for determining the direction of motion of FTEs, discussing the benefits of each. The results are presented initially in Section 5.3, where the orientation of the X-line is inferred for different magnetosheath IMF clock angles, before more precise travel directions are utilised in Section 5.4 to provide a proxy description of the nature of magnetospheric convection at Mercury.

5.2 Methods for determining orientation and motion of flux transfer events

As discussed in Chapter 2, multi-spacecraft analysis provides the most reliable and accurate method for determining the scale, orientation and motion of FTEs, however alternative methods do allow for good estimations of some of these properties using measurements from only one spacecraft, as is the case for MESSENGER at Mercury. These utilise two different coordinate systems, introduced in Chapter 1.6: minimum variance, and boundary normal coordinates. These are discussed in greater detail here, including an analysis of the benefits and difficulties of both methods.

5.2.1 Minimum variance analysis of the magnetic field

Minimum variance analysis (MVA) of the magnetic field was originally developed as a method for determining the normal to a transitional current layer such as the magnetopause, using single-spacecraft measurements. It takes a time series of magnetometer data, and calculates the magnetic variance matrix with three orthogonal eigenvectors corresponding to the directions of maximum, intermediate and minimum variance of the magnetic field. In the case of a transition layer, the minimum variance direction represents the best estimate for the normal to the layer, but MVA can also be performed to determine the structure of a flux rope. However, the physical significance of the intermediate and maximum variance directions is not necessarily the same for all FTEs, making accurate identification of the flux rope structure and orientation difficult. In most cases, the magnetic field along the maximum variance direction exhibits a bipolar signature, such that the core field of the FTE is aligned closely with the intermediate variance direction. For non-force free flux ropes, however, where there is also a large axial field, the maximum variance direction best describes the core direction of the FTE. In both cases, the minimum variance direction completes the right-hand set by providing the best indicator of the axis along which the FTE is travelling. This is seen most clearly for an encounter with a cylindrical FTE, in which the spacecraft passes directly through the centre of the flux rope's cross-section, with an impact parameter of zero. In this instance, there will be no magnetic field component along the direction of travel of the FTE, at any point inside the flux rope. The minimum variance direction will therefore align perfectly with the travel direction, with a variance of zero along this axis.

Figure 5.1 shows an example FTE identified on the basis of its signature in MSM′ coordinates, plotted in panels (a-c), along with the total magnetic field strength in (d). The vertical dashed lines indicate the start and end times of the FTE, the interval for which minimum variance analysis was performed. The magnetic field components along each of the resultant axes are plotted in Figure 5.1e-g, along the directions of maximum, intermediate and minimum variance respectively. Also indicated are the eigenvectors in MSM′ coordinates, given in brackets, and the corresponding eigenvalues. Magnetic hodograms indicating the relationship between the components along maximum and minimum (Figure 5.1j), and maximum and intermediate (Figure 5.1k) variance directions are also shown.

The minimum variance axis is extremely well-defined for this event, as evidenced by the hodogram in Figure 5.1j and the ratio of intermediate to minimum eigenvalues of 504. The clear rotation present in panel (k) represents the rotation of the magnetic field as the flux rope passes over MESSENGER. However, the intermediate and maximum variance directions are less well-defined, with an eigenvalue ratio of only 1.49. This is a by-product of the relatively weak bipolar signature, with a peak-to-peak amplitude of only ~ 50 nT, compared to a core field amplitude of over 70 nT,

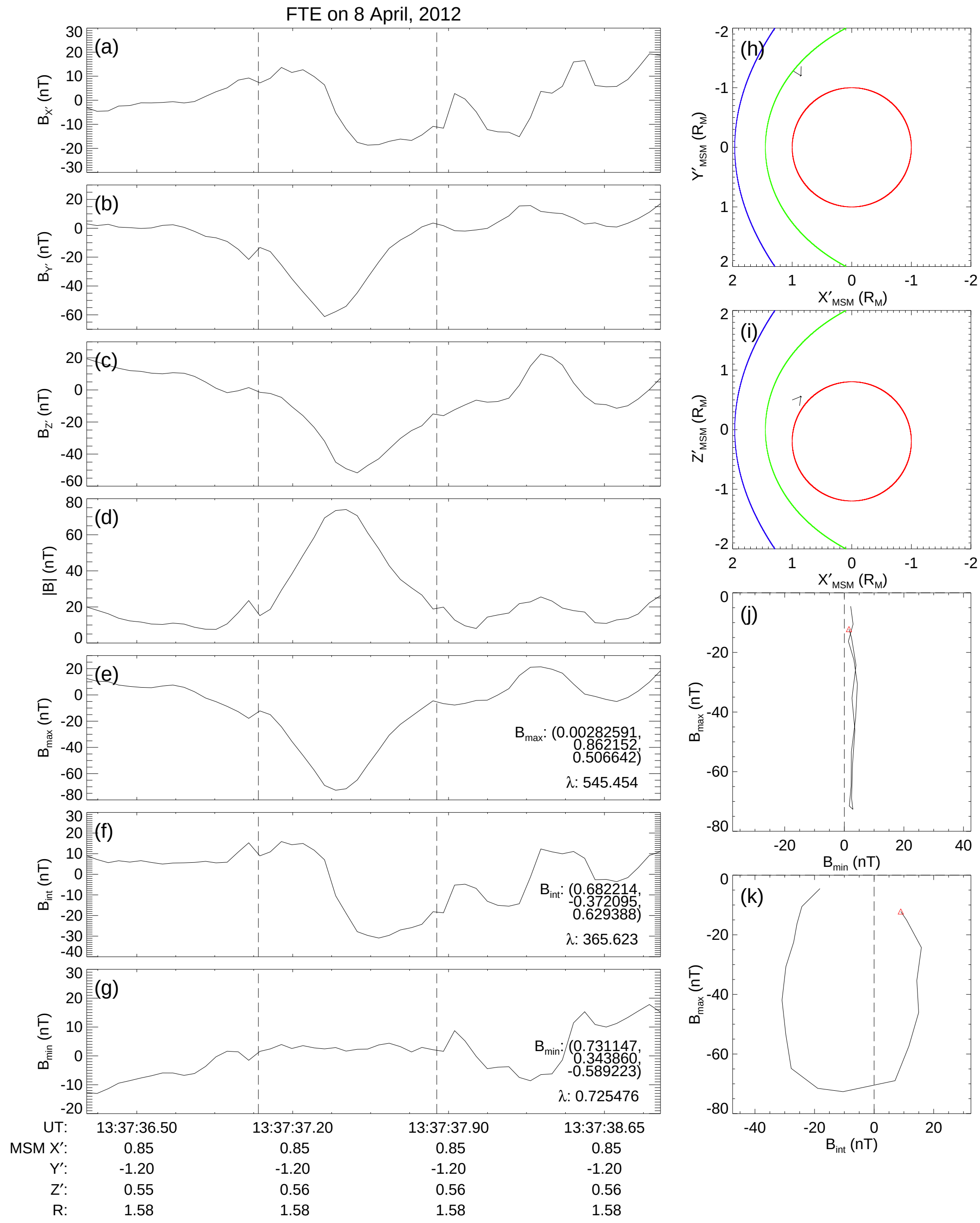

Figure 5.1: Example MESSENGER Mag data during an identified flux transfer event on 8 April 2012. Panels (a-d) show the magnetic field in MSM′ coordinates. These data are then projected into the directions of maximum (e), intermediate (f), and minimum (g) variance. The respective eigenvectors are given in MSM′ coordinates in each panel, with the eigenvalue shown in the bottom line. MESSENGER's trajectory during the interval is indicated by an arrowhead projected onto the MSM Y'-X' (h) and Z'-X' (i) planes. Hodograms of the (j) maximum and minimum variance, and (k) maximum and intermediate variance eigenvalues are also presented, showing a clear rotation in the magnetic field vector as MESSENGER traversed the flux rope. The red triangle in both (j) and (k) indicates the start of the interval marked by the vertical dashed lines in (a-g), which denote the interval for which minimum variance analysis was performed.

such that the maximum variance axis lies along the axial direction of the flux rope.

Figure 5.2 shows an example of another FTE, following the same format as Figure 5.1. The main difference between the two events is that despite the extremely large core field of $|B_{core}| = 180$ nT, the maximum variance axis is aligned with the bipolar signature, due to the large peak-to-peak amplitude of 170 nT. Both axes are also well-defined, as shown by the eigenvalue ratio of 3.45. Once again, a clear rotation is evident in the maximum and intermediate variance hodogram, reflective of the helical nature of the flux rope. The minimum variance direction is again extremely well-defined, albeit less so than for the event in Figure 5.1, with an intermediate-to-minimum eigenvalue ratio of 7.76.

The two events shown in Figures 5.1 and 5.2 highlight the major difficulty in using MVA to describe the orientation and motion of FTEs: despite producing precise coordinate axes, they do not consistently describe the same axes of different flux ropes. Further complications are caused by the coordinate axes having an arbitrary sense, such that the minimum variance direction could be either parallel or anti-parallel to the direction of motion of the FTE, and similarly for whichever axis lies along the core field direction. Indeed, in both examples presented in Figures 5.1 and 5.2, the large negative peak in the core component indicates that the respective axes are anti-parallel to the core field. Further factors must therefore be considered before the FTE properties can be determined from MVA results.

Figure 5.3 shows the magnetic structure of two flux ropes moving in opposite directions, and with helical fields of opposite polarity. Flux rope (a) has right-handed helicity, and moves northward past a spacecraft, producing a standard bipolar signature in B_X, with a positive then negative deflection. The core field of the flux rope produces a peak in the B_Y component. However, an identical signature would be produced by a left-handed helicity flux rope (b) moving southward past the spacecraft. In order to determine whether the direction of motion of an FTE is parallel or anti-parallel to the minimum variance direction, the helicity of the flux rope must therefore be known.

Identifying helicity is only possible, however, by making certain assumptions about the nature of the events. Firstly, given the strength of Mercury's magneto-

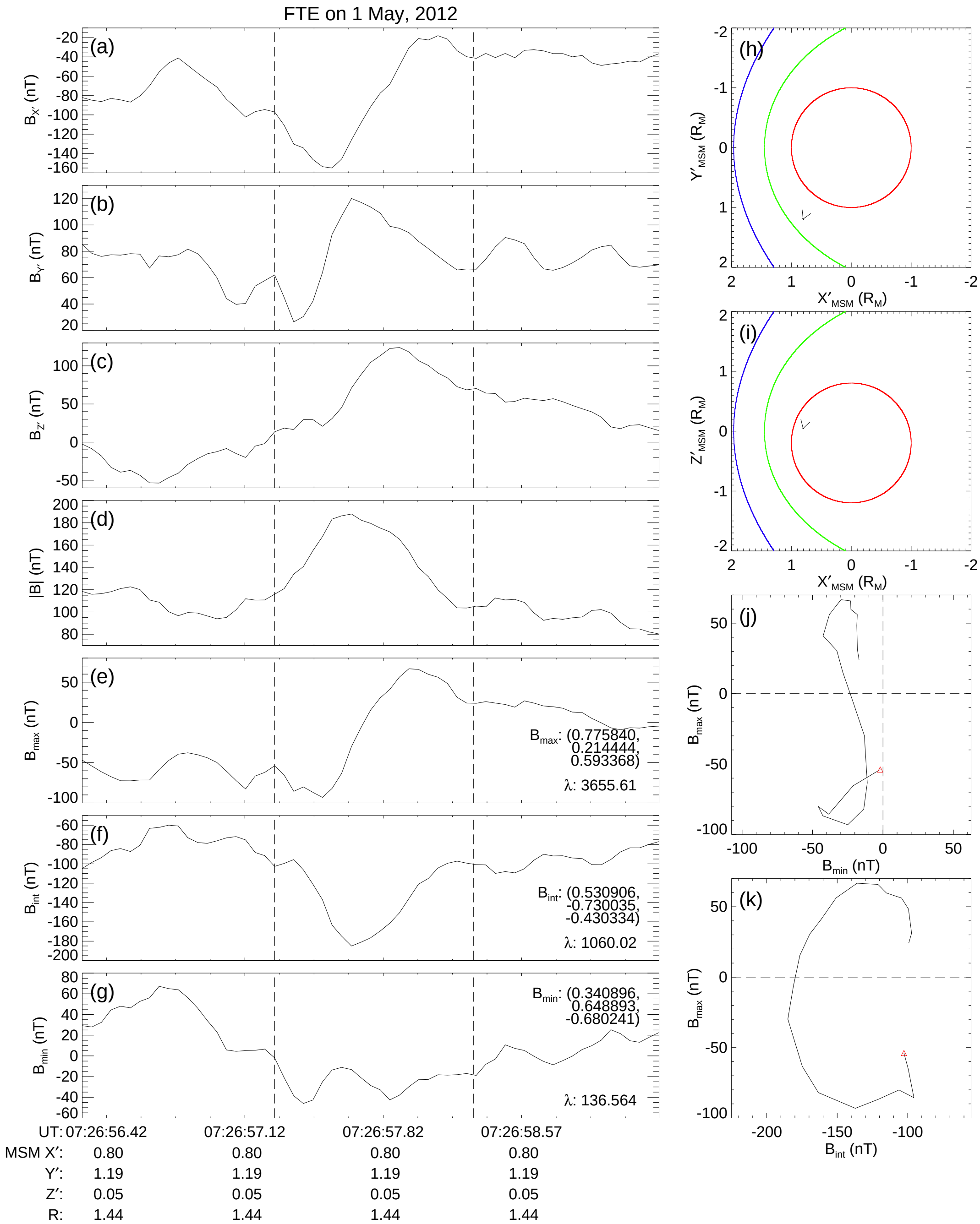

Figure 5.2: Example MESSENGER Mag data during an identified flux transfer event on 1 May 2012. The format is the same as in Figure 5.1.

spheric field, it is assumed that for all FTEs the planetary side of the helical field has a positive B_Z component, aligned with the planetary field. Additionally, events located near the flanks of the magnetopause are assumed to be carried by the draped magnetosheath IMF, and therefore only travel tailward.

By first fitting a sinusoid and a gaussian to both the intermediate and maximum

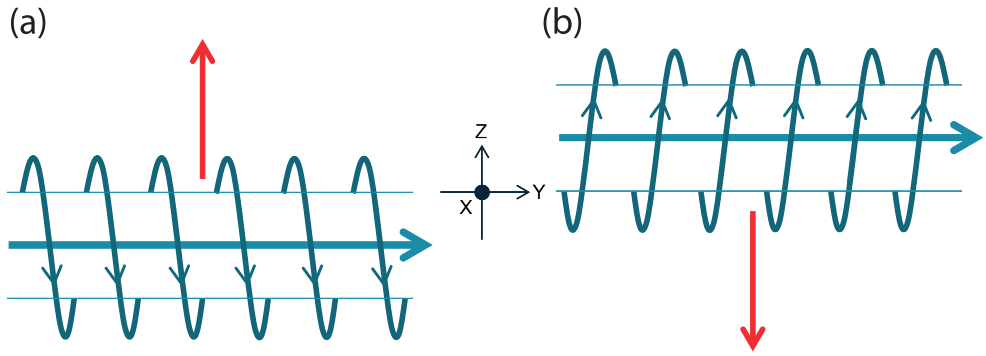

Figure 5.3: Schematic showing the magnetic structure of (a) right-hand, and (b) left-hand helicity flux ropes, moving in opposite directions, as denoted by the red arrows. In both cases, the flux ropes will produce a peak in the B_Y component, and a standard polarity (+/- deflection) bipolar signature in B_X as they pass over a spacecraft.

variance components of each FTE, the bipolar signature and core field direction can be identified. Any events for which the MVA axes are sufficiently degenerate that no clear fit to both a core field and a bipolar signature can be made are removed from the analysis at this stage. From the calculated core component of the remaining events, the helicity is then calculated based on the above assumptions, and the correct direction of travel is obtained.

5.2.2 Bipolar signature in boundary normal coordinates

Given the difficulties in identifying the direction of motion from MVA, either through a poorly defined coordinate system or an FTE orientation that makes calculating the helicity impossible, an alternative method has also been employed to describe the motion of FTEs in the dayside magnetosphere. Whilst not as precise as an accurate MVA result, analysing the sense of the bipolar signature in boundary normal coordinates more robustly identifies whether an event is moving northward or southward past MESSENGER. This method has been utilised regularly at Earth [e.g. Berchem & Russell, 1984; Kawano & Russell, 1997b; Korotova *et al.*, 2012; Fear *et al.*, 2012b] in similar investigations to the one presented in this chapter for Mercury.

The local boundary normal (LMN) coordinates, as introduced in Chapter 1, are first calculated using the Winslow *et al.* [2013] magnetopause model. The magnetic field components are then projected onto the magnetopause normal (**N**). If a bipolar signature is present, the sense of the deflections is used to assign either a northward or southward motion to the event: standard polarity (positive-to-negative) signatures indicate an FTE moving northward past MESSENGER, and conversely for reverse polarity events.

5.3 Inferring the average X-line orientation

The initial dataset of 2898 FTEs identified as described in Chapter 4 was analysed for the sense of the bipolar signature in B_N, as detailed in Section 5.2.2. For 424 events, B_N exhibited a unipolar peak indicating that the core field of those FTEs was closely aligned with the magnetopause normal. The locations of the 2474 events with a clear bipolar signature in B_N are projected onto a plane of the model magnetopause in Figure 5.4a, colour-coded for the sense of the polarity. Orange dots denote the 1810 events with a standard polarity, suggesting a northward component to the motion, and the remaining 664 FTEs are shown in purple. The dwell time of MESSENGER in $5° \times 5°$ bins has also been calculated, with an additional distance filter to include only the time spent within 0.8 R_{MP} of the magnetopause, where R_{MP} is the distance to the Winslow *et al.* [2013] model magnetopause in the centre of each latitude-MLT bin. This value of 0.8 is somewhat arbitrary, but provides a good indication of MESSENGER's coverage of the near-magnetopause region, as indicated by the greyscale shading in Figure 5.4, where the vast majority of FTEs are observed, without filling the entire plot. The exceptions are the high-latitude FTEs seen near the northern cusp region. Although these events are observed deep into the magnetosphere, they are not as far away from the magnetopause as the lack of coverage would suggest, due to the model having a cylindrically symmetric magnetopause, and therefore not including an indentation in the cusp regions.

Figure 5.4a shows that not only are FTEs near Mercury's dayside magnetopause preferentially observed close to local noon, as seen in Chapter 4, but the majority of events are seen to travel northward. This is especially the case from 9-15 MLT, with very few events exhibiting a reverse polarity signature.

The preference for standard polarity events in this region is made even more

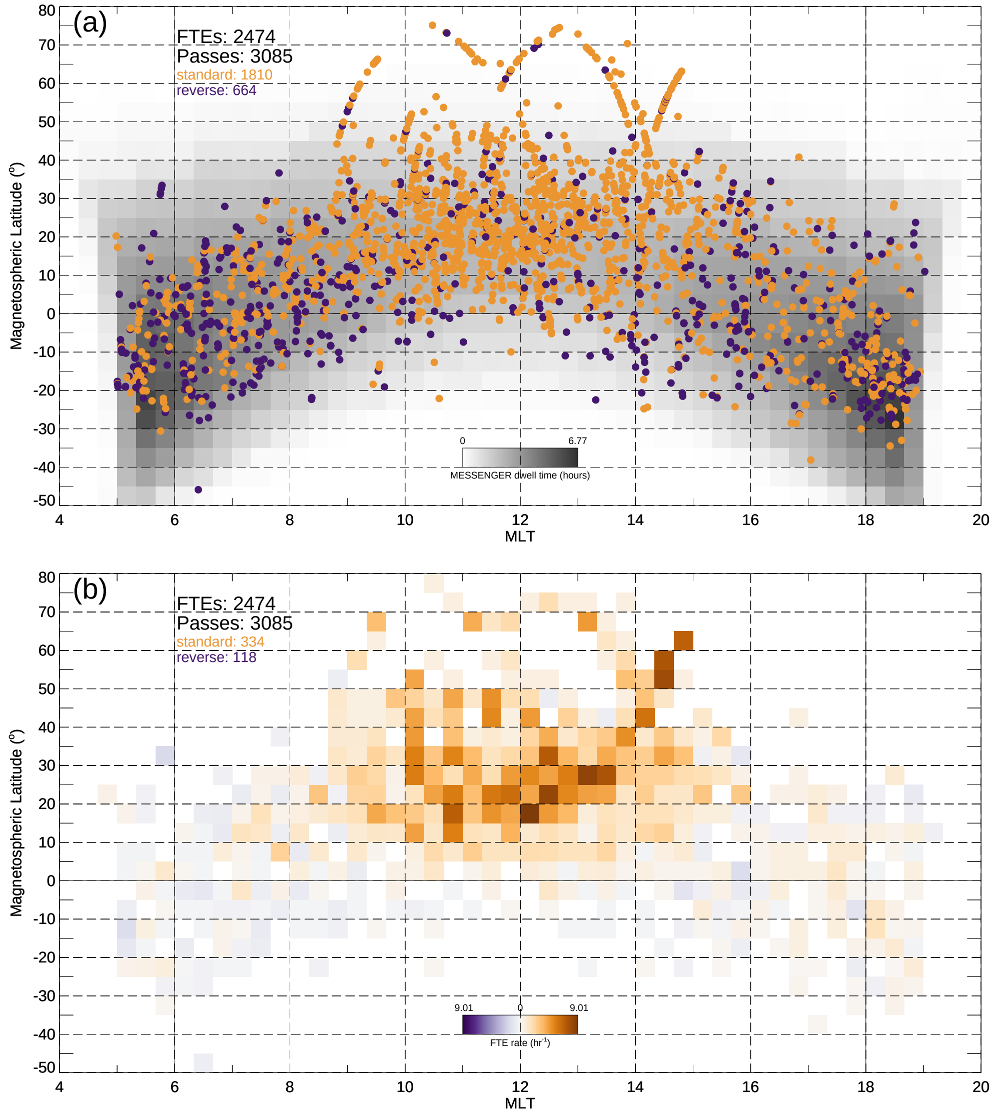

Figure 5.4: (a) The location of every FTE identified in this study projected onto the model Winslow *et al.* [2013] magnetopause. Events in orange are travelling northward, based on their B_N signature polarity, and those in purple are moving southward. Also indicated by the greyscale shading is the amount of time MESSENGER spent within 0.8 R_{MP} of the magnetopause, where R_{MP} is the distance to the model magnetopause. (b) The mean direction of travel and rate of observations per hour of FTEs, in the same plane as panel (a), now removing the restriction on MESSENGER's location. In both panels, the total number of passes and FTEs is indicated. The vertical solid lines indicate the terminator plane for reference, and the magnetic equator is also marked by a solid horizontal line.

evident in Figure 5.4b, where the FTE rate, R, is indicated for each spatial bin. The difference between the number of standard, N_S, and reverse, N_R, polarity events is divided by the total time, t_{dwell}, spent by MESSENGER in each bin, where the distance filter has been removed from the spacecraft coverage shown in Figure 5.4a:

$$R = \frac{N_S - N_R}{t_{dwell}}. \tag{5.1}$$

Orange bins therefore denote regions where more events are travelling northward than southward, and the reverse is true for purple bins. The shading shows that for the spatial coverage provided by MESSENGER, FTEs are three times more likely to be travelling northward in general, with 334 bins having a net northward rate compared to only 118 with a net southward observation rate. Furthermore, the peak rate of net northward events of 9.01 hr^{-1} is considerably greater than the maximum rate of southward moving events, only 1.74 hr^{-1}, indicating that not only are standard polarity signatures seen across a wider spatial range, but they also occur far more frequently than reverse signatures. This therefore suggests that for the locations sampled by MESSENGER, chains of multiple FTEs are considerably more likely to be travelling northwards than southwards.

Because MESSENGER's coverage of the near-noon local time sectors is predominantly in the northern magnetic hemisphere, the clear preference for standard signatures in this region is to be expected for an azimuthally-aligned reconnection X-line passing through the sub-solar point. However, further to the flanks of the magnetosphere, where MESSENGER spends increasingly longer in the southern hemisphere, the opposite is not true. Although most FTEs observed below the magnetic equator would be expected to move southward, and therefore produce a reverse polarity signature, there are still a significant number of northward-moving events observed south of the magnetic equator. Similarly, the FTEs observed in the northern hemisphere near the terminator, denoted by the solid vertical lines, are seen to be moving northward and southward in similar numbers. A significant dawnward or duskward component in the IMF has previously been shown to cause a tilting of the X-line at Earth, so the expected direction of motion of FTEs a large distance from the sub-solar point is likely to depend strongly on the orientation of the IMF at the time of formation.

Figure 5.5 shows a subset of the data included in Figure 5.4, focusing on passes for which the magnetosheath IMF clock angle was (a-b) $0 \pm 45°$ and (c-d) $180 \pm 45°$, as indicated by the arrow in the top right of each panel. In each case, the mag-

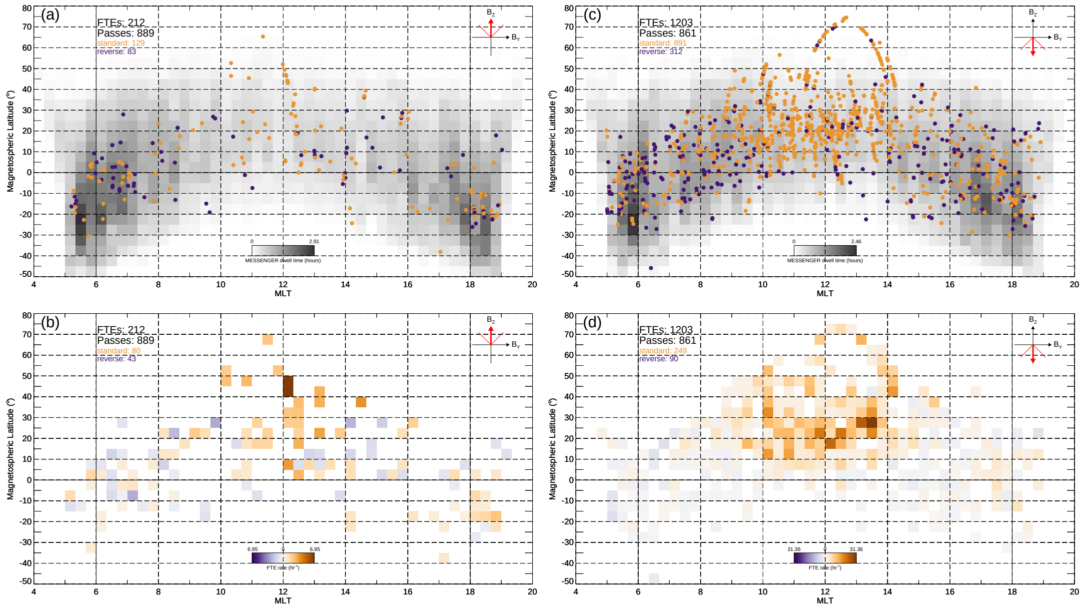

Figure 5.5: The location and direction of motion of FTEs, separated into those events seen during different IMF orientations. (a-b) follow the same format as Figure 5.4, but including only those FTEs observed on passes for which the IMF clock angle was within 45° of due north, as indicated by the arrow in the top right of each panel. Similarly, (c-d) show only those events and passes where the IMF in the magnetosheath was within 45° of due south. Care should be taken directly comparing the two orientations, as the colour scale has been normalised for each panel individually.

netosheath field was recorded over a 1 minute interval just outside the outermost magnetopause crossing on each spacecraft pass. It has already been shown in Chapter 4 that FTEs are far less likely to be observed at Mercury when the IMF has a strong northward component, and Figure 5.5a shows that out of 889 passes meeting the orientation criterion, only 212 FTEs were seen. Whilst a preference for standard polarity signatures is still evident, it is much less pronounced than in the unfiltered dataset. Of the 212 events, 61% are moving northward, a significantly smaller proportion than the 73% when considering events observed across all IMF orientations. Similarly, when the net rate of standard or reverse polarity events is calculated in spatial bins, standard signatures are only twice as likely across the whole magnetopause plane, as seen in Figure 5.5b.

This difference can be attributed largely to the lack of events observed near local noon in the northern hemisphere, the region seen in Figure 5.4 to be where standard signatures are most prevalent. Contrary to the result seen for all events in Figure 5.4a, FTEs during northward IMF are distributed evenly across all MLT sectors, with the largest number of events seen near the terminator on both magnetopause flanks. As a caveat to this, it should be noted that MESSENGER spent much more time during northward IMF in these locations than it did near local noon. This is likely a draping effect, whereby northward upstream IMF gains a larger B_Y component in the pre- and post-noon sectors as it wraps around the magnetopause, to the extent that it no longer falls within the angle range included in these plots. When the dwell time is taken into consideration, Figure 5.5b shows that the net rate of FTEs is generally higher in the northern hemisphere near local noon than near the terminator. However, the peak rate of 6.95 hr^{-1} for standard signatures is lower than the overall peak standard rate, reflecting the overall picture of less frequent FTE observations during northward IMF.

Due to the relatively low statistics, it is difficult to obtain a clear indication of the X-line location and orientation across the magnetopause during northward IMF. However, the lack of FTEs at low latitudes near local noon and the larger proportion of high latitude dayside and extreme flank events compared to the distribution of all FTEs supports the idea that unlike during southward IMF, these locations provide the most favourable conditions for reconnection during northward IMF.

The FTE distribution and net rate map shown in Figures 5.5c and 5.5d for southward IMF are very similar to the overall distributions. This is unsurprising given that approximately half of the total observed FTEs occurred during magnetosheath clock angles within the range included here. Indeed, Figure 5.5d shows that standard polarity signatures are almost three times more likely than reverse polarity across the magnetopause plane, reflecting the results seen for the entire dataset. The highest rates of northward-moving FTEs are seen at low latitude in the northern magnetic hemisphere, as would be expected for events observed shortly after their formation at a horizontal X-line passing close to the subsolar magnetopause. The change from predominantly northward to predominantly southward FTEs occurs near a northern magnetic latitude of 5°, although the comparatively low observation rates near the equator make determining the exact location of the reversal difficult. The peak net rate of just over 31 standard polarity FTEs hr^{-1} is 3.5 times higher than the maximum rate seen across the entire dataset, and the peak southward rate also a

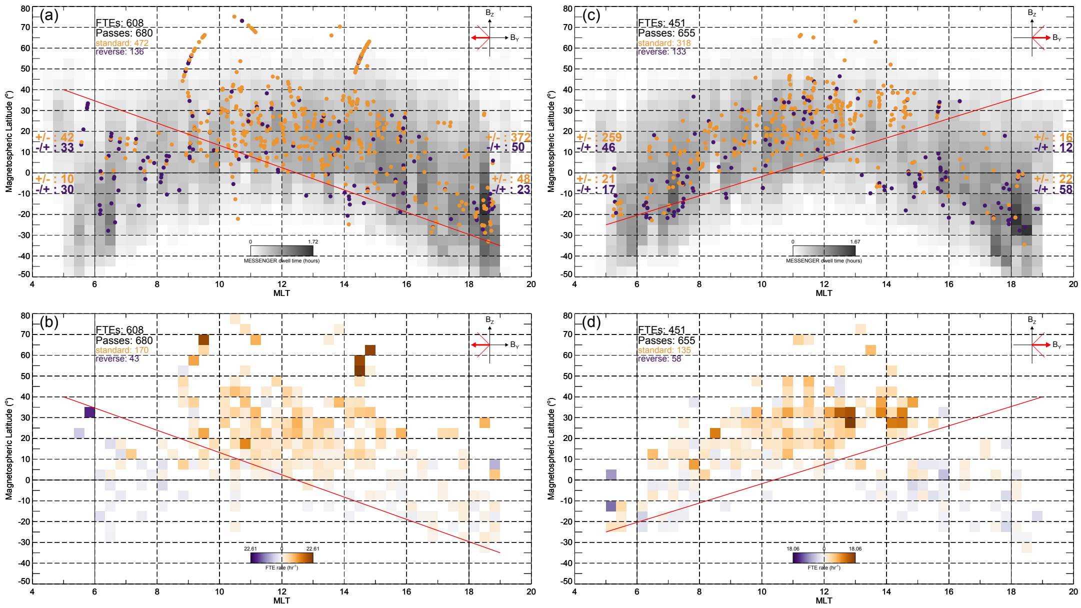

Figure 5.6: The location and direction of motion of FTEs, separated into those events seen during different IMF orientations. (a-b) follow the same format as Figure 5.4, but including only those FTEs observed on passes for which the IMF clock angle was within 45° of dawnward, as indicated by the arrow in the top right of each panel. Similarly, (c-d) show only those events and passes where the IMF in the magnetosheath was within 45° of duskward. The diagonal red line in panels (a) and (c) represents the tilted X-line, separating those events travelling predominantly northward from those predominantly travelling southward. These lines are shown again in (b) and (d) for reference. Every panel also highlights the number of standard and reverse polarity events in each of 4 differently-sized sectors, bounded by the tilted X-line and the magnetic equator.

factor of 3 higher, indicating that FTE formation is greatly enhanced when the IMF has a strong negative B_Z component.

The clearest change in the orientation of the reconnection X-line is expected for strongly dawnward or duskward magnetosheath IMF, producing a clockwise or anti-clockwise rotation respectively. The magnetopause coverage and FTE observation locations during intervals of IMF within 45° of each of these cardinal directions are shown in Figure 5.6, with the dawnward data shown in panels (a) and (b), and duskward in (c) and (d).

Whilst Figures 5.5a and 5.5c exhibit clear differences in the quantity and spatial distribution of FTEs between northward and southward IMF, the most notable distinction between the dawnward and duskward cases presented in Figures 5.6a and 5.6c is in the polarity of the signatures. As was the case for southward IMF, in both IMF orientations shown here, the majority of FTEs are observed in the northern hemisphere near local noon with standard polarity signatures, as indicated by the orange dots. Those events seen near the terminator, however, vary considerably not only between IMF orientations but also between opposite flanks of the magnetopause during the same B_Y prevalence.

Focusing initially on the FTEs identified during dawnward IMF, displayed in Figure 5.6a, standard polarity events are seen to be dominant across the dusk flank of the magnetosphere, even at MLT > 17, where the MESSENGER coverage was mainly south of the magnetic equator. This is contrary to the case seen previously for southward IMF, where standard and reverse events were observed approximately equally in this region. Even more striking is the distinct lack of standard polarity signatures observed at MLT < 9, meaning that southward-travelling reverse polarity FTEs dominate in this region. This is strongly supportive of a clockwise-tilted reconnection X-line, passing through northern dawn and southern dusk. The red line in Figure 5.6a indicates approximately where the separation between standard-dominated and reverse-dominated FTEs occurs. Also shown are the number of standard and reverse polarity events in each of four sectors, bounded by the magnetic equator and the X-line indicator. For example, the number of each polarity event observed in the small wedge between the magnetic equator and the indicative 'X-line' in the northern hemisphere is indicated by the numbers just north of the magnetic equator on the left of Figure 5.6a. Similarly, the numbers just below the equator on the left-hand side indicate the respective number of events seen in the larger region between the equator and the indicative X-line in the southern hemisphere. The top right sector, above the average X-line in the northern hemisphere, is dominated by northward events, as expected. However, these standard polarities make up a larger percentage of the total observations in the southern dusk sector, at 67%, than at northern dawn (56%), despite being below the equator where a non-tilted X-line would predict southward FTEs.

The indicative tilted X-line is also presented in Figure 5.6c for reference, where the net rate of FTEs is again shown, as calculated from Equation 5.1. Although exceptions appear with some reverse bins above and some standard below the 'average X-line', this is to be expected when combining data obtained from almost 700 passes. The overall trend is certainly in evidence, with the reverse dominance in the dawn sector particularly significant considering that reverse polarity events make up a little over one fifth of the total FTE observations, and reverse-dominated bins only a fifth of the spatial coverage. The peak net rate of southward-moving events of 18.36 hr^{-1} is higher than seen for any other IMF orientation, although this is a somewhat anomalous result given the small amount of time spent by MESSENGER in that location.

Figures 5.6c and 5.6d tell a very similar story for duskward-directed magnetosheath IMF, but with the main spatial features reflected about local noon. In this instance, a large number of northward FTEs are seen in the southern hemisphere dawn sector, but the dusk region is dominated by southward events. Once again, the preference for reverse polarity FTEs is made more significant by their relative scarcity in general, comprising less than 30% of the total events and being prevalent in the same percentage of the spatial bins for which at least 1 FTE was observed. The number of each polarity event is given for each of four sectors bounded in the same way by the X-line and the equator. For duskward IMF, the southern dawn sector has the same ratio of standard to reverse polarity FTEs as the northern dusk sector. Whilst not quite as stark a result as was seen for dawnward IMF, this still highlights how the average X-line cannot lie along the equator. Although some exceptions are again present, the overall trend is therefore strongly supportive of Mercury FTEs forming due to component reconnection at an X-line that is tilted anti-clockwise for duskward IMF, as has previously been shown at Earth.

5.4 Direction of motion of FTEs

Although the above method of utilising the sense of the bipolar signature in the normal component (Section 5.2.2) elucidates the influence of the IMF orientation on the location of northward- and southward-moving FTEs, and therefore the tilting of the average reconnection X-line, it gives no indication as to how the FTEs move along the curved magnetopause. In this section, the minimum variance analysis method is used to describe more precisely the motion of the observed FTEs.

As described in Section 5.2.1, only those events for which the helicity can be determined are included in this analysis. Immediately, this highlights one of the difficulties with using MVA on single-spacecraft data, as only 1899 events are left out of the original 2898. In previous work [e.g Imber *et al.*, 2014], the ratio between eigenvalues has been used to determine whether MVA axes are degenerate. A lower limit of 5 is therefore applied here to the ratio of intermediate to minimum variance eigenvalues, to ensure that the minimum variance axis has been accurately identified. An additional 283 events are removed from the dataset at this stage, leaving 1616 FTEs for which MVA can be utilised as an indication of motion. Using the assumed helicity as described in Section 5.2.1, the direction of travel is then determined to be either parallel or anti-parallel to the minimum variance axis, and the minimum variance direction reversed where required.

Figure 5.7 shows the location of the remaining FTEs projected onto the magnetopause plane, indicated by the circles. The solid coloured lines from each FTE indicate the orientation of the core field axis in this plane. This is calculated by fitting a Gaussian distribution the magnetic field components along both the intermediate and maximum variance directions, and taking the axis with the best fit to be the long axis of the flux rope. Similarly to the travel direction and minimum variance axis, the direction is reversed for those FTEs with a negative peak, such that the solid line indicates the direction of positive magnetic field along the core axis. If the FTEs in this plot were assumed to be force free, the intermediate variance direction would always indicate the core field axis. Because in some cases the field along the maximum variance axis best fits the expected distribution for the field in the core direction, there are therefore no assumptions made here as to whether the FTEs are force free.

However, there is much greater degeneracy between the intermediate and maximum variance directions than between intermediate and minimum variance directions, possibly making this core field orientation less reliable than the direction of travel. This is evidenced by only 128 of the 1616 FTEs meeting a similar criterion of the maximum to intermediate eigenvalue ratio exceeding 5. Despite the potential uncertainty of how accurately the core field has been identified by MVA, Figure 5.7 suggests that the majority of events are oriented with their long axis close to the

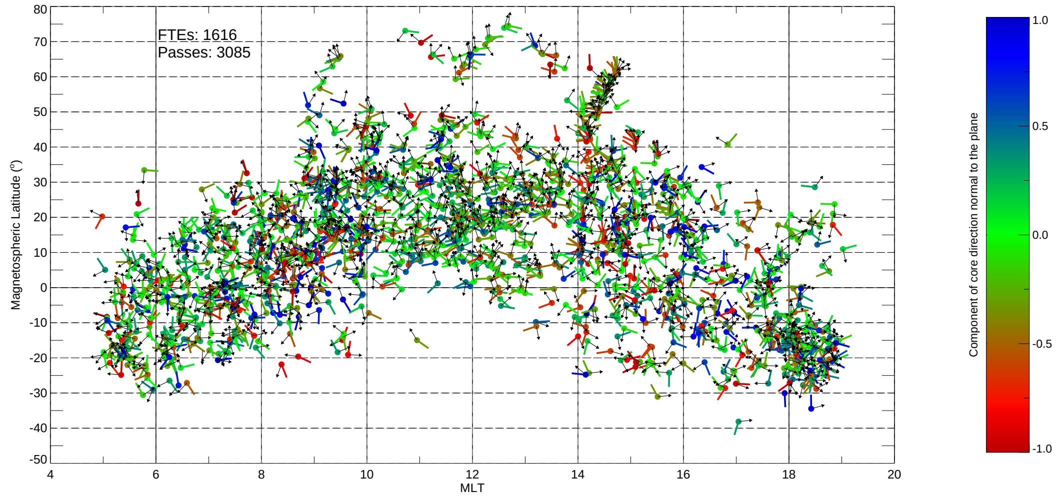

Figure 5.7: The orientation and direction of travel of each FTE as determined using minimum variance analysis. The coloured lines indicate the direction of the core field for each FTE (observation locations marked by the circles) in the magnetopause plane, and blue (red) colours indicate a large component out of (into) the plane of the figure. The minimum variance direction in this plane is marked with a black arrow for each FTE, corrected for assumed flux rope helicity where required, to provide the best estimate of a precise direction of travel.

plane of the magnetopause, as would be expected. The colour scale indicates the component of the axial field direction pointing into (red) or out of (blue) the plane of the magnetopause, computed by taking the dot product of the axis direction vector with the model magnetopause normal. For 1100 events, this dot product is less than 0.5, indicating an axial direction oriented less than 30° away from the magnetopause plane.

Although the long axis of the majority of FTEs lies close to the surface of the magnetopause, there is considerable variation in the orientations within that plane. The core field of each FTE would be expected to lie close to the orientation of the X-line at which it formed, and although this has been shown in Section 5.3 to tilt with an increased B_Y component in the IMF, this still does not explain some of the near-meridional orientations seen in Figure 5.7. Far from the formation site, however, as the IMF drapes over the magnetopause and exerts a different force at one end of the flux rope structure to that seen at the end connected to the planetary field, the FTE is likely to twist or rotate out of its original orientation, explaining some of the variation seen. It should also be remembered that the MVA axis describing the core field direction is less well-defined than the direction of travel, introducing some uncertainty.

Due to the large number of events for which a travel direction can be calculated, it is difficult to obtain a clear picture of the precise motion of the FTEs in Figure 5.7. For this reason, it is useful to calculate the average travel direction within small spatial bins in the magnetopause plane. To do this, the directional mean is calculated in $5° \times 5°$ bins, using the method of Mardia & Jupp [2000].

The direction of each event as determined by MVA is given by a unit vector in MSM′ coordinates, which is then projected into the magnetopause plane to give a latitudinal, d_{lat}, and longitudinal, d_{lon} component, and a directional clock angle of

$$\theta = \arctan\left(\frac{d_{lon}}{d_{lat}}\right). \tag{5.2}$$

Within each angular bin, the direction of each FTE is combined to give

$$\bar{S} = \frac{1}{n}\sum_{i=1}^{n}\sin\theta_i \tag{5.3}$$

$$\bar{C} = \frac{1}{n}\sum_{i=1}^{n}\cos\theta_i, \tag{5.4}$$

from which the mean travel direction vector can be calculated to have a length

$$\bar{D} = \sqrt{\bar{S}^2 + \bar{C}^2}, \tag{5.5}$$

and a clock angle

$$\bar{\theta} = \arctan\left(\bar{S}/\bar{C}\right). \tag{5.6}$$

The length of the direction vector therefore gives an indication of how closely aligned the individual events within that bin are, such that only a small difference between the clock angle of each event will yield a larger $\bar{D}$. The directions from each bin can be combined to produce a vector field describing the average motion of FTEs in the magnetopause plane. However, the magnitude of each vector depends solely on the agreement of the FTE travel directions within that bin, rather than the velocity of the FTE, as this could only be obtained from single-spacecraft data by modelling. As a result, if every FTE in a bin is travelling in the same direction, the magnitude of the ‘flow vector’ for that bin will have a value of 1. Conversely, a bin containing only two FTEs, travelling in opposite directions, will have a ‘flow vector’ of zero magnitude.

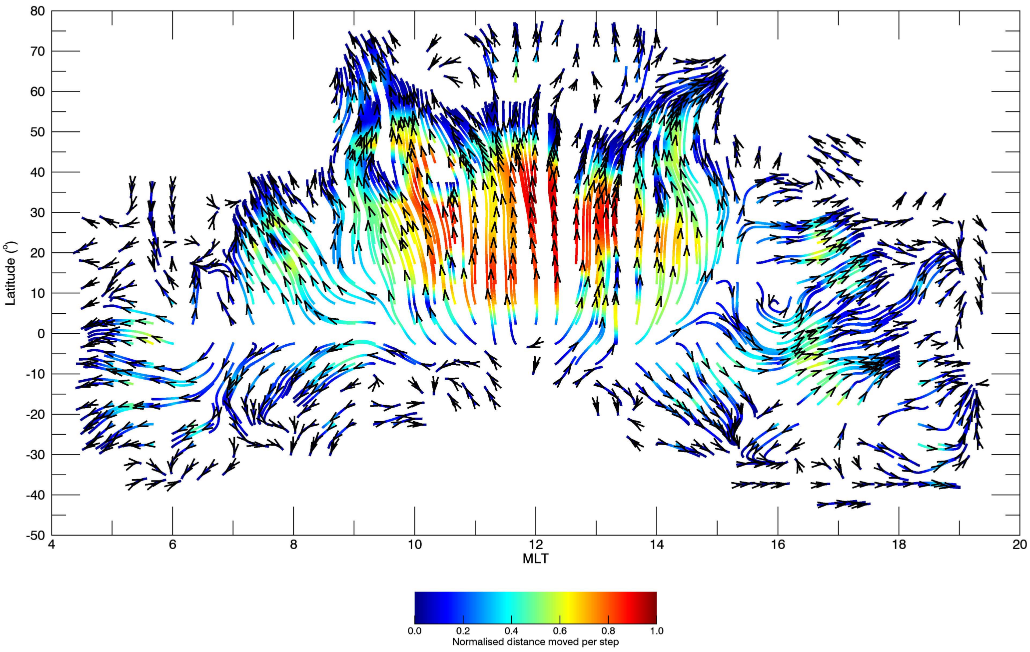

Figure 5.8: Flow diagram showing the average motion of FTEs in a projection onto the plane of the magnetopause. The colour scale indicates a normalised distance travelled by a particle at each step of the streamline, as described in the text.

Due to MESSENGER's orbital characteristics and the lack of FTE observations near certain regions of the magnetopause resulting in a large quantity of bins with no data, the calculated average directions have been passed through a 3-point bidirectional smoothing to provide better overall coverage of the magnetopause plane. To ensure that the resultant flow streamlines remain indicative of the data rather than the interpolated vectors, additional weighting has been given to the 'flow vectors' in bins containing FTE observations, increasing their magnitude by a factor of 5. At the centre of each spatial bin, particles are then injected, and their motion through the vector field tracked to produce the streamlines shown in Figure 5.8. These streamlines therefore indicate the average motion of FTEs in the plane of the model magnetopause.

The colour scale in Figure 5.8 denotes the normalised distance travelled by a particle in each step of the streamline generation. The largest distances naturally occur in regions of the vector field with the highest magnitude. As described above, these vector magnitudes are indicative not of the FTE velocities, but instead of how well the individual travel directions at each location are aligned with each other, as described by Equations 5.3-5.5. As such, the largest normalised distances, denoted by the red colouring, occur in regions where only small variations exist between the individual FTE travel directions. It is therefore unsurprising to see the best agreement in the low-latitude northern hemisphere near local noon, given that the vast majority of FTEs in this region were seen to be travelling northward in Figures 5.4 and 5.7. Physically, this implies that the FTEs formed near 12 h MLT are carried directly northwards and anti-sunward by the IMF, with any rotation of the long axis providing little contribution to the overall motion. Furthermore, within 1 h MLT of local noon, there is very little motion towards either flank at latitudes lower than 50°, at which point the tailward convection of the open field regions connected to the flux ropes begins to cut through MLT sectors around the side of the high-latitude magnetopause.

The effect of the draped IMF is much stronger and more evident further away from local noon. Beyond 16 h MLT, the FTEs on the dusk flank are seen to be travelling predominantly along lines of constant latitude, indicating IMF flow around the flank of the magnetosphere rather than over the poles. However, the positive or negative latitudinal components of motion provide some indication of the magnetic connectivity of the FTEs in this region, being linked to the northern and southern hemispheres respectively. A similar result is seen on the dawn flank, although the preference for predominantly tailward motion begins slightly further around the flank, beyond 7 h MLT.

Although the average motion depicted in Figure 5.8 may at first appear to disagree with the clear northward or southward motion implied by considering the sense of the B_N bipolar signature in Figures 5.4-5.6, this is not necessarily the case. As seen for the complete dataset in Figure 5.4, the total number of standard polarity events is similar to the number of reverse polarity FTEs near the dawn and dusk terminator, such that in calculating the average direction in each spatial bin the latitudinal components are likely to cancel out to a large extent, leaving only the tailward motion seen in Figure 5.8.

Due to the significantly reduced statistics when filtering the FTEs for IMF clock angle as was done in Section 5.3, the spatial coverage is too poor to accurately calculate the average flow direction of FTEs for strongly dawnward or duskward magnetosheath IMF. In these instances, there are too many bins for which the direction is computed entirely from smoothing rather than actual FTE observations, so additional observations are required before a proxy for the IMF convection can be compared for different IMF orientations.

5.5 Discussion

The main results of this chapter are now discussed not just in isolation, but in the context of previous similar work at both Earth and Mercury, as was done in Chapter 4. Although numerous authors have conducted investigations into the polarity of FTE bipolar signatures during different IMF clock angles at Earth, no such prior study exists at Mercury. As such, this chapter represents the first analysis of reconnection X-line orientation at Mercury using observations of flux transfer events, providing important context for the current understanding of the effect at Earth.

In MLT sectors close to local noon, Berchem & Russell [1984] observed predominantly standard polarity events, indicating a northward motion, in the northern hemisphere of Earth's magnetosphere, and southward-moving reverse polarity events almost exclusively in the southern hemisphere, a result repeated by Sibeck *et al.* [2005]. This indicates an average X-line location very close to, and parallel with, the magnetic equator. Korotova *et al.* [2012] performed a similar investigation to that presented in this chapter, analysing the distribution of standard and reverse polarity events at Earth during periods with a strong IMF bias towards either dawn or dusk. They observed a clear and strong rotation of the divide between the two polarities, indicating a rotation of the X-line during IMF with a large dawnward or duskward component, as shown in Figure 2.9. Fear *et al.* [2012b] also observed a similar effect during dawnward IMF, with standard FTEs seen near southern dusk and reverse FTEs near northern dawn. The results presented in this chapter therefore indicate that reconnection at Mercury exhibits a similar response to changes in the IMF clock angle as is seen at Earth, whereby component reconnection occurs along an X-line that tilts with respect to the magnetic equator.

Although other authors have previously used the polarity of FTE signatures to indicate their northward or southward motion, this chapter presents the first use of the minimum variance direction in describing a more precise direction of motion. As a result, there are no similar large-scale studies with which to compare the flow diagram shown in Figure 5.8. However, previous work has focused on modelling the motion of individual Earth FTEs at a range of locations on the magnetopause. Cooling *et al.* [2001] produced a model to describe the motion of reconnected magnetic flux tubes along the magnetopause. They showed that for IMF without a significant B_Y component, flux tubes near 12 MLT move almost directly northwards or southwards, depending on the hemisphere they are connected to, whereas those at greater longitude exhibit some initial azimuthal motion at low latitude before travelling over the poles. Such an effect is seen in the average flows calculated in this chapter, indicating that the overall motion when including all IMF orientations agrees well with the model predictions at Earth. Sibeck & Lin [2010, 2011] showed further, using the Cooling *et al.* [2001] model, that FTEs formed at a tilted X-line tend to propagate further around the flanks of the magnetopause, a feature also seen in Figure 5.8. The streamline diagram presented in this chapter therefore displays a new method for describing an average global flow using the motion of FTEs, and with additional data could be developed further to provide an alternative analysis of magnetic flux tube motions during a range of IMF conditions.

5.6 Summary

This chapter has presented a detailed analysis of the location and motion of flux transfer events near the dayside magnetopause of Mercury for four different orientations of the IMF in the magnetosheath. From the database of FTEs compiled in the previous chapter, the direction of motion for each event has been established using two different methods. Firstly, the sense of the bipolar signature seen in the magnetic field component normal to the magnetopause, B_N, is used to give an indication of either northward or southward motion, before a more precise direction of travel is calculated using minimum variance analysis of the magnetic field for each

FTE.

From the B_N component signature, the majority of FTEs observed by MESSENGER near the dayside magnetopause have been shown to travel northward, particularly in the northern hemisphere where MESSENGER provides the best spatial and temporal coverage, indicating a formation site at a reconnection X-line near the magnetic equator. However, when considering only those events observed during spacecraft passes on which the magnetosheath IMF was strongly biased towards either dawn or dusk, the average X-line is seen to tilt from the equatorial plane.

For dawnward IMF, a higher percentage of FTEs in the northern dawn sector are observed to travel southward than would be expected for an equatorial X-line, and the same is true of northward-moving events near southern dusk. This strongly suggests that FTEs are formed by component reconnection at an X-line that is on average tilted clockwise when the IMF clock angle is near -90°.

The opposite effect is seen for IMF clock angles close to 90°, where enhanced rates of northward FTEs are seen near southern dawn, and the northern dusk region contains a higher percentage of southward-moving events, suggesting that in this instance the X-line is tilted anti-clockwise.

Although the MVA technique has some difficulty reliably identifying the principal axes of the flux ropes in certain regions of the magnetosphere, for those events where the core field direction and helicity of the structure can be obtained, a precise direction of motion can be calculated. By averaging the directions of all events in small spatial bins, a flow diagram has been produced to map the motion of FTEs projected onto the plane of the magnetopause and give an indication of how open magnetic field convects into the magnetotail.

FTEs observed near 12 h MLT are seen to travel predominantly due north, suggesting that they are carried over the pole by the IMF, but further away from local noon an increasing longitudinal component is seen in the flow direction, particularly at high latitudes as the IMF drapes around the side of the magnetopause. Finally, near the equatorial terminator the average motion of FTEs is mainly tailward, with the northward or southward components of individual events effectively cancelling out. In low latitude regions, though, there is still an indicator of the magnetic hemisphere connectivity of the events, as FTEs connected to the northern hemisphere tend to travel northwards, and the opposite is true for southward-moving FTEs.

Chapter 6

Superposed Epoch Analysis of Flux Transfer Events

6.1 Introduction

The previous two chapters have focused on statistical observations of flux transfer events at Mercury to describe how their formation and subsequent motion is controlled by the orientation of the IMF. In this chapter, specific details of the signatures exhibited in magnetic field data by FTEs are examined through performing a superposed epoch analysis, and used to investigate the structure of the events identified in this thesis. The analysis has been performed with the data in both boundary normal (LMN) and minimum variance (MVA) coordinate systems, as defined in Chapter 1, with each providing different details on the structure of the FTEs.

In addition to utilising two coordinate systems, the superposed epoch analysis (SEA) has been performed using two methods of ordering the events. Firstly, the start and end times of the bipolar deflection evident in the MESSENGER magnetometer [Anderson *et al.*, 2007] data are recorded, and the duration of each event normalised between these points such that the magnetic field can be analysed as a function of the fractional duration of each FTE. The second method of ordering enables more direct comparison of the durations of observed FTEs, by identifying the point of largest magnetic field amplitude during each FTE, and setting this to the zero epoch.

In Section 6.2, the results are presented in the context of the entire dataset, providing an average picture of the magnetic structure of all FTEs identified in this thesis. Section 6.3 then divides the dataset based on location of FTE observation and properties of the IMF in the magnetosheath, to investigate how the magnetic structure varies with a range of parameters.

6.2 Overview of FTE magnetic field signatures

Throughout the analyses in this chapter, in addition to the two coordinate systems and two ordering methods outlined above, three different magnetic field scales are used to present the data. The first, and most simplistic, scale is to calculate the component of the magnetic field along each coordinate axis. In this system, however, the magnitude is likely to be dominated by the strength of the background magnetic field, particularly deep inside the magnetosphere, rather than reflecting the nature of the magnetic field contributions from the FTE itself.

In order to remove this effect from the results, the data are also presented as a magnitude change from the background level of that field component either side of the FTE. As indicated in Chapter 5, the start and end times of each FTE are identified on the basis of its bipolar signature, marking the start of the sharp rise in amplitude before the first peak, and the transition out of a sharp decrease in amplitude following the second peak. The magnetic field 10 s either side of these points is recorded, and the mean value of each component taken to be the baseline value for this difference calculation.

Accounting for the baseline level in the amplitude of each FTE as above does not completely reflect how significant a contribution the FTE represents relative to the total magnetic field strength at that location. For this reason, the amplitude change from the background level, ΔB, is divided by the magnitude of the background value, $|B_{bg}|$, to give the fractional change presented in the following results. A value of 1 on this scale therefore indicates that the field at that point is twice the background level in that component.

Chapter 5 discussed the direction of motion of FTEs, and the subsequent signatures produced in the magnetic field data as they passed over MESSENGER. In these analyses, standard and reverse polarity events are not considered separately, as the concern is primarily on the amplitude of the field variations in each component. Additionally, a large number of the signatures would cancel out when superposed, producing only a small amplitude bipolar feature that would not accurately reflect the nature of the vast majority of identified events. All reverse bipolar signatures, first decreasing before a positive second peak, therefore have their amplitude reversed such that the first peak of all bipolar signatures is positive. Similarly, the direction of the core field is strongly dependent on the polarity of the guide field during the formation process, and is again likely to cancel out if superposed in its raw form. For the following analyses, the core field is therefore also adjusted such that all core fields produce a positive enhancement.

Finally, Chapter 5 also discussed how the magnetic field signatures in minimum variance coordinates vary between FTEs. In particular, although the majority of bipolar signatures are found in the maximum variance direction, in 775 of the 2898 events the maximum variance axis most closely aligns instead with the core field. To ensure that the bipolar and core signatures can be investigated separately, without cross-contamination of the datasets, a further adjustment is made to swap the intermediate and maximum variance components in cases where the core field lies along the latter direction. In the following plots, the data are therefore given in B_{min}, B_{core} and $B_{bipolar}$ coordinates, rather than along the uncorrected minimum variance axes.

The analysis is first performed on the entire dataset of 2898 FTEs, to provide an overview of the signatures observed in all of the FTEs utilised in previous chapters, regardless of the location, orientation, or IMF conditions at the time. Figure 6.1 presents the results in boundary normal coordinates, when the duration of each FTE is normalised, and the events are ordered by the start and end times of the bipolar signature. From top to bottom, the rows show the L, M, and N components of the magnetic field, and from left to right the columns indicate: the actual magnitude, B; ΔB, the change from the background; and the fractional change from the baseline. In all panels, the upper and lower quartiles are marked by the shaded region, and the median value is denoted by the solid black line. The mean value at each timestep is

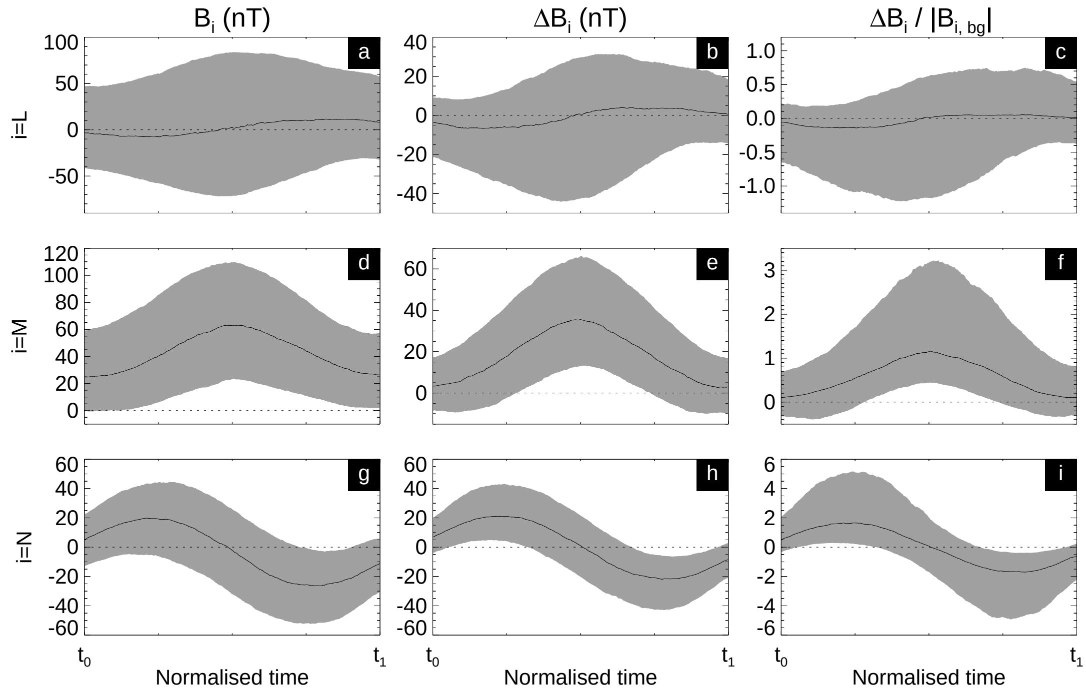

Figure 6.1: Results of superposed epoch analysis, with the data ordered by the start and end times of the bipolar signature, shown in boundary normal coordinates. The rows show the data in each of L/M/N coordinates, from top to bottom. From left to right, the columns indicate: the magnetic field in each component; the change from the background value of that component; and the fractional change from the background level. The solid line denotes the median value at each normalised timestep, whilst the shading indicates the upper and lower quartile values.

not too dissimilar from the median value of the field in both absolute magnitude and difference from the background, however it is weighted heavily towards the FTEs with very low background field components for the fractional increase measurements. This produces signatures unrepresentative of the whole dataset, so for consistency the median value is used across all measurements.

In Figure 6.1a, the median component along the B_L direction shows a small amplitude bipolar signature, suggesting a component of motion along the direction normal to the magnetopause. However, the wide range of values in the shaded region shows that there is considerable variation between individual FTEs, with a large number of measurements cancelling out to leave only the small residual bipolar signature present in the median values. The greatest spread of amplitudes occurs near the centre of the window, producing both a positive and negative unipolar peak. This indicates that the component of the core field along the L direction has a larger amplitude than the B_L component of the flux rope's helical field. The implication of this is that the local azimuth, the θ component in cylindrical coordinates, is inclined with respect to the L direction. When accounting for the background field, the shape of the median curve changes very little, however the upper quartile becomes less unipolar. This is particularly true in 6.1c, showing the fractional change, and is attributed to the large positive B_L component of the planetary field representing a significant contribution to the positive peak in Figure 6.1a. The negative unipolar peak persists in Figures 6.1(b-c), though, implying that the FTEs are the source of this feature in Figure 6.1a. This indicates that a large portion of the FTEs are oriented such that their core field has a significant $-B_L$ component.

The average direction of the long axis is closely aligned with the M direction, though, as can be seen from the unipolar shape of the median B_M component. Furthermore, the larger amplitude difference between the median and upper quartile (UQ) than the median and lower quartile (LQ) in Figure 6.1e indicates that there are more extremely large core fields than there are extremely small core fields. This is likely due to a selection bias introduced by visual identification of FTEs, whereby the largest core fields are naturally identified more easily than small amplitude core fields. This becomes even clearer in Figure 6.1f, which also suggests that many of the largest amplitude core fields occur in regions where the background B_M is very low. This would be the case near the magnetic equator, implying that FTEs formed at low-latitude reconnection X-lines lie with their long axis initially primarily along the magnetic equator, before tilting out of this orientation as they move away into regions where the background field also has a larger B_M component. This will be discussed further in Section 6.3.2.

Finally, Figures 6.1(g-i) show that the magnetic field normal to the magnetopause exhibits a very clear bipolar signature that is extremely symmetric. Not only does the median value cross through 0 very close to the mid-point of the normalised time interval, but the amplitude of the two peaks is also identical, at 20 nT from the baseline level (panel h). This suggests a highly cylindrical structure for the observed FTEs, and a direction of motion mostly within the plane of the magnetopause, as a component of travel normal to the magnetopause would be likely to introduce asymmetries in the peak amplitudes. The small difference observed between (g) and

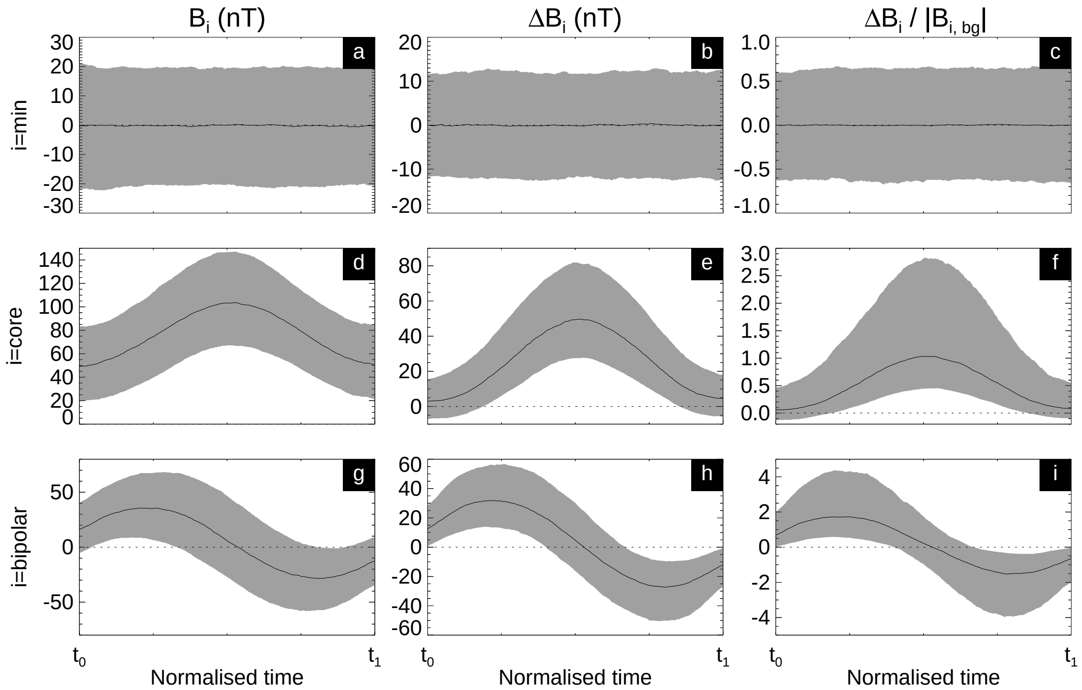

Figure 6.2: Results of superposed epoch analysis, with the data ordered by the start and end times of the bipolar signature, shown in adjusted minimum variance coordinates. The format follows that of Figure 6.1, but with the rows now indicating the components in the directions of minimum variance, core field and bipolar signature, from top to bottom.

(h) also reflects how the majority of FTEs are observed near the magnetopause, where the background $B_N \approx 0$. This is also evident in the fractional change results (Figure 6.1i). For the first peak, there is a larger variation from median to upper quartile than there is from median to lower quartile, and the opposite is true for the negative peak.

Figure 6.2 presents a similar analysis, but with the magnetic field data now converted to the adapted minimum variance coordinates described above, where the core field and bipolar directions have been isolated from the intermediate and maximum variance axes. From top to bottom, the rows show the magnetic field components along the directions of minimum variance, core field and bipolar signature, whilst the columns have the same format as in Figure 6.1. Figures 6.2(a-c) indicate that the minimum variance direction is extremely well-defined across the dataset of FTEs, with a median value of 0 and only a small variation within the upper and lower quartile range.

Although the core field signature in Figures 6.2(d-f) looks very similar to that in boundary normal coordinates, there are some subtle differences that provide information as to the orientation of the observed FTEs. In minimum variance coordinates, the median core amplitude above the background level is 50 nT, with upper and lower quartile values of 80 nT and 25 nT respectively. Comparatively, the median increase above the mean background field in B_M, as shown in Figure 6.1e, is 35 nT, with upper and lower quartiles of 65 nT and 25 nT. As minimum variance analysis provides the most accurate method of determining the core field direction, the values indicated in Figure 6.2 best represent the average increase in magnetic field strength due to the core field of each FTE. The peak values seen in B_M to be 15 nT lower than those in B_{core} therefore provide further evidence of an average tilting of the flux ropes' long axis away from the M direction, as had already been inferred from the presence of a negative peak in B_L in Figures 6.1(a-c).

An additional difference between the magnetic field features observed in the two coordinate systems is that of the symmetry in the bipolar signature. Whereas the B_N component is seen to be symmetric both in time and in magnitude of the peaks, the same is not true in minimum variance coordinates. Although the $\Delta B = 0$ point occurs very close to halfway through the interval in Figure 6.2h, the magnitude of the first peak is $\sim 13-17\%$ greater than that of the second, in both the median trace and the largest amplitude quartile. The amplitude of the first peak in the median is 31.87 nT, dropping to 27.30 nT at the second peak, whilst the upper quartile has a maximum of 56.89 nT during the first peak and the amplitude of the lower quartile during the second peak is only 50.46 nT. Fear *et al.* [2010] similarly observed a peak-to-peak amplitude difference in analysis of FTEs observed by Cluster at Earth, and attributed it to a compression of the magnetic flux at the leading edge of the FTE, and a rarefaction on the trailing side. However, they saw this asymmetry in the B_N component, whereas the FTEs shown in Figure 6.1 have symmetric peaks.

The lack of asymmetry seen here in B_N is likely due to the intermediate and maximum variance directions not being particularly well-defined for the majority of FTEs examined here, as discussed in Chapter 5. A poorly-defined 'core' axis will not be perfectly aligned with the core field of the FTE, and conversely the axis containing the bipolar signature may have a component along the long axis of

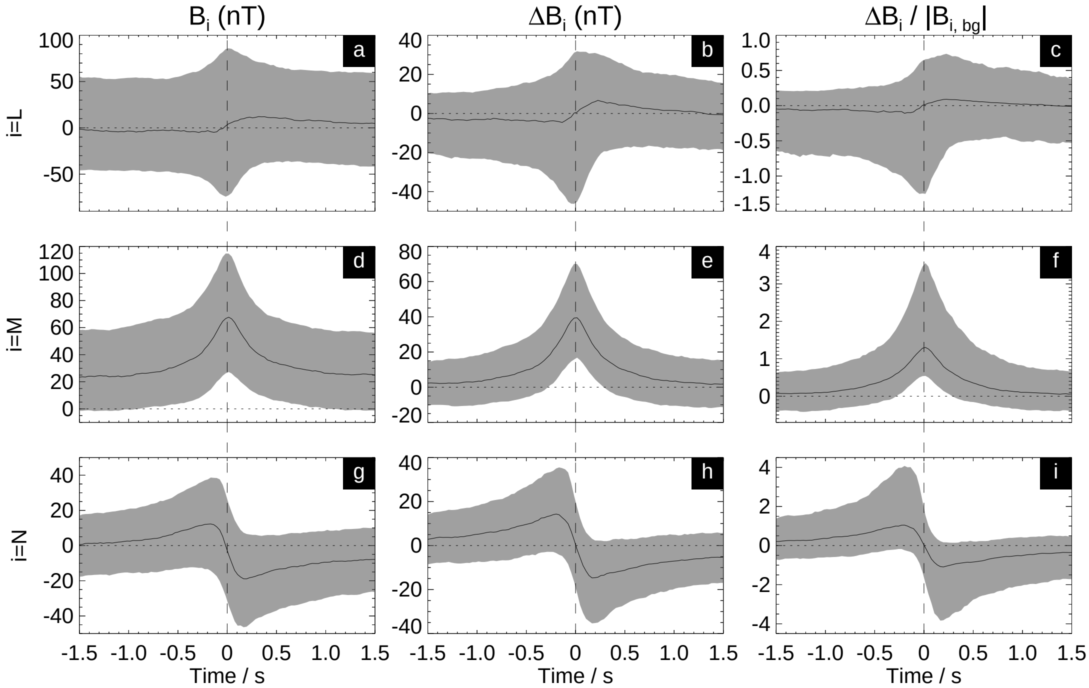

Figure 6.3: Results of superposed epoch analysis, with the data ordered by the time of the largest field amplitude, shown in boundary normal coordinates. The panel format follows that of Figure 6.1.

the flux rope. For a cylindrical force-free FTE, the core magnetic field should be entirely along the z-axis in cylindrical coordinates, and the helical field at increasing distance from the centre of the flux rope tends towards the local azimuth, or θ direction. However, for many FTEs it may not become entirely azimuthal at the outer extent, either due to retaining a component along the core field direction or the FTE having a non-circular cross-section. As a result, the field along a 'bipolar' MVA axis with a small component parallel to the core field will produce peaks with asymmetric amplitudes, as is the case in Figures 6.2(h-i).

Figures 6.3 and 6.4 follow the same format as Figures 6.1 and 6.2 respectively, but with the FTEs now ordered by the time of peak field amplitude rather than the bipolar signature. Many of the features seen in the bipolar-ordered data are also present in a very similar form within the central $1-2$ s of the core-ordered data, indicating that across the database the FTEs exhibit a very strong temporal symmetry. Furthermore, the amplitude of the core field in both coordinate systems agrees very well with that seen when the events are ordered by the bipolar field, suggesting that the temporal symmetry is not merely an averaging effect, but a

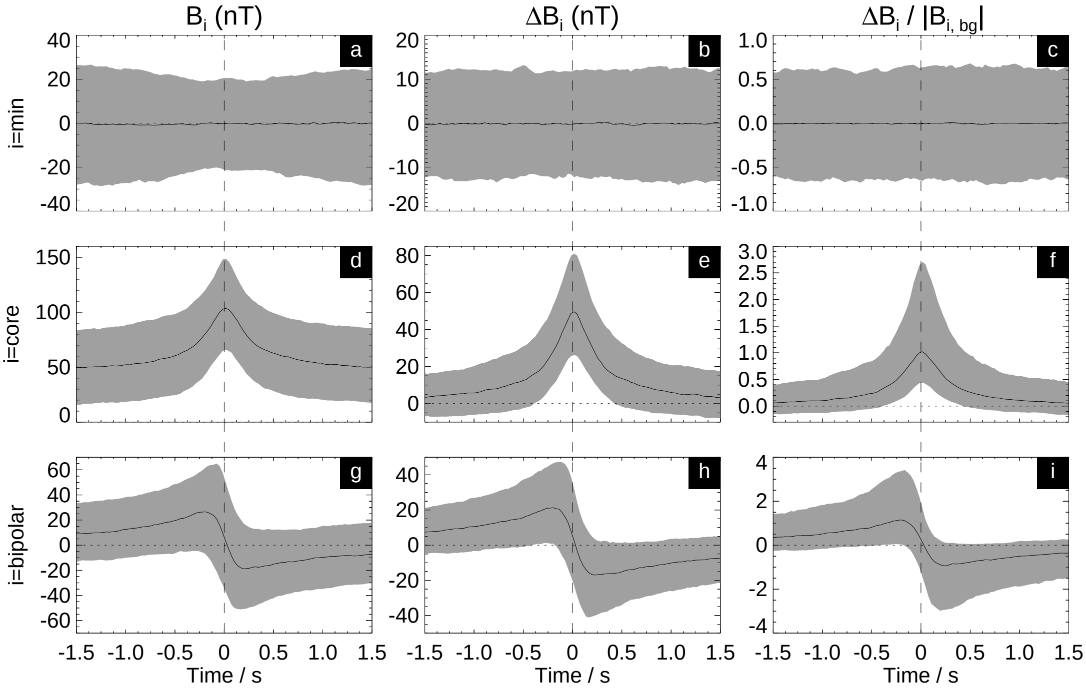

Figure 6.4: Results of superposed epoch analysis, with the data ordered by the time of the largest field amplitude, shown in adjusted minimum variance coordinates. The panel format follows that of Figure 6.2.

genuine feature in the individual FTEs.

It is in the bipolar signature that the main differences between the two ordering systems exist. Although the amplitudes of both B_N peaks are symmetric, and again larger in the first peak than the second when converted to minimum variance coordinates, the actual amplitudes of the median and quartile values are considerably lower when the data are ordered by the time of the peak field. This arises due to a considerable range of FTE durations producing a wide spread in peak times in the 'real' temporal scale used in Figures 6.3-6.4 that is removed by normalisation of the bipolar-ordered time series.

Similarly, the spread in durations produces much wider peaks in the core-ordered analyses, with shallower gradients immediately outside the peaks in field along the maximum ('bipolar') MVA axis than are seen in the bipolar-ordered time series. Beyond 0.5 s either side of the zero epoch, both Figures 6.3h and 6.4h show sustained non-zero field, with a ~ 25 nT spread between upper and lower quartiles, even out to 1.5 s either side of $t = 0$. This indicates the presence of a pile-up of magnetic flux outside the main flux rope, in the form of the travelling compression regions first identified at Mercury by Slavin *et al.* [2009a].

The results presented in both coordinate systems and with both methods of ordering the data clearly show the strong magnetic fields present inside FTEs at Mercury, highlighting the large contribution they make to the Dungey Cycle as shown previously by Imber *et al.* [2014]. In minimum variance coordinates, the median bipolar field of the FTEs contained in this study peaks at $\sim$ 30 nT (Figure 6.2h), and the median core field is $\sim$ 50 nT (Figure 6.4e), whilst the upper quartiles indicate that 25% of the identified events have components exceeding both of these values by at least 30 nT. This equates to a median increase of 100% above the background level of each component. For both the bipolar and core fields, the difference from median value to the largest amplitude quartile is considerably greater than that between median and lowest amplitude quartile. Although a selection bias ensures that not many events containing magnetic fields substantially weaker than the median values can be observed, a significant number of events will greatly exceed the flux content of the average FTE presented here.

6.3 Investigating variations in FTE signatures

Whilst the previous section provides a picture of the average FTE structure across almost 3000 events, it gives no indication of how the structure changes with a number of parameters. In this section, the dataset is broken down to provide analysis on how the FTE signatures vary with the strength of the IMF in the magnetosheath relative to the magnetospheric field strength. The direction of the core field is also investigated for opposite polarity magnetosheath IMF $B_{Y'}$, before the duration and magnetic field strength of each event is analysed at a range of distances either side of the magnetopause.

6.3.1 Strength of the magnetosheath field

In order to investigate whether there are differences between FTEs produced during symmetric and asymmetric reconnection (discussed in Chapter 2.1.2), the ratio of B_{MSp}/B_{MSh} is calculated for each pass through the magnetopause (where a 1-minute mean of the field magnitude just outside the crossing is given by B_{MSh} and that just inside is given as B_{MSp}), and the dataset divided into three groups: those where the magnetosheath field is dominant, ($B_{MSp}/B_{MSh} < 1$); when the planetary field is significantly larger ($B_{MSp}/B_{MSh} > 1.5$); and the more symmetric case containing all events where the ratio lay between these two values. The limits were chosen to provide the best coverage of magnetosheath dominant, symmetric, and magnetosphere dominant regimes whilst retaining sufficient data coverage within each bin for a superposed epoch analysis to produce meaningful results. This is particularly crucial for the first case, as only 150 FTEs were observed on passes during which the magnetosheath field was stronger than that just inside the magnetopause. For each ratio bin, the median change from the background level was calculated in minimum variance coordinates, as indicated in Figure 6.5 along with the upper and lower quartiles. The data are ordered by the normalised duration of the bipolar signature to ensure no features are introduced by the range of FTE durations present throughout the dataset.

The figure follows a similar format to those in the previous section, where the rows show, from top to bottom, the components along the minimum variance, core field, and bipolar signature directions. The columns separate the data by field strength ratio, where the relative strength of the magnetosheath field decreases from left to right. The number of FTEs observed in each range is indicated in panels (g-i), showing that the majority of events were observed when the magnetospheric field was dominant. However, this is more a reflection of the number of passes on which MESSENGER observed each ratio rather than an indication of increased FTE observations for particularly weak magnetosheath fields. Indeed, the average of 0.99 FTEs per pass during magnetospheric-dominant field is lower than the 1.24 seen per pass during strong magnetosheath field.

Figures 6.5(a-c) show that in all cases, the minimum variance axis is, on average, very well defined, with the median trace showing only small departures from the background field along that direction. In both the core field and bipolar signature, the FTEs observed during intervals of near-equal and magnetosphere-dominated fields exhibit very similar features. The median core field is 50 nT above the back-

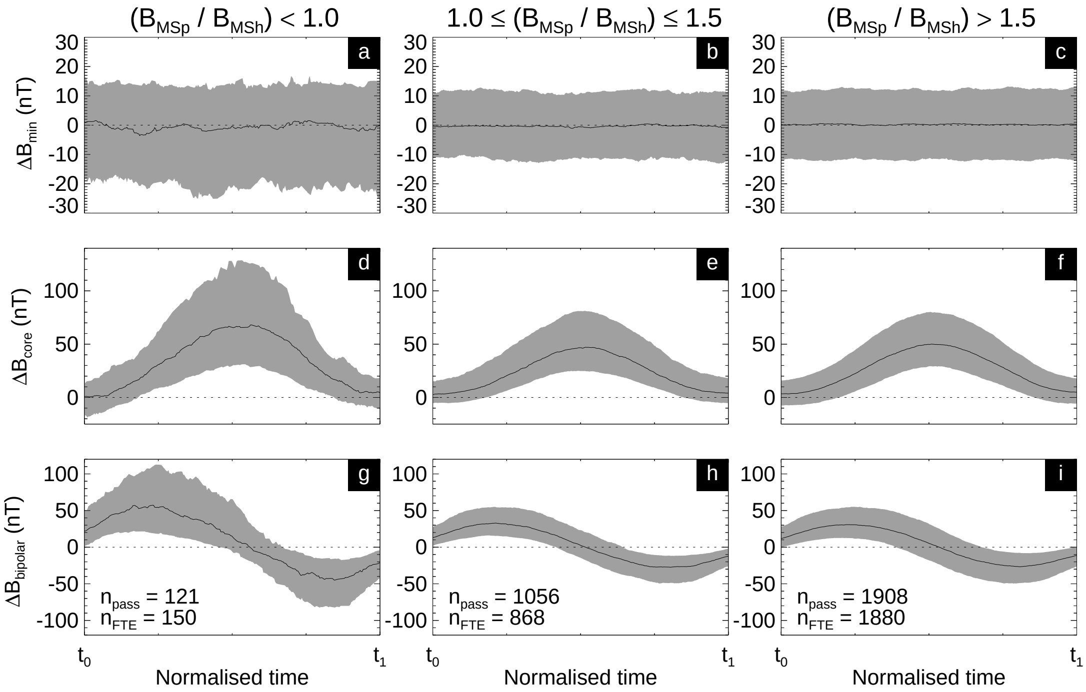

Figure 6.5: Comparison of superposed epoch analysis results for a range of magnetic field strength ratios either side of the magnetopause. The data are ordered by the start and end times of the bipolar deflection, and are presented in minimum variance coordinates. From top to bottom, the rows indicate the change of the magnetic field from the background level in the minimum variance, core field and bipolar directions. The leftmost column contains FTE data during passes when the strength of the magnetosheath field was greater than that just inside the magnetopause. The rightmost column contains FTE data when the magnetospheric field was considerably stronger than the magnetosheath field, with a ratio greater than 1.5, and the middle column contains the remaining FTEs. The number of FTEs (n_{FTE}) and passes (n_{pass}) in each column is indicated in panels (g-i).

ground field along that direction, with an upper quartile of 80 nT. Similarly, the bipolar signature in both cases is slightly asymmetric, with a median amplitude of 30 nT for the first peak and 25 nT for the second, whilst the highest amplitude quartile is an additional 25 nT higher for both peaks.

However, the events observed during passes on which the IMF in the magnetosheath was stronger than the planetary field just inside the magnetopause show a very different picture. The central 50% of the distribution have core field amplitudes above the background level ranging from $30 - 140$ nT, with a median value of 70 nT, only slightly lower than the upper quartile value seen in the larger ratio bins. The same increased field strengths are also seen in the azimuthal field producing a bipolar signature, where the median trace has similar peak amplitudes to the upper quartile value of larger field strength ratio FTEs, and the largest amplitude quartile

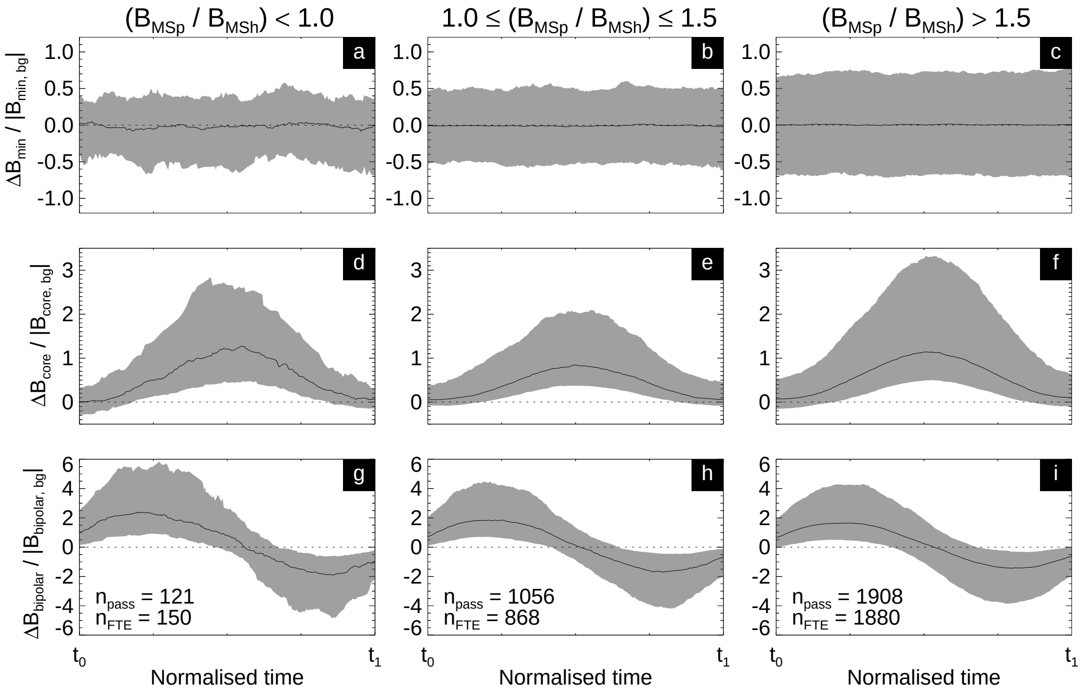

Figure 6.6: Comparison of superposed epoch analysis results for a range of magnetic field strength ratios either side of the magnetopause. The format is the same as in Figure 6.5, but the Y-axis here shows the fractional change from the background level in each component.

for magnetosheath-dominated events exceeds 110 nT at the first peak and 80 nT at the second. During reconnection with particularly strong magnetosheath field, a greater quantity of magnetic flux is opened and subsequently transported within FTEs than during reconnection where the planetary field is dominant. It should be noted, though, that the sample size of the magnetosheath-dominated FTEs is only one sixth that of the near-equal field strength events, meaning that a small number of extreme events will have a larger influence on the results.

In Figure 6.6, the same data are presented with the Y-axis accounting further for the level of background field along each axis by showing the fractional increase rather than the absolute value. The FTEs observed during strong magnetosheath field again exhibit stronger core fields and larger bipolar amplitudes than the near-equal field strength events. However, a more interesting comparison can be made between the near-equal strength FTEs, and events observed during strongly dominant magnetospheric field, particularly due to the large sample size contained within each bin. The bipolar peaks in panels (h-i) again appear similar, with median peaks at 1.75-2 times greater than the background, and upper quartile peaks a factor of 4 higher.

It is in the core field that the most notable difference exists between the two classes of events. Although the absolute difference from the baseline field along the direction of the flux rope long axis is the same, as seen in Figures 6.5(e-f), the fractional increase in Figures 6.6(e-f) is greater for FTEs observed during very dominant magnetospheric field than it is for FTEs produced by near-symmetric reconnection. The median core field in Figure 6.6f has a maximum increase of 1.14 times the baseline, compared to an increase of 0.85 for FTEs during near-symmetric reconnection. Considering the upper quartiles, these values rise to 3.33 and 2.10 respectively. The smaller number of extreme amplitude events seen in Figure 6.6e for more symmetric reconnection means that the background field along the core direction is stronger for these events.

There are two possible interpretations of these results. Firstly, for FTEs inside the magnetopause, the background planetary field is dominated by $B_{Z'}$. If the core field of the near-symmetric field events has a component in $B_{Z'}$, parallel to the planetary field, the same absolute increase would equate to a smaller fractional increase along the core direction than seen in Figure 6.6f for events oriented perpendicular to the Z-axis. 42% of the near-symmetric FTEs, and 27% of those seen during weak magnetosheath fields, were observed inside the magnetopause, so whilst such a tilting is not an insignificant contribution to the features seen in Figures 6.5 and 6.6(e-f), it is perhaps not the sole reason for the differences. For symmetric magnetic fields, pressure balance across the magnetopause (Equation 1.36) dictates that the plasma pressure is similar on both sides of the boundary. As a result of the small difference in β (Chapter 1.3.4), reconnection can occur across a wide range of magnetic shear angles, and therefore magnetosheath clock angles [e.g Phan *et al.*, 2013; DiBraccio *et al.*, 2013]. Consequently, the events produced by symmetric reconnection are more likely to be observed in background magnetosheath fields with a large $B_{Y'}$ component, close to the direction of the FTE core field. The different features seen between the central and right-hand columns of Figures 6.5 and 6.6 are therefore due to the symmetric events being generated at X-lines that form during a wide range of magnetosheath clock angles, and can exist at greater angles from the equatorial plane.

6.3.2 Y-component of the magnetosheath field

Following on from the analysis of core field orientations, in this section the relationship between IMF $B_{Y'}$ and the direction of the FTE long axis is explored. The full dataset is therefore separated into FTEs observed on passes where the magnetosheath $B_{Y'}$ was either positive or negative over a 1-minute mean just outside the magnetopause traversal, before performing superposed epoch analysis separately on the two groups. The results are shown in Figure 6.7 in boundary normal coordinates, where the Y-axis shows the difference from the background level in each component and the data are ordered by setting the zero epoch to the time of the peak in total

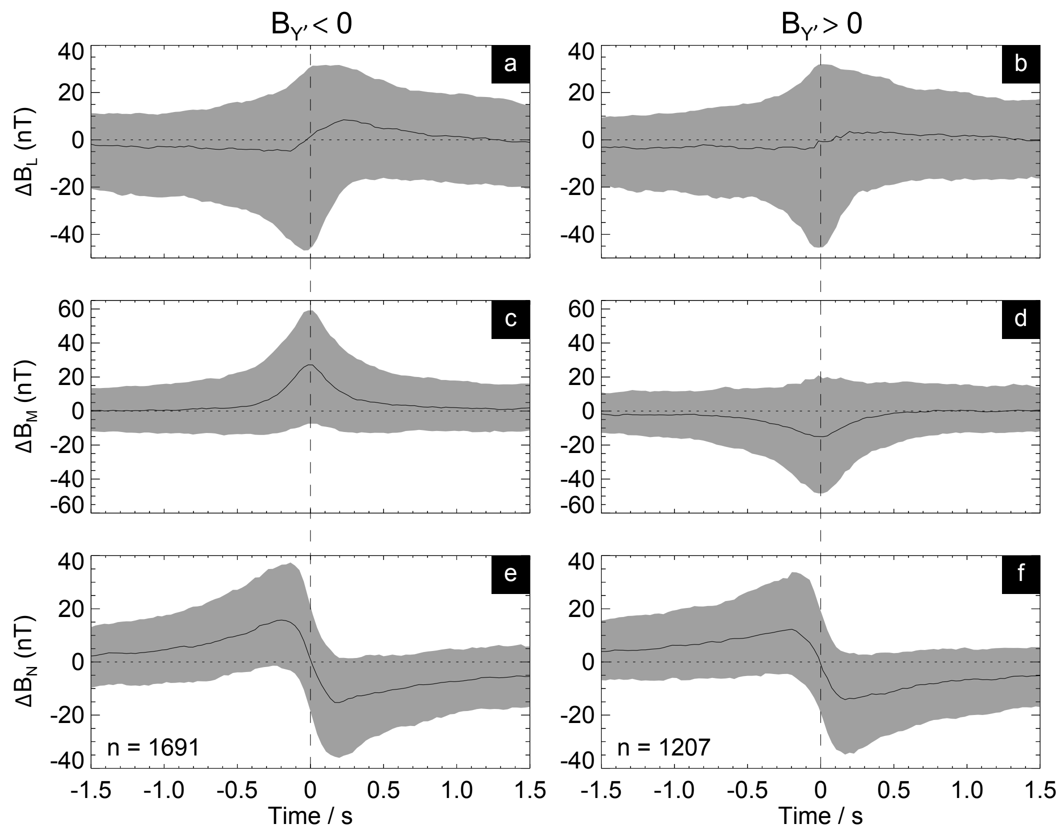

Figure 6.7: Comparison of superposed epoch analysis results for different magnetosheath $B_{Y'}$ polarities, where the data are ordered by the time of the peak in field amplitude. From top to bottom, the rows indicate the difference in the L, M and N components from the background level. The columns contain FTE data during intervals when the magnetosheath $B_{Y'}$ was negative (left), or positive (right). Also indicated in panels (e-f) are the number of FTEs observed during each orientation.

field amplitude. Unlike in the previous analyses, the direction of the core field is not reversed to always produce a positive peak, in order to determine whether it inherits the sign of the magnetosheath $B_{Y'}$. When located at the subsolar point, the M-axis points along $-Y'_{MSM}$, such that a core field inheriting a negative $B_{Y'}$ magnetosheath orientation will exhibit a positive peak in B_M, and the opposite is true when $B_{Y'} > 0$.

Figures 6.7(c-d) show that on average the FTE core directions follow the direction of the guide field present at the reconnection site due to the magnetosheath $B_{Y'}$ component, although the large spread between upper and lower quartiles suggests that a significant number of events are also oriented in the opposite direction. This is particularly true for $B_{Y'} > 0$, where the upper quartile shows a small positive peak, indicating that significantly more than 25% of FTEs have a component of their core field anti-parallel to the magnetosheath $B_{Y'}$ direction. Similarly, a little over 25% of FTEs seen during $B_{Y'} < 0$ also have a component of their core field anti-parallel to the magnetosheath $B_{Y'}$ direction, although the lower amplitude of the respective quartile peaks indicates that this effect is less common than for $B_{Y'} > 0$. For magnetosheath $B_{Y'} > 0$, the median and lower quartile values of 15 nT and 50 nT respectively are also lower than the corresponding peaks of 30 nT and 60 nT for FTEs on passes during which the magnetosheath $B_{Y'}$ was negative. This suggests that FTEs formed under conditions of $B_{Y'} < 0$ are more likely to have core fields that retain the sense of the guide field.

The B_L signatures shown in Figures 6.7(a-b) also exhibit subtle differences. Panel b, for $B_{Y'} > 0$, has a large, nearly symmetric, negative peak centred very close to the zero epoch in the lower quartile, and an upper quartile that appears to contain elements of both a unipolar core signature and a bipolar azimuthal field. This is indicative of the FTE core field making a large contribution to the B_L component. However, the negative peak in the $B_{Y'} < 0$ (panel a) lower quartile is more asymmetric around $t = 0$, producing a greater asymmetry in the overall signature between the quartiles than seen for positive $B_{Y'}$, suggesting that the largest contribution to B_L in these events comes from the helical field.

To investigate the difference between the two magnetosheath orientations, the

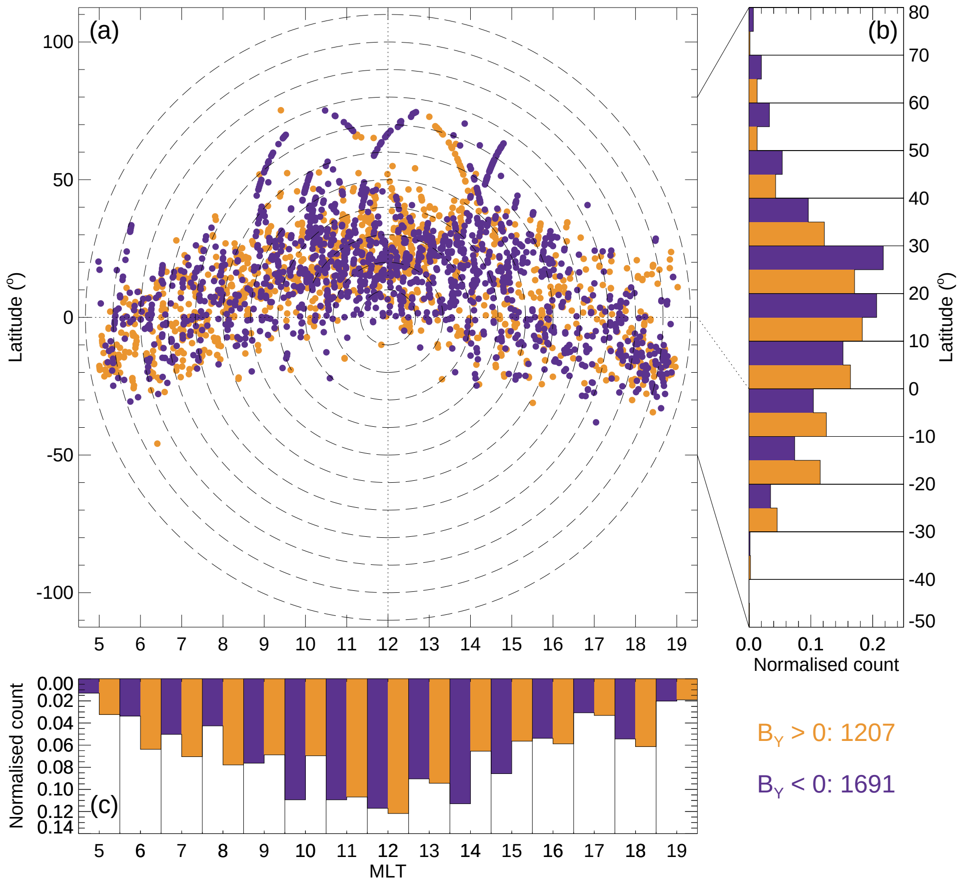

Figure 6.8: The spatial distribution of FTEs observed during passes when the magnetosheath $B_{Y'}$ component was positive (orange) or negative (purple). (a) The location of each FTE projected onto the MLT-latitude plane. The dashed circles denote intervals of 10° from the X'_{MSM} axis, for reference in Figure 6.9. (b) Histogram showing the relative occurrence of FTEs during each $B_{Y'}$ polarity in 10° latitude bins. (c) Histogram showing the relative occurrence of FTEs observed in 1 hour MLT bins.

locations of all FTEs have been plotted in magnetic latitude-MLT coordinates in Figure 6.8a, where the purple dots denote FTEs during negative magnetosheath $B_{Y'}$ and orange indicates the location of $B_{Y'} > 0$ FTEs. The number of events in each group within 10° latitude bins is indicated in Figure 6.8b, normalised for the total number of events observed during each IMF orientation, and Figure 6.8c shows a histogram of the MLT distribution of the events. Also marked on Figure 6.8a are circles indicating the limits of 10° wide bins from the X'_{MSM} axis, and the number of FTEs within each annulus is plotted on the histogram in Figure 6.9. The X-axis therefore represents the angle from the X'_{MSM} axis at which the FTE is observed, and the Y-axis shows the fractional occurrence of events during positive (negative) $B_{Y'}$, indicated in orange (purple).

As discussed in Chapter 4.4, the IMF bias [James *et al.*, 2017; Lockwood *et al.*, 2017] during the first year of MESSENGER's orbit provided more opportunities to observe FTEs during negative $B_{Y'}$ magnetosheath field. Accounting for the extra 484 events by calculating the fraction of FTEs seen in each MLT or latitude bin allows for a more direct comparison of how the distributions contribute to the signatures seen in Figure 6.7. During negative $B_{Y'}$, FTEs are seen predominantly between magnetic latitudes of $0-30°$, as shown in Figure 6.8b, whereas FTEs during positive $B_{Y'}$ are also seen extensively in the southern magnetic hemisphere. Similarly, the negative $B_{Y'}$ FTEs are seen primarily in the 9-15 h MLT range, whilst positive $B_{Y'}$ events are relatively more commonly observed further away from local noon, particularly on the dawn flank. This corresponds to increased observations of positive $B_{Y'}$ FTEs at angles greater than 70° from the X'_{MSM} axis, as shown in Figure 6.9. Conversely, during negative $B_{Y'}$, there are comparatively more events at small angles, especially between $10-40°$. The difference in magnetic field signatures between the two groups in Figure 6.7 can therefore be attributed to different spatial distributions.

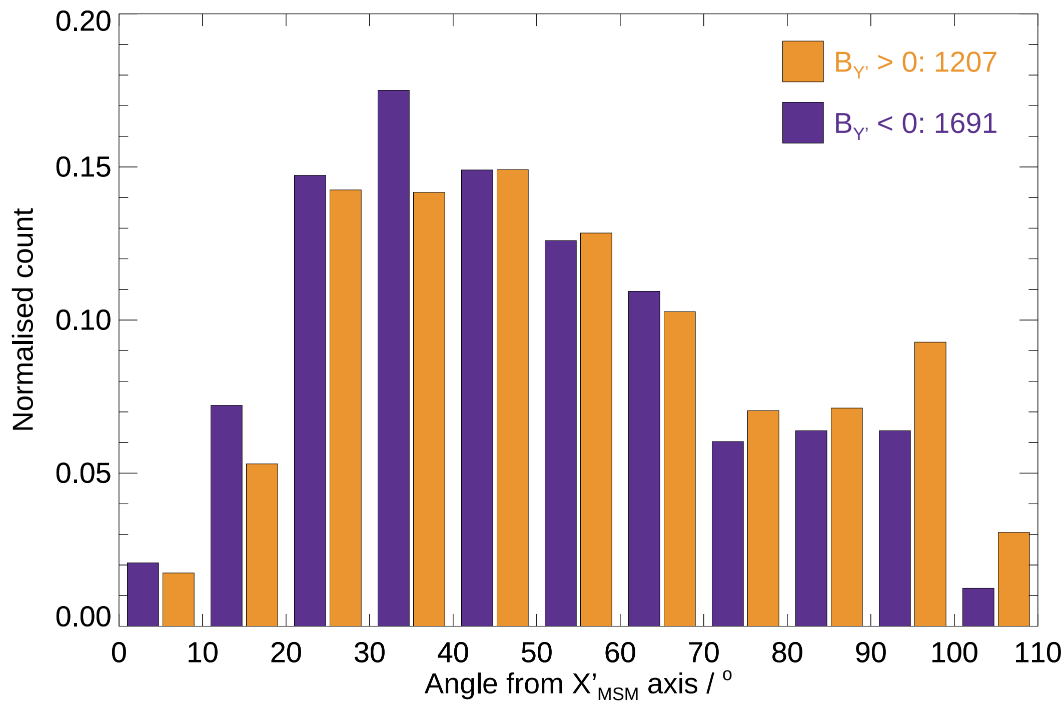

Figure 6.9: Histogram showing the relative occurrence of FTEs observed at a range of angles from the X'_{MSM} axis, counted in the 10°-wide bins indicated in Figure 6.8a. The count rate is given as a fraction of the total observations during each IMF orientation. FTEs observed on passes where magnetosheath $B_{Y'} < 0$ are counted in purple, whilst orange denotes those events on passes where $B_{Y'} > 0$.

With a greater percentage of the $B_{Y'} < 0$ FTEs observed near the subsolar point, both in latitude and MLT, the average signatures seen in Figure 6.7 are dominated by those events, whereas the $B_{Y'} > 0$ time series have a proportionally larger contribution from those events observed further towards the flanks of the magnetosphere or at higher southern latitudes. FTEs formed near the subsolar point are initially oriented with their long axis closely aligned to B_M, and the core field retaining the sense of the IMF $B_{Y'}$ component in the magnetosheath. However, as they convect to higher latitudes or around the flanks of the magnetosphere, they become more tilted, resulting in an increased component of the core field along B_L, as seen in Figure 6.7b.

6.3.3 Variations with distance from the magnetopause

In addition to moving away from the generally low-latitude reconnection sites along the magnetopause, producing the variation in signatures seen in the previous section, FTEs are also observed at a range of locations both inside and outside the magnetopause. In this section, the difference between events seen simply in either the magnetosheath or magnetosphere are examined, before an analysis of the variation across a discrete range of distances is performed.

Figure 6.10 shows the upper and lower quartiles, and the median value of the magnetic field along minimum variance axes relative to the background in each component, where the data are ordered by the time of the peak field amplitude. The dataset is split into those events observed outside the nearest magnetopause crossing, on the left; and those inside the magnetosphere on the right. Chapter 5 discussed how the minimum variance axis indicates the direction of motion, which for the majority of FTEs, particularly those seen within ~ 3 h of local noon, is predominantly either northward or southward. Panels (a-b) show that the minimum variance direction is, as with all previous analyses, very well defined on average, with a slightly smaller variation for those events inside the magnetosphere. This is due to the large component of the planetary field along $B_{Z'}$ inside the magnetopause, producing a high background field along the minimum variance direction for the FTEs shown in Figure 6.10a. In the magnetosheath, however, where the field is

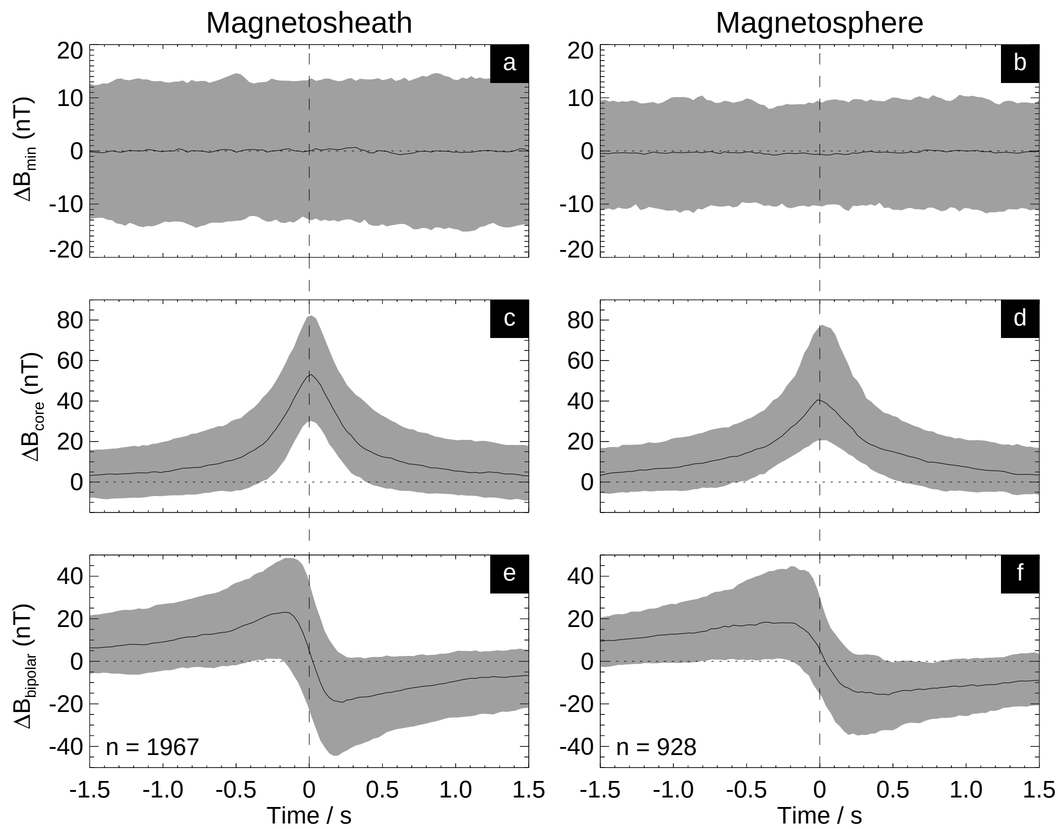

Figure 6.10: Comparison of superposed epoch analysis results for FTEs observed in either the magnetosheath or inside the magnetosphere, where the data are ordered by the peak in field amplitude. From top to bottom, the rows indicate the fractional change from the background level of the magnetic field along the minimum, intermediate, and maximum variance directions. The columns contain FTEs observed in the magnetosheath (left), or inside the magnetopause (right). Also indicated in panels (e-f) are the number of FTEs observed in each location.

generally of lower amplitude and more variable orientation, the background field along B_{min} will be smaller.

Figures 6.10(c-d) also reflect the lower magnetic field strengths generally measured in the magnetosheath, as FTEs forming at the magnetopause with the same core field strength and subsequently being observed in the magnetosheath have larger core amplitudes relative to their surroundings. The magnetosheath core field amplitudes also appear to have a very symmetric distribution, with a median of 55 nT, and upper and lower quartiles 25 nT either side of the median. Within the magnetosphere, however, the median amplitude relative to the background field along that direction is only 40 nT, with a lower quartile of only 20 nT. The upper quartile is only slightly lower than that seen in the magnetosheath, at 75 nT, indicating that there are proportionally more FTEs with extremely large core field amplitudes within the magnetosphere than in the magnetosheath.

Although the median peaks have a similar width in both the magnetosheath and magnetospheric FTEs, the wider peaks seen in the upper and lower quartile values inside the magnetopause suggest a larger range of durations for those events, an effect that is also seen in the bipolar signatures shown in Figures 6.10(e-f). The median and upper quartile amplitudes of both peaks are larger in the magnetosheath events, potentially due to a selection bias favouring identification of FTEs with stronger internal fields in a more turbulent background, and the sharper peaks again imply a smaller range of durations. In both locations, however, the first peak has a higher amplitude than the second. In Figure 6.10e, the median trace has a leading peak of 23.08 nT, and a trailing peak amplitude of 19.32 nT, and a similar amplitude decrease from 18.37 nT to 15.75 nT is present in the median trace of Figure 6.10f. This shows that compression of the leading edge due to magnetic flux pile-up occurs at all locations, regardless of the background magnetic field strength.

In order to further examine the variation in duration with distance, the locations were broken up into smaller distance bins from the magnetopause. In order to provide the best estimate of distance, even for events observed at a very different location from the magnetopause crossing on that pass, the distance was calculated from the FTE location to the nearest point on a magnetopause produced by scaling the subsolar point in the Winslow *et al.* [2013] model such that the boundary passes through the observed magnetopause crossing. Then, to account for the flaring at the flanks of the magnetopause, the separation between FTE and magnetopause was divided by the distance to the magnetopause at that location, giving the fractional distance, d:

$$d = \frac{R_{FTE} - R_{MP}}{R_{MP}}, \tag{6.1}$$

where R_{FTE} is the distance to the FTE from the centre of the MSM' coordinate system, and R_{MP} is the distance to the scaled model magnetopause.

The median duration of all FTEs within each distance bin is calculated based on the start and end times of the bipolar deflection, and plotted in the top panel of Figure 6.11 as the solid black line, where the upper and lower quartiles are indicated by the shaded grey region. The median orientation of the magnetic field at each timestep of a window spanning the bipolar signature is shown in the second panel in angular form, with normalised time increasing from $t_0 - t_1$. Considering only the magnetic field components along the core and bipolar axes, the difference from the background level is calculated, and the angle, θ, between the two components is given as

$$\theta = \tan^{-1}\left(\frac{\Delta B_{core}}{\Delta B_{bipol}}\right). \tag{6.2}$$

An angle of 90° (shown in green) therefore indicates that the local magnetic field within the FTE lies entirely along the core field direction, whilst a field pointing entirely along the local θ direction in cylindrical coordinates will have an angle of 0° (red) for the positive bipolar peak and 180° (blue) for the negative peak. The third panel of Figure 6.11 indicates the median total magnetic field amplitude for 3 seconds either side of the core-ordered zero epoch, relative to the background amplitude, and the bottom panel shows the number of FTEs observed at each fractional distance from the magnetopause.

Although the general trend is for the duration of FTEs to decrease from left to right, moving closer to Mercury, it should be noted that the largest magnetosheath distances have only a very small number of events. Discounting the leftmost 4 bins, as there are no more than 5 FTEs in each, the median duration still decreases from 2 s to 0.8 s, but with a $\sim$ 1.5 s range from lower to upper quartile in the majority of bins. The spread in durations for magnetospheric events seen in Figure 6.10 therefore seems to be predominantly due to those FTEs seen $0.1 - 0.2$ R_{MP} inside the magnetopause, where the peak in the upper quartile indicates a large number of events over 5 s in duration. Aside from the short duration events seen very deep inside the magnetosphere, the general trend appears to show that the duration of FTEs increases further away from the magnetopause. This could be due to rapid acceleration of FTEs away from their formation site as a result of magnetic tension causing them to travel past MESSENGER at a greater speed near the reconnection site than seen further away from the magnetopause, when they are being carried by the local flow. However, with only single spacecraft measurements and without modelling of the flux ropes, MESSENGER's path through the FTEs is unknown. A

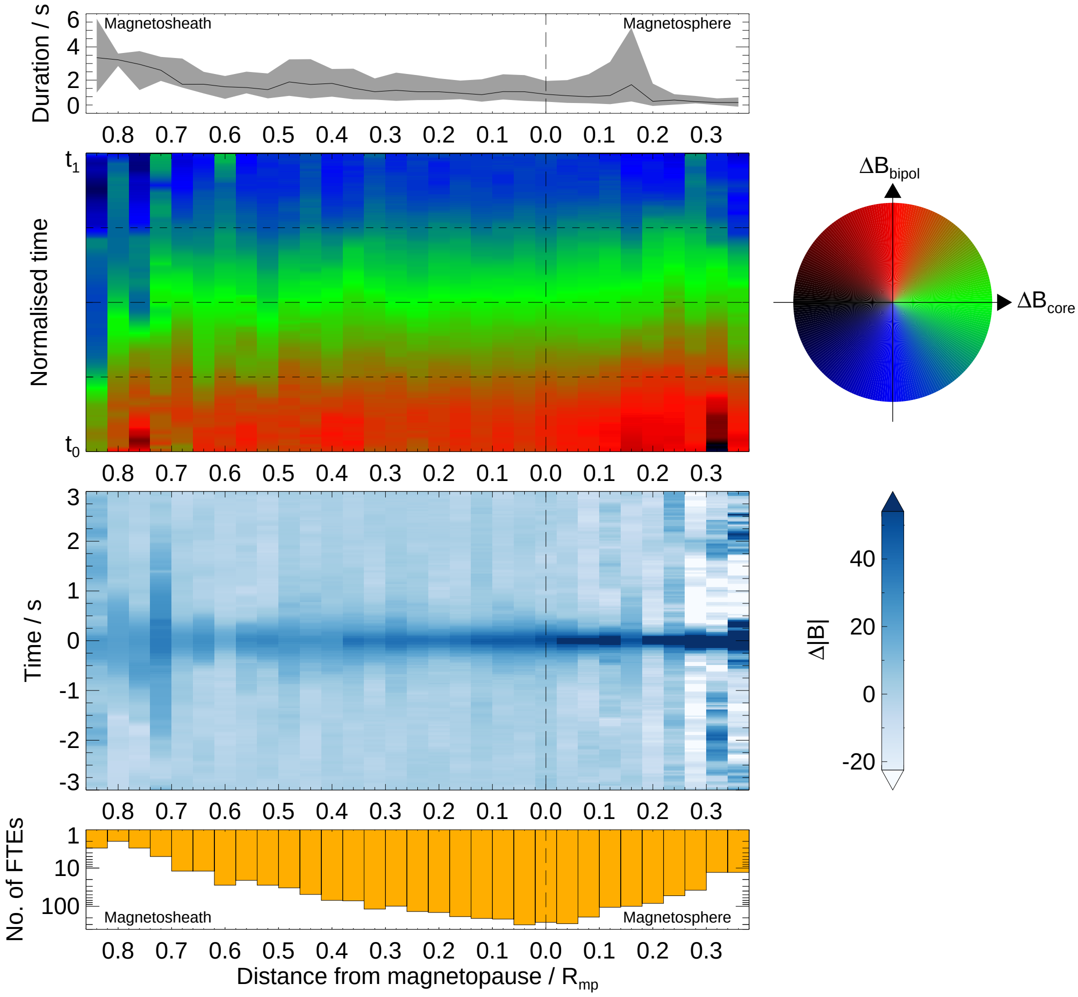

Figure 6.11: Variability in FTE signatures with location, measured as a fraction of the distance to the magnetopause as described in the text. From top to bottom: FTE durations, with the median denoted by the solid line and the upper and lower quartiles indicated by the grey shading; the angle of the magnetic field in the bipolar-core plane, as outlined in the text; the amplitude of the magnetic field within 3 s of the core-ordered zero epoch; the number of FTEs in each distance bin. Magnetic field values are given as the absolute difference from the background level of the relevant component.

low impact factor, passing close to the centre of the flux rope, will naturally produce a longer signal than an FTE encounter where MESSENGER only skims the edge of the flux rope. As a result, it is difficult to ascertain any details about the size of the observed FTEs at each location from these data.

The second panel shows that in most locations the magnetic field within the FTEs is closely aligned to the long axis for almost 50% of the event duration, before gradually becoming more tightly bound and reaching an entirely azimuthal field near the edges of the window. Excluding the low sample size bins at the greatest distances outside the magnetopause, the orientation of the magnetic field within each FTE is therefore shown to not vary significantly between magnetosheath events and magnetospheric events.

Considering the change in total field amplitude shown in the third panel, however, there are some differences with distance. Whilst the peak is, by definition, always at $t = 0$, the amplitude is greater for FTEs seen inside the magnetopause, increasing at larger fractional distances towards Mercury from the local magnetopause. The larger amplitudes inside the magnetopause are particularly interesting for those FTEs observed deepest into the magnetosphere, where the background planetary field is highest. Combined with the short durations seen deep inside the magnetosphere, the large relative core field strengths suggest that FTEs moving inwards towards regions of strong planetary field are compressed such that their radius decreases and, to ensure conservation of the magnetic flux within the structure, the field strength increases accordingly. The inward motion described here does not necessarily mean the FTEs are moving perpendicularly to the magnetopause plane, rather that they appear deeper inside the magnetopause at high latitude due to the cylindrically-symmetric magnetopause model used here not accounting for the cusp indentations. As a result, FTEs moving along the magnetopause towards the cusp will encounter stronger surrounding magnetic field strength, and be compressed whilst appearing to be located further from the model magnetopause used as a reference in Figure 6.11. However, without multi-spacecraft measurements, it is not possible to confirm the spatial scale of FTEs at various locations in the magnetosphere of Mercury.

6.4 Discussion

In this section, the results presented in this chapter are again compared to previous work investigating the properties of FTEs at both Earth and Mercury. However, no prior study has performed superposed epoch analysis on a large sample of FTEs at either planet. All comparisons are therefore made with case studies of spacecraft observations or simulations of individual events.

An example of this is in the orientation of the FTE long axis, where, at Earth, numerous authors have utilised multi-spacecraft measurements or modelling techniques to determine the angle of the long axis to the local M direction. Fear *et al.* [2012a] modelled FTE orientations and found that the events all exhibited an axis tilted slightly with respect to the local azimuth. This result was also observed by Trenchi *et al.* [2016], who saw even larger rotations, both from modelling and multi-spacecraft measurements. However, Kawano & Russell [2005] determined an axial orientation more closely aligned with the L direction using dual-spacecraft measurements. The results seen here for Mercury FTEs indicate a small rotation from an azimuthally-aligned core field, with the tilting increasing at greater distance from the subsolar point, in better agreement with the results of Fear *et al.* [2012a]. However, the analyses performed in this chapter do not allow for calculation of an exact angle to compare with previous work.

The superposed epoch analysis of FTE bipolar signatures in this chapter has revealed an asymmetry in the amplitude of the peaks. Whilst this has again not been investigated in the same way before at either Earth or Mercury, numerous MHD simulations have shown asymmetries in Earth FTE signatures. Ding *et al.* [1991] and Ku & Sibeck [1997, 2000] found that their simulations produced events where the trailing peak was of higher amplitude than the leading peak. However, from analysis of Cluster observations of FTEs, Fear *et al.* [2010] found the opposite result, where the leading peak tended to have a larger amplitude. They attributed this to compression of the leading edge of the FTE as it propagates through the magnetosphere, and rarefaction of the trailing edge. The dataset of Mercury FTEs analysed here shows the same trend seen by Fear *et al.* [2010], and supports their theory of FTE compression, with further evidence provided by the short duration of events observed deepest into the magnetosphere.

6.5 Summary

This chapter has presented an investigation of 2898 flux transfer events observed in the dayside magnetosphere of Mercury, using a superposed epoch analysis of their magnetic field signatures. By examining the data in both minimum variance and boundary normal coordinates, and ordering the data separately by both normalising to the start and end times of the bipolar signature, and in real time from the peak in total field amplitude, a number of features and trends have been identified.

Analysis of the entire dataset together shows that the long axis of the FTEs is, on average, tilted out of a plane parallel to the magnetic equator, and through dividing the dataset into events observed during either positive or negative IMF B_Y in the magnetosheath, the tilting is found to be greater for FTEs seen at larger distances along the magnetopause from the subsolar point. Axial tilting is also observed more clearly in FTEs formed by near-symmetric reconnection, when the field strength in the magnetosheath is similar to that just inside the magnetopause, indicative of reconnection occurring at a wider range of clock angles and therefore producing tilted X-lines.

In all analyses, the first peak in the bipolar signature is found to have a larger amplitude than the second peak, a result seen previously at Earth by Fear *et al.* [2010] and attributed to a pile-up of magnetic flux compressing the leading edge of the FTE. However, a large spread in the duration of the observed events produces a long, low gradient slope either side of the main FTE in the median and quartile values, making direct interpretation of the level of compression difficult.

Finally, investigation of the FTE signatures across a range of distances from the magnetopause, both in the magnetosheath and inside the magnetosphere, indicates that the events seen closest to Mercury have shorter durations, and larger core field amplitudes relative to the background field, than those seen close to the magnetopause or farther out in the magnetosheath. This is attributed to large compression of the flux ropes due to the high magnetic pressure of their surroundings, creating smaller radius flux ropes with stronger internal fields in order to conserve the magnetic flux content of each event as it moves close to the planet.

The magnetic field signatures of FTEs at Mercury bear a number of similarities to those seen at Earth, reflecting the similar underlying processes taking place to produce the structures. At both planets, the orientation of the IMF is a controlling factor in the orientation of the FTE long axis, however Mercury events have been shown to exhibit significant rotation from their initial orientation at large distances from the expected formation site. Although FTEs at Mercury occupy a considerably larger portion of the magnetosphere than do Earth events [Imber *et al.*, 2014], their actual size is much smaller. Indeed, the median duration of ~ 1 s seen here is even shorter than that observed by Imber *et al.* [2014], implying a similarly reduced spatial scale. Whilst the extent of the FTEs in MLT, along their long axis, cannot be determined without multiple spacecraft, the small magnetosphere at Mercury will likely limit the maximum azimuthal scale to be substantially shorter than that seen at Earth. As a result, Mercury FTEs are more easily rotated, highlighting that although the initial formation depends on the same factors at both Earth and Mercury, the subsequent evolution varies slightly between the two planets due to the different local conditions.

Chapter 7

Conclusions and Future Work

This thesis has presented a large-scale investigation into flux transfer events within the dayside magnetosphere of Mercury. This final chapter summarises the key results of the studies contained in the previous chapters and discusses their implications for the understanding of Mercury's magnetosphere and its interaction with the interplanetary magnetic field and solar wind. Finally, some remaining questions are discussed, along with ideas for future research to answer them.

7.1 Summary

In Chapter 4, magnetometer data from onboard the MESSENGER spacecraft were visually examined for signatures of magnetopause crossings and flux transfer events (FTEs) in the dayside magnetosphere of Mercury. The analysed data spanned 12 Mercury years, from orbital insertion on 18 March 2011 to 11 February 2014, ensuring even coverage of all magnetic local time (MLT) sectors. In total, across 3085 passes through the magnetopause, 12133 individual magnetopause crossings were identified, where the ~ 4 crossings per pass arose either through MESSENGER's orbital path causing it to skim the magnetopause at high latitude near the northern magnetospheric cusp, or as a result of ongoing reconnection eroding the magnetopause towards the planet and causing it to pass repeatedly past MESSENGER's location. Additionally, 2898 FTEs were identified on the basis of a clear bipolar signature in the magnetometer data, with an accompanying enhancement in the total magnetic field strength.

The interplanetary magnetic field (IMF) in the magnetosheath was measured just outside the outermost magnetopause crossing on each pass, and the rate of FTE observations investigated for variations with the IMF orientation. It was shown that for IMF clock angles close to 180°, where the negative B_Z component is dominant, at least one FTE was observed on $\sim$ 65% of passes, compared to only $\sim$ 15% of passes during near-northward oriented IMF (0° clock angle) yielding at least one FTE signature. Previous work by DiBraccio *et al.* [2013] had indicated that magnetic reconnection at Mercury occurs across a wide range of clock angles, but these observations show a clear preference for FTEs forming at reconnection sites between nearly anti-parallel magnetic fields.

The spatial distribution of the FTEs was also considered over the entire dataset examined, and shown to peak strongly near local-noon whilst significantly fewer events were identified on the dawn and dusk flanks of the magnetopause. This is to be expected for reconnection taking place mainly near the subsolar point at low magnetic latitude, but during the first 4 Mercury years of the mission the distribution showed far less variation, with a similar number of observations in all sectors between $9 - 15$ h MLT. This is due to both an interplanetary coronal mass ejection (ICME) encountering Mercury and generating 45 FTEs on a single pass in the post-noon sector, and the particularly strong bias in IMF orientation during this period, as was previously identified by James *et al.* [2017]; Lockwood *et al.* [2017], causing enhanced reconnection rates in the pre-noon sector.

Expanding on the investigation of spatial distribution of FTEs, Chapter 5 presents a study into the direction of motion of the event at each location, in order to estimate the formation sites and therefore the location at which reconnection takes place for four different IMF orientations. Two methods were employed, each with benefits and drawbacks. Although performing minimum variance analysis (MVA) on each FTE signature gives a precise axis along which the FTE travels, the direction of motion along that axis is only able to be determined for 1616 of the identified FTEs, a little over half the dataset. Analysing the signatures in boundary normal coordinates, however, enables identification of either northward or southward motion for 2474 events.

Using the boundary normal results, 75% of the FTEs are seen to be travelling northward, indicating a reconnection site south of the FTE location. Given the extensive coverage of Mercury's northern magnetic hemisphere, and only limited coverage of the southern hemisphere, particularly near local noon, this confirms that reconnection occurs predominantly near the magnetic equator. The results were then broken down into IMF orientations within 45° of the cardinal directions. Given the preference for FTE observation during southward IMF, shown in Chapter 4, it is unsurprising to find the southward IMF distribution comprises 50% of the total dataset, and the distribution of northward- and southward-moving events is very similar to that of the entire dataset. However, during northward IMF, FTEs are mostly seen on the flanks of the magnetosphere, where a large B_X component will produce a large magnetic shear angle across the magnetopause. Comparing the distributions of FTEs observed for both dawnward and duskward magnetosheath IMF reveals a clear tilting of the average reconnection X-line in the clockwise and anti-clockwise direction respectively.

Using the more precise directions of motion ascertained from MVA for a subset of these data allowed for construction of a flow map in the magnetopause plane. The FTEs observed at low northern latitudes near local noon are seen to travel almost entirely due northward, indicating that they are connected to magnetosheath field flowing directly tailward over the north pole. At higher latitudes, however, the FTEs are seen to gain a component of motion in MLT, indicating a slight deflection caused by the IMF draping around the sides of the polar region. Furthermore, at large distances in MLT from the subsolar point, FTEs are seen to move predominantly tailward on average, under the influence of the open magnetic field carried tailward by the solar wind flow around the sides of the magnetosphere.

Finally, Chapter 6 presented an investigation of variation in the properties of FTEs with both location and magnetosheath IMF properties, through a superposed epoch analysis of the magnetic field signatures. The key results include evidence for an increased inclination angle of the FTE long axis from a longitudinal alignment at greater distances from the subsolar point, both at high latitude and towards dawn or dusk. This tilting is also observed more strongly for FTEs observed when the magnetosheath field was of comparable strength to the planetary field just inside the magnetopause, suggesting that symmetric reconnection occurs across a wider range of magnetic shear angles, therefore producing more strongly tilted X-lines.

The bipolar signature is also found to be slightly asymmetric, such that the first peak has a larger amplitude than the second. This supports the findings of Fear *et al.* [2010] in a study of Earth FTEs, who suggested a pile-up of magnetic flux is produced at the leading edge of the FTE as it moves through a region of high magnetic field strength. The duration of the bipolar signature is also seen to reduce slightly as FTEs move closer to Mercury, with an accompanying increase in the strength of the axially-aligned core magnetic field, implying that as the FTEs travel further into the region of strong planetary magnetic field seen near the magnetospheric cusps, they are compressed spatially. In order to conserve the magnetic flux contained within the structure, a corresponding increase in the internal field strength of each FTE is seen.

More generally, the results of this thesis have enabled a number of comparisons to be made between flux transfer events at Mercury and Earth. At both planets, the orientation of the IMF plays a crucial role in not only the rate at which conditions enable formation of FTEs, but also the location of those formation sites. Additionally, the predominantly azimuthal orientation of the flux rope at low latitudes supports previous observations at Earth [e.g. Fear *et al.*, 2012a] that eliminated the Russell & Elphic [1978] ‘elbow’ model of FTE formation.

However, the nature of the events varies between the two planets, with FTEs at Mercury occupying a larger portion of the magnetosphere and containing much stronger magnetic fields, resulting in the significantly larger relative contribution to total magnetic flux transport seen previously by Imber *et al.* [2014]. Furthermore, due to the smaller spatial scale of FTEs at Mercury, and the stronger IMF in the inner solar system, magnetic tension forces at the azimuthal extent of the flux ropes cause FTEs to rotate out of their initial orientation as they move further away from the formation site.

Overall, the FTEs identified at Mercury are found to be governed by the same underlying physics as seen to control FTEs at Earth, but the different local conditions produce variations in the structure and evolution of events at the two planets, beyond a simple scaling to account for the size of the magnetosphere.

7.2 Future Work

The results presented in this thesis have provided new understanding of the nature of Mercury's magnetospheric interaction with the IMF, and the subsequent motion of magnetic flux tubes as part of the Dungey Cycle. Furthermore, previous observations of the tilting of reconnection X-lines at Earth have been replicated at another planet for the first time. However, a number of questions still remain, guiding the direction of future research to expand on the work conducted for this thesis.

The locations of the magnetopause crossings identified in Chapter 4 show considerable variation in distance from Mercury at the same latitude and MLT. The magnetopause model of Winslow *et al.* [2013] employed throughout this thesis is an average model that does not account for any external parameters such as magnetosheath plasma density, or the field strength and orientation, which have been shown to be important in describing the state of the magnetosphere. Given the large database of crossings identified here, and a further 5 Mercury years of MESSENGER data that was not included in any of these studies, an improved model featuring such external properties would give a better indication of the expected location of the magnetopause at any given time, and therefore the effect of erosion by reconnection.

The large database compiled in this thesis also provides an excellent basis for further investigation of FTE properties at Mercury, particularly once the final portion of the mission is analysed. Previous work has included modelling of flux ropes to estimate their orientation or magnetic flux content [e.g. Slavin *et al.*, 2010b; Rong *et al.*, 2013; Imber *et al.*, 2014], and extending this approach to the complete dataset will increase the understanding of how flux circulation at Mercury varies with conditions in the solar wind.

The BepiColombo mission [Benkhoff *et al.*, 2010] is currently en route to Mercury, and upon arrival in December 2025 will provide measurements of upstream solar wind properties that will facilitate a greatly improved magnetopause model. Crucially, it will also provide extensive coverage of the southern hemisphere dayside magnetosphere, filling in substantial data gaps from the MESSENGER orbital coverage. The improved coverage will also enable development of the results of Chapter 5, with significant southern hemisphere observations of flux transfer events allowing for the reconnection X-line location to be more precisely calculated.

The MESSENGER mission did not provide sufficient plasma measurements to accompany the magnetometer observations of FTEs, but improved plasma measurements from the Mercury Magnetospheric Orbiter [Saito *et al.*, 2010], one of two spacecraft in the BepiColombo mission, will provide further information about the flows driving magnetospheric convection that was estimated from FTE motions in Chapter 5. Additional FTE observations, both from the remaining MESSENGER data and BepiColombo, will allow construction of similar convection diagrams for magnetosheath field oriented predominantly along $\pm Y'_{MSM}$.

Although FTE observations have been shown to depend strongly on the orientation of the IMF, the effect of the magnetosheath field strength remains unexplained. Given the significant quantity of magnetic flux transported by FTEs, it is important to investigate whether the rate of formation shows any preference for either symmetric or asymmetric reconnection to further understanding of the overall magnetospheric dynamics at Mercury across a range of solar wind conditions.

Bibliography

Akasofu, S.-I. 1981. Energy coupling between the solar wind and the magnetosphere. *Space Sci. Rev.*, **28**(2), 121–190.

Alexeev, Igor I., Belenkaya, Elena S., Slavin, James A., Korth, Haje, Anderson, Brian J., Baker, Daniel N., Boardsen, Scott A., Johnson, Catherine L., Purucker, Michael E., Sarantos, Menelaos, & Solomon, Sean C. 2010. Mercury's magnetospheric magnetic field after the first two MESSENGER flybys. *Icarus*, **209**(1), 23–39.

Anderson, Brian J., Acuña, Mario H., Lohr, David A., Scheifele, John, Raval, Asseem, Korth, Haje, & Slavin, James A. 2007. The Magnetometer Instrument on MESSENGER. *Space Science Reviews*, **131**(1), 417–450.

Anderson, Brian J, Johnson, Catherine L, Korth, Haje, Purucker, Michael E, Winslow, Reka M, Slavin, James A, Solomon, Sean C, McNutt, Ralph L, Raines, Jim M, & Zurbuchen, Thomas H. 2011. The global magnetic field of Mercury from MESSENGER orbital observations. *Science (New York, N.Y.)*, **333**(6051), 1859–62.

Angelopoulos, V., Baumjohann, W., Kennel, C. F., Coroniti, F. V., Kivelson, M. G., Pellat, R., Walker, R. J., Lühr, H., & Paschmann, G. 1992. Bursty bulk flows in the inner central plasma sheet. *J. Geophys. Res.*, **97**(A4), 4027.

Axford, W. I., & Hines, C. O. 1961. A unifying theory of high-latitude geophysical phenomena and geomagnetic storms. *Can. J. Phys.*, **39**(10), 1433–1464.

Baumjohann, Wolfgang, & Paschmann, Götz. 1987. Solar wind-magnetosphere coupling: Processes and observations. *Phys. Scr.*, **T18**(T18), 61–72.

Baumjohann, Wolfgang, & Treumann, Rudolf A. 1997. *Basic Space Plasma Physics*. Imperial College Press.

Benkhoff, Johannes, van Casteren, Jan, Hayakawa, Hajime, Fujimoto, Masaki, Laakso, Harri, Novara, Mauro, Ferri, Paolo, Middleton, Helen R., & Ziethe, Ruth. 2010. BepiColombo—Comprehensive exploration of Mercury: Mission overview and science goals. *Planet. Space Sci.*, **58**(1-2), 2–20.

Berchem, Jean, & Russell, C. T. 1984. Flux Transfer Events on the Magnetopause: Spatial Distribution and Controlling Factors. *J. Geophys. Res.*, **89**(A8), 6689.

Blomberg, L. G., Cumnock, J. A., Glassmeier, K.-H., & Treumann, R. A. 2007. Plasma Waves in the Hermean Magnetosphere. *Space Sci. Rev.*, **132**(2-4), 575–591.

Burlaga, L.F. 2001. Magnetic fields and plasmas in the inner heliosphere: Helios results. *Planet. Space Sci.*, **49**(14-15), 1619–1627.

Cassak, P. A., & Shay, M. A. 2007. Scaling of asymmetric magnetic reconnection: General theory and collisional simulations. *Phys. Plasmas*, **14**(10), 102114.

Cooling, B. M. A., Owen, C. J., & Schwartz, S. J. 2001. Role of the magnetosheath flow in determining the motion of open flux tubes. *J. Geophys. Res. Sp. Phys.*, **106**(A9), 18763–18775.

Cowley, S. W. H. 1982. The causes of convection in the Earth's magnetosphere: A review of developments during the IMS. *Rev. Geophys.*, **20**(3), 531.

Cowley, S. W H, & Owen, C. J. 1989. A simple illustrative model of open flux tube motion over the dayside magnetopause. *Planet. Space Sci.*, **37**(11), 1461–1475.

Cowley, S. W.H. 1981. Magnetospheric asymmetries associated with the y-component of the IMF. *Planet. Space Sci.*, **29**(1), 79–96.

Crooker, N. U. 1979. Dayside merging and cusp geometry. *J. Geophys. Res.*, **84**(A3), 951.

Crooker, N. U., Siscoe, G. L., Eastman, T. E., Frank, L. A., & Zwickl, R. D. 1984. Large-scale flow in the dayside magnetosheath. *J. Geophys. Res.*, **89**(A11), 9711.

Dewey, Ryan M., Slavin, James A., Raines, Jim M., Baker, Daniel N., & Lawrence, David J. 2017. Energetic Electron Acceleration and Injection During Dipolarization Events in Mercury's Magnetotail. *J. Geophys. Res. Sp. Phys.*, **122**(12), 12,170–12,188.

DiBraccio, Gina A., Slavin, James A., Boardsen, Scott A., Anderson, Brian J., Korth, Haje, Zurbuchen, Thomas H., Raines, Jim M., Baker, Daniel N., McNutt, Ralph L., & Solomon, Sean C. 2013. MESSENGER observations of magnetopause structure and dynamics at Mercury. *Journal of Geophysical Research: Space Physics*, **118**(3), 997–1008.

DiBraccio, Gina A., Slavin, James A., Raines, Jim M., Gershman, Daniel J., Tracy, Patrick J., Boardsen, Scott A., Zurbuchen, Thomas H., Anderson, Brian J., Korth, Haje, McNutt, Ralph L., & Solomon, Sean C. 2015a. First observations of Mercury's plasma mantle by MESSENGER. *Geophys. Res. Lett.*, **42**(22), 9666–9675.

DiBraccio, Gina A., Slavin, James A., Imber, Suzanne M., Gershman, Daniel J., Raines, Jim M., Jackman, Caitriona M., Boardsen, Scott A., Anderson, Brian J., Korth, Haje, Zurbuchen, Thomas H., McNutt, Ralph L., & Solomon, Sean C. 2015b. MESSENGER observations of flux ropes in Mercury's magnetotail. *Planet. Space Sci.*, **115**(dec), 77–89.

Ding, D. Q., Lee, L. C., & Ma, Z. W. 1991. Different FTE signatures generated by the bursty single X line reconnection and the multiple X line reconnection at the dayside magnetopause. *Journal of Geophysical Research*, **96**(A1), 57.

Dong, X. C., Dunlop, M. W., Trattner, K. J., Phan, T. D., Fu, H. S., Cao, J. B., Russell, C. T., Giles, B. L., Torbert, R. B., Le, Guan, & Burch, J. L. 2017. Structure and evolution of flux transfer events near dayside magnetic reconnection dissipation region: MMS observations. *Geophysical Research Letters*, **44**(12), 5951–5959.

Dungey, J. W. 1961. Interplanetary Magnetic Field and the Auroral Zones. *Phys. Rev. Lett.*, **6**(Jan), 47–48.

Dungey, J.W. 1963. Interactions of solar plasma with the geomagnetic field. *Planet. Space Sci.*, **10**(jan), 233–237.

Dunlop, M. W., Zhang, Q.-H., Bogdanova, Y. V., Lockwood, M., Pu, Z., Hasegawa, H., Wang, J., Taylor, M. G. G. T., Berchem, J., Lavraud, B., Eastwood, J., Volwerk, M., Shen, C., Shi, J.-K., Constantinescu, D., Frey, H., Fazakerley, A. N., Sibeck, D., Escoubet, P., Wild, J. A., & Liu, Z.-X. 2011. Extended Magnetic Reconnection across the Dayside Magnetopause. *Phys. Rev. Lett.*, **107**(Jul), 025004.

Eastwood, J. P., Phan, T. D., Cassak, P. A., Gershman, D. J., Haggerty, C., Malakit, K., Shay, M. A., Mistry, R., Øieroset, M., Russell, C. T., Slavin, J. A., Argall, M. R., Avanov, L. A., Burch, J. L., Chen, L. J., Dorelli, J. C., Ergun, R. E., Giles, B. L., Khotyaintsev, Y., Lavraud, B., Lindqvist, P. A., Moore, T. E., Nakamura, R., Paterson, W., Pollock, C., Strangeway, R. J., Torbert, R. B., & Wang, S. 2016. Ion-scale secondary flux ropes generated by magnetopause reconnection as resolved by MMS. *Geophys. Res. Lett.*, **43**(10), 4716–4724.

Fairfield, D. H., & Cahill, L. J. 1966. Transition region magnetic field and polar magnetic disturbances. *J. Geophys. Res.*, **71**(1), 155–169.

Farrugia, C.J., Elphic, R.C., Southwood, D.J., & Cowley, S.W.H. 1987. Field and flow perturbations outside the reconnected field line region in flux transfer events: Theory. *Planet. Space Sci.*, **35**(2), 227–240.

Fear, R. C., Fazakerley, A. N., Owen, C. J., & Lucek, E. A. 2005. A survey of flux transfer events observed by Cluster during strongly northward IMF. *Geophys. Res. Lett.*, **32**(18).

Fear, R. C., Milan, S. E., Fazakerley, A. N., Owen, C. J., Asikainen, T., Taylor, M. G. G. T., Lucek, E. A., Rème, H., Dandouras, I., & Daly, P. W. 2007. Motion of flux transfer events: a test of the Cooling model. *Annales Geophysicae*, **25**(7), 1669–1690.

Fear, R. C., Milan, S. E., Fazakerley, A. N., Lucek, E. A., Cowley, S. W. H., & Dandouras, I. 2008. The azimuthal extent of three flux transfer events. *Annales Geophysicae*, **26**(8), 2353–2369.

Fear, R. C., Milan, S. E., Raeder, J., & Sibeck, D. G. 2010. Asymmetry in the bipolar signatures of flux transfer events. *J. Geophys. Res.*, **115**(A11), A11217.

Fear, R. C., Milan, S. E., & Oksavik, K. 2012a. Determining the axial direction of high-shear flux transfer events: Implications for models of FTE structure. *J. Geophys. Res.*, **117**(A9), A09220.

Fear, R. C., Palmroth, M., & Milan, S. E. 2012b. Seasonal and clock angle control of the location of flux transfer event signatures at the magnetopause. *J. Geophys. Res. Sp. Phys.*, **117**(4).

Fujimoto, M., Baumjohann, W., Kabin, K., Nakamura, R., Slavin, J. A., Terada, N., & Zelenyi, L. 2007. Hermean Magnetosphere-Solar Wind Interaction. *Space Sci. Rev.*, **132**(2-4), 529–550.

Fuselier, S. A., & Lewis, W. S. 2011. Properties of near-earth magnetic reconnection from in-situ observations. **160**(1-4), 95–121.

Fuselier, S. A., Trattner, K. J., Petrinec, S. M., Owen, C. J., & Réme, H. 2005. Computing the reconnection rate at the Earth's magnetopause using two spacecraft observations. *J. Geophys. Res. Sp. Phys.*, **110**(A6), A06212.

Fuselier, S. A., Vines, S. K., Burch, J. L., Petrinec, S. M., Trattner, K. J., Cassak, P. A., Chen, L. J., Ergun, R. E., Eriksson, S., Giles, B. L., Graham, D. B., Khotyaintsev, Yu V., Lavraud, B., Lewis, W. S., Mukherjee, J., Norgren, C., Phan, T. D., Russell, C. T., Strangeway, R. J., Torbert, R. B., & Webster, J. M. 2017. Large-scale characteristics of reconnection diffusion regions and associated magnetopause crossings observed by MMS. *Journal of Geophysical Research: Space Physics*, **122**(5), 5466–5486.

Gershman, Daniel J, Slavin, James A, Raines, Jim M, Zurbuchen, Thomas H, Anderson, Brian J, Korth, Haje, Baker, Daniel N, & Solomon, Sean C. 2013. Magnetic flux pileup and plasma depletion in Mercury's subsolar magnetosheath. *J. Geophys. Res. (sp. Physics)*, **118**, 7181–7199.

Glassmeier, Karl-Heinz. 2013. *Currents in Mercury's Magnetosphere.* Geophys. Mono. Series. (AGU).

Gold, Robert E., Solomon, Sean C., McNutt, Ralph L., Santo, Andrew G., Abshire, James B., Acuña, Mario H., Afzal, Robert S., Anderson, Brian J., Andrews, G. Bruce, Bedini, Peter D., Cain, John, Cheng, Andrew F., Evans, Larry G., Feldman, William C., Follas, Ronald B., Gloeckler, George, Goldsten, John O., Hawkins, S. Edward, Izenberg, Noam R., Jaskulek, Stephen E., Ketchum, Eleanor A., Lankton, Mark R., Lohr, David A., Mauk, Barry H., McClintock, William E., Murchie, Scott E., Schlemm, Charles E., Smith, David E., Starr, Richard D., & Zurbuchen, Thomas H. 2001. The MESSENGER mission to Mercury: Scientific payload. *Planet. Space Sci.*, **49**(14-15), 1467–1479.

Gonzalez, W. D., & Mozer, F. S. 1974. A quantitative model for the potential resulting from reconnection with an arbitrary interplanetary magnetic field. *J. Geophys. Res.*, **79**(28), 4186–4194.

Hauck, Steven A., Margot, Jean-Luc, Solomon, Sean C., Phillips, Roger J., Johnson, Catherine L., Lemoine, Frank G., Mazarico, Erwan, McCoy, Timothy J., Padovan, Sebastiano, Peale, Stanton J., Perry, Mark E., Smith, David E., & Zuber, Maria T. 2013. The curious case of Mercury's internal structure. *J. Geophys. Res. Planets*, **118**(6), 1204–1220.

Heyner, Daniel, Nabert, Christian, Liebert, Evelyn, & Glassmeier, Karl-Heinz. 2016. Concerning reconnection-induction balance at the magnetopause of Mercury. *J. Geophys. Res. Sp. Phys.*, **121**(4), 2935–2961.

Hood, L.L., & Schubert, G. 1979. Inhibition of solar wind impingement on mercury by planetary induction currents. *J. Geophys. Res.*, **84**(A6), 2641.

Hunt, G. J. 2016. *Analyses of field-aligned currents in Saturn's nightside magnetosphere*. Ph.D. thesis.

Imber, S. M., & Slavin, J. A. 2017. MESSENGER Observations of Magnetotail Loading and Unloading: Implications for Substorms at Mercury. *J. Geophys. Res. Sp. Phys.*, **122**(11), 11,402–11,412.

Imber, Suzanne M., Slavin, James A., Boardsen, Scott A., Anderson, Brian J., Korth, Haje, McNutt, Ralph L., & Solomon, Sean C. 2014. MESSENGER observations of large dayside flux transfer events: Do they drive Mercury's substorm cycle? *Journal of Geophysical Research: Space Physics*, **119**(7), 5613–5623. 2014JA019884.

Imperial College, London. 2014. *How a Fluxgate Magnetometer Works*. Online; accessed on 25-March-2019.

James, Matthew K., Imber, Suzanne M., Bunce, Emma J., Yeoman, Timothy K., Lockwood, Mike, Owens, Mathew J., & Slavin, James A. 2017. Interplanetary magnetic field properties and variability near Mercury's orbit. *J. Geophys. Res. Sp. Phys.*, **122**(8), 7907–7924.

Jasinski, Jamie M., Slavin, James A., Raines, Jim M., & DiBraccio, Gina A. 2017. Mercury's Solar Wind Interaction as Characterized by Magnetospheric Plasma Mantle Observations With MESSENGER. *J. Geophys. Res. Sp. Phys.*, **122**(12), 12153–12169.

JHU/APL. 2007a. *MESSENGER Instrumentation*. http://messenger.jhuapl.edu/About/Spacecraft-and-Instruments.html; accessed on 19-March-2019.

JHU/APL. 2007b. *MESSENGER Orbit*. http://messenger.jhuapl.edu/About/Mission-Design.html; accessed on 19-March-2019.

Johnson, Catherine L., Purucker, Michael E., Korth, Haje, Anderson, Brian J., Winslow, Reka M., Al Asad, Manar M. H., Slavin, James A., Alexeev, Igor. I., Phillips, Roger J., Zuber, Maria T., & Solomon, Sean C. 2012. MESSENGER observations of Mercury's magnetic field structure. *Journal of Geophysical Research: Planets*, **117**(E12).

Johnson, Catherine L., Philpott, Lydia C., Anderson, Brian J., Korth, Haje, Hauck, Steven A., Heyner, Daniel, Phillips, Roger J., Winslow, Reka M., & Solomon, Sean C. 2016. MESSENGER observations of induced magnetic fields in Mercury's core. *Geophys. Res. Lett.*, **43**(6), 2436–2444.

Kawano, H., & Russell, C. T. 1996. Survey of flux transfer events observed with the ISEE 1 spacecraft: Rotational polarity and the source region. *J. Geophys. Res. Sp. Phys.*, **101**(A12), 27299–27308.

Kawano, H., & Russell, C. T. 1997a. Cause of postterminator flux transfer events. *J. Geophys. Res. Sp. Phys.*, **102**(A12), 27029–27038.

Kawano, H., & Russell, C. T. 1997b. Survey of flux transfer events observed with the ISEE 1 spacecraft: Dependence on the interplanetary magnetic field. *J. Geophys. Res. Sp. Phys.*, **102**(A6), 11307–11313.

Kawano, H., & Russell, C. T. 2005. Dual-satellite observations of the motions of flux transfer events: Statistical analysis with ISEE 1 and ISEE 2. *Journal of Geophysical Research: Space Physics*, **110**(A7).

Kivelson, Margaret G., & Russell, Christopher T. 1995. *Introduction to space physics*. Vol. 58.

Korotova, G. I., Sibeck, D. G., & Petrov, V. I. 2012. Interball-1 observations of flux transfer events. *Ann. Geophys.*, **30**(10), 1451–1462.

Ku, Hwar C., & Sibeck, David G. 1997. Internal structure of flux transfer events produced by the onset of merging at a single X line. *Journal of Geophysical Research A: Space Physics*, **102**(A2), 2243–2260.

Ku, Hwar C., & Sibeck, David G. 2000. Flux transfer events produced by the onset of merging at multiple X lines. *Journal of Geophysical Research: Space Physics*, **105**(A2), 2657–2675.

Kuo, H., Russell, C. T., & Le, G. 1995. Statistical studies of flux transfer events. *J. Geophys. Res. Sp. Phys.*, **100**(A3), 3513–3519.

Lee, L. C., & Fu, Z. F. 1985. A theory of magnetic flux transfer at the Earth's magnetopause. *Geophys. Res. Lett.*, **12**(2), 105–108.

Leyser, Roger P., Imber, Suzanne M., Milan, Stephen E., & Slavin, James A. 2017. The Influence of IMF Clock Angle on Dayside Flux Transfer Events at Mercury. *Geophys. Res. Lett.*, **44**(21), 10,829–10,837.

Lockwood, Mike, Owens, Mathew J., Imber, Suzanne M., James, Matthew K., Bunce, Emma J., & Yeoman, Timothy K. 2017. Coronal and heliospheric magnetic flux circulation and its relation to open solar flux evolution. *J. Geophys. Res. Sp. Phys.*, **122**(6), 5870–5894.

Mardia, K. V., & Jupp, Peter E. 2000. *Directional statistics*. J. Wiley.

Masters, A., Eastwood, J. P., Swisdak, M., Thomsen, M. F., Russell, C. T., Sergis, N., Crary, F. J., Dougherty, M. K., Coates, A. J., & Krimigis, S. M. 2012. The importance of plasma βconditions for magnetic reconnection at Saturn's magnetopause. *Geophysical Research Letters*, **39**(8).

Milan, S. E., Cowley, S. W.H., Lester, M., Wright, D. M., Slavin, J. A., Fillingim, M., Carlson, C. W., & Singer, H. J. 2004. Response of the magnetotail to changes in the open flux content of the magnetosphere. *J. Geophys. Res. Sp. Phys.*, **109**(A4), A04220.

Milan, S. E., Provan, G., & Hubert, B. 2007. Magnetic flux transport in the Dungey cycle: A survey of dayside and nightside reconnection rates. *J. Geophys. Res. Sp. Phys.*, **112**(1).

Milan, S. E., Gosling, J. S., & Hubert, B. 2012. Relationship between interplanetary parameters and the magnetopause reconnection rate quantified from observations of the expanding polar cap. *J. Geophys. Res. Sp. Phys.*, **117**(3).

Moore, T. E., Fok, M. C., & Chandler, M. O. 2002. The dayside reconnection X line. *Journal of Geophysical Research: Space Physics*, **107**(A10), 1332.

Mozer, F. S., & Retinò, A. 2007. Quantitative estimates of magnetic field reconnection properties from electric and magnetic field measurements. *J. Geophys. Res.*, **112**(A10), A10206.

NASA. 2013. *Heliospheric Current Sheet.* https://www.nasa.gov/content/goddard/heliospheric-current-sheet; accessed on 2-February-2019.

NASA. 2018. *Mercury in Depth.* https://solarsystem.nasa.gov/planets/mercury/in-depth/; accessed on 22-February-2019.

Ness, N. F., Behannon, K. W., Lepping, R. P., Whang, Y. C., & Schatten, K. H. 1974. Magnetic field observations near Mercury: Preliminary results from Mariner 10. *Science (New York, N.Y.)*, **185**(4146), 151–160.

Ness, N. F., Behannon, K. W., Lepping, R. P., & Whang, Y. C. 1975. The magnetic field of Mercury, 1. *Journal of Geophysical Research*, **80**(19), 2708–2716.

Newell, P. T., Sotirelis, T., Liou, K., Meng, C.-I., & Rich, F. J. 2007. A nearly universal solar wind-magnetosphere coupling function inferred from 10 magnetospheric state variables. *J. Geophys. Res. Sp. Phys.*, **112**(A1).

Parker, E. N. 1958. Dynamics of the Interplanetary Gas and Magnetic Fields. *Astrophys. J.*, **128**(nov), 664.

Paschmann, G., Sonnerup, B. U. Ö., Papamastorakis, I., Sckopke, N., Haerendel, G., Bame, S. J., Asbridge, J. R., Gosling, J. T., Russell, C. T., & Elphic, R. C. 1979. Plasma acceleration at the Earth's magnetopause: evidence for reconnection. *Nature*, **282**(5736), 243–246.

Paschmann, G., Haerendel, G., Papamastorakis, I., Sckopke, N., Bame, S. J., Gosling, J. T., & Russell, C. T. 1982. Plasma and magnetic field characteristics of magnetic flux transfer events. *J. Geophys. Res.*, **87**(A4), 2159.

Perreault, Paul, & Akasofu, S.-I. 1978. A study of geomagnetic storms. *Geophys. J. R. Astron. Soc.*, **54**(3), 547–573.

Petschek, E. H. 1964. Magnetic field annihilation. *NASA Special Publication*, **50**(10), 425–439.

Petschek, H. E. 1966. The Mechanism for Reconnection of Geomagnetic and Interplanetary Field Lines. *Pages 257–273 of:* Mackin, Jr., R. J., & Neugebauer, M. (eds), *The Solar Wind*. Pergamon.

Phan, T. D., & Paschmann, Götz. 1996. Low-latitude dayside magnetopause and boundary layer for high magnetic shear: 1. Structure and motion. *J. Geophys. Res. Sp. Phys.*, **101**(A4), 7801–7815.

Phan, T. D., Paschmann, G., & Sonnerup, B. U. Ö. 1996. Low-latitude dayside magnetopause and boundary layer for high magnetic shear: 2. Occurrence of magnetic reconnection. *J. Geophys. Res. Sp. Phys.*, **101**(A4), 7817–7828.

Phan, T. D., Sonnerup, Bengt U. Ö., & Lin, Robert P. 2001. Fluid and kinetics signatures of reconnection at the dawn tail magnetopause: Wind observations. *J. Geophys. Res. Sp. Phys.*, **106**(A11), 25489–25501.

Phan, T. D., Paschmann, G., Gosling, J. T., Oieroset, M., Fujimoto, M., Drake, J. F., & Angelopoulos, V. 2013. The dependence of magnetic reconnection on plasma β and magnetic shear: Evidence from magnetopause observations. *Geophys. Res. Lett.*, **40**(1), 11–16.

Poh, Gangkai, Slavin, James A., Jia, Xianzhe, DiBraccio, Gina A., Raines, Jim M., Imber, Suzanne M., Gershman, Daniel J., Sun, Wei-Jie, Anderson, Brian J., Korth, Haje, Zurbuchen, Thomas H., McNutt, Ralph L., & Solomon, Sean C. 2016. MESSENGER observations of cusp plasma filaments at Mercury. *J. Geophys. Res. Sp. Phys.*, **121**(9), 8260–8285.

Pritchett, P. L. 2008. Collisionless magnetic reconnection in an asymmetric current sheet. *Journal of Geophysical Research: Space Physics*, **113**(A6).

Raines, Jim M, Gershman, Daniel J, Slavin, James A, Zurbuchen, Thomas H, Korth, Haje, Anderson, Brian J, & Solomon, Sean C. 2014. Structure and dynamics of Mercury's magnetospheric cusp: MESSENGER measurements of protons and planetary ions. *J. Geophys. Res.*, **119**(8), 6587–6602.

Raymer, K. M. 2018. *Influences on the location of the Earth's magnetopause*. Ph.D. thesis.

Rijnbeek, R. P., Cowley, S. W. H., Southwood, D. J., & Russell, C. T. 1984. A survey of dayside flux transfer events observed by ISEE 1 and 2 magnetometers. *J. Geophys. Res.*, **89**(A2), 786.

Rong, Z. J., Wan, W. X., Shen, C., Zhang, T. L., Lui, A. T. Y., Wang, Yuming, Dunlop, M. W., Zhang, Y. C., & Zong, Q. G. 2013. Method for inferring the axis orientation of cylindrical magnetic flux rope based on single-point measurement. *J. Geophys. Res. Sp. Phys.*, **118**(1), 271–283.

Russell, C. T., & Atkinson, G. 1973. Comments on a paper by J. P. Heppner, 'Polar cap electric field distributions related to interplanetary magnetic field direction'. *J. Geophys. Res.*, **78**(19), 4001–4002.

Russell, C. T., & Elphic, R. C. 1978. Initial ISEE magnetometer results - Magnetopause observations. *Space Science Reviews*, **22**(Dec.), 681–715.

Russell, C. T., & Walker, R. J. 1985. Flux transfer events at Mercury. *Journal of Geophysical Research: Space Physics*, **90**(A11), 11067–11074.

Saito, Y., Sauvaud, J.A., Hirahara, M., Barabash, S., Delcourt, D., Takashima, T., & Asamura, K. 2010. Scientific objectives and instrumentation of Mercury Plasma Particle Experiment (MPPE) onboard MMO. *Planet. Space Sci.*, **58**(1-2), 182–200.

Sandhu, J. K. 2016. *A statistical study of magnetospheric plasma mass loading using the Cluster spacecraft*. Ph.D. thesis.

Santo, Andrew G, Gold, Robert E, Jr., Ralph L McNutt, Solomon, Sean C, Ercol, Carl J, Farquhar, Robert W, Hartka, Theodore J, Jenkins, Jason E, McAdams, James V, Mosher, Larry E, Persons, David F, Artis, David A, Bokulic, Robert S, Conde, Richard F, Dakermanji, George, Jr., Milton E Goss, Haley, David R, Heeres, Kenneth J, Maurer, Richard H, Moore, Robert C, Rodberg, Elliot H, Stern, Theodore G, Wiley, Samuel R, Williams, Bobby G, wan L Yen, Chen, & Peterson, Max R. 2001. The MESSENGER mission to Mercury: spacecraft and mission design. *Planetary and Space Science*, **49**(14–15), 1481 – 1500.

Scholer, Manfred. 1988. Magnetic flux transfer at the magnetopause based on single X line bursty reconnection. *Geophysical Research Letters*, **15**(4), 291–294.

Schwartz, S. J. 1998. Shock and Discontinuity Normals, Mach Numbers, and Related Parameters. *ISSI Scientific Reports Series*, **1**, 249–270.

Shue, J.-H., Chao, J. K., Fu, H. C., Russell, C. T., Song, P., Khurana, K. K., & Singer, H. J. 1997. A new functional form to study the solar wind control of the magnetopause size and shape. *Journal of Geophysical Research: Space Physics*, **102**(A5), 9497–9511.

Sibeck, D. G., & Lin, R.-Q. 2010. Concerning the motion of flux transfer events generated by component reconnection across the dayside magnetopause. *J. Geophys. Res. Sp. Phys.*, **115**(A4).

Sibeck, D. G., & Lin, R. Q. 2011. Concerning the motion and orientation of flux transfer events produced by component and antiparallel reconnection. *J. Geophys. Res. Sp. Phys.*, **116**(7).

Sibeck, D. G., Siscoe, G. L., Slavin, J. A., Smith, E. J., Bame, S. J., & Scarf, F. L. 1984. Magnetotail flux ropes. *Geophys. Res. Lett.*, **11**(10), 1090–1093.

Sibeck, D. G., Korotova, G. I., Petrov, V., Styazhkin, V., & Rosenberg, T. J. 2005. Flux transfer events on the high-latitude magnetopause: Interball-1 observations. *Ann. Geophys.*, **23**(11), 3549–3559.

Siscoe, G. L., & Huang, T. S. 1985. Polar cap inflation and deflation. *J. Geophys. Res. Sp. Phys.*, **90**(A1), 543–547.

Slavin, J. A., Tsurutani, B. T., Smith, E. J., Jones, D. E., & Sibeck, D. G. 1983. Average configuration of the distant ($<$220 R e) magnetotail: Initial ISEE-3 magnetic field results. *Geophys. Res. Lett.*, **10**(10), 973–976.

Slavin, J. A., Baker, D. N., Craven, J. D., Elphic, R. C., Fairfield, D. H., Frank, L. A., Galvin, A. B., Hughes, W. J., Manka, R. H., Mitchell, D. G., Richardson, I. G., Sanderson, T. R., Sibeck, D. J., Smith, E. J., & Zwickl, R. D. 1989. CDAW 8 observations of plasmoid signatures in the geomagnetic tail: An assessment. *J. Geophys. Res.*, **94**(A11), 15153.

Slavin, James A., & Holzer, Robert E. 1979. The effect of erosion on the solar wind stand-off distance at Mercury. *J. Geophys. Res.*, **84**(A5), 2076.

Slavin, James A., & Holzer, Robert E. 1981. Solar wind flow about the terrestrial planets 1. Modeling bow shock position and shape. *J. Geophys. Res.*, **86**(A13), 11401.

Slavin, James A., Acuña, Mario H., Anderson, Brian J., Baker, Daniel N., Benna, Mehdi, Boardsen, Scott A., Gloeckler, George, Gold, Robert E., Ho, George C., Korth, Haje, Krimigis, Stamatios M., McNutt, Ralph L., Raines, Jim M., Sarantos, Menelaos, Schriver, David, Solomon, Sean C., Trávníček, Pavel, & Zurbuchen, Thomas H. 2009a. MESSENGER Observations of Magnetic Reconnection in Mercury's Magnetosphere. *Science*, **324**(5927), 606–610.

Slavin, James A, Anderson, Brian J, Zurbuchen, Thomas H, Baker, Daniel N, Krimigis, Stamatios M, Acuña, Mario H, Benna, Mehdi, Boardsen, Scott A, Gloeckler, George, Gold, Robert E, Ho, George C, Korth, Haje, McNutt, Ralph L, Raines, Jim M, Sarantos, Menelaos, Schriver, David, Solomon, Sean C, & Trávníček, Pavel. 2009b. MESSENGER observations of Mercury's magnetosphere during northward IMF. *Geophys. Res. Lett.*, **36**(2), L02101.

Slavin, James A, Anderson, Brian J, Baker, Daniel N, Benna, Mehdi, Boardsen, Scott A, Gloeckler, George, Gold, Robert E, Ho, George C, Korth, Haje, Krimigis, Stamatios M, McNutt, Ralph L, Nittler, Larry R, Raines, Jim M, Sarantos, Menelaos, Schriver, David, Solomon, Sean C, Starr, Richard D, Trávnícek, Pavel M, & Zurbuchen, Thomas H. 2010a. MESSENGER observations of extreme loading and unloading of Mercury's magnetic tail. *Science*, **329**(5992), 665–8.

Slavin, James A., Lepping, Ronald P., Wu, Chin-Chun, Anderson, Brian J., Baker, Daniel N., Benna, Mehdi, Boardsen, Scott A., Killen, Rosemary M., Korth, Haje, Krimigis, Stamatios M., McClintock, William E., McNutt, Ralph L., Sarantos, Menelaos, Schriver, David, Solomon, Sean C., Trávnícek, Pavel, & Zurbuchen, Thomas H. 2010b. MESSENGER observations of large flux transfer events at Mercury. *Geophysical Research Letters*, **37**(2). L02105.

Slavin, James A., Imber, Suzanne M., Boardsen, Scott A., DiBraccio, Gina A., Sundberg, Torbjorn, Sarantos, Menelaos, Nieves-Chinchilla, Teresa, Szabo, Adam, Anderson, Brian J., Korth, Haje, Zurbuchen, Thomas H., Raines, Jim M., Johnson, Catherine L., Winslow, Reka M., Killen, Rosemary M., McNutt, Ralph L., & Solomon, Sean C. 2012. MESSENGER observations of a flux-transfer-event shower at Mercury. *Journal of Geophysical Research: Space Physics*, **117**(A12). A00M06.

Slavin, James A., DiBraccio, Gina A., Gershman, Daniel J., Imber, Suzanne M., Poh, Gang Kai, Raines, Jim M., Zurbuchen, Thomas H., Jia, Xianzhe, Baker, Daniel N., Glassmeier, Karl-Heinz, Livi, Stefano A., Boardsen, Scott A., Cassidy, Timothy A., Sarantos, Menelaos, Sundberg, Torbjorn, Masters, Adam, Johnson, Catherine L., Winslow, Reka M., Anderson, Brian J., Korth, Haje, McNutt, Ralph L., & Solomon, Sean C. 2014. MESSENGER observations of Mercury's dayside magnetosphere under extreme solar wind conditions. *Journal of Geophysical Research: Space Physics*, **119**(10), 8087–8116.

Smith, A. W., Slavin, J. A., Jackman, C. M., Poh, G. K., & Fear, R. C. 2017. Flux ropes in the Hermean magnetotail: Distribution, properties, and formation. *J. Geophys. Res. Sp. Phys.*, **122**(8), 8136–8153.

Solomon, Sean C, Jr., Ralph L McNutt, Gold, Robert E, Acuña, Mario H, Baker, Daniel N, Boynton, William V, Chapman, Clark R, Cheng, Andrew F, Gloeckler, George, III, James W Head, Krimigis, Stamatios M, McClintock, William E, Murchie, Scott L, Peale, Stanton J, Phillips, Roger J, Robinson, Mark S, Slavin, James A, Smith, David E, Strom, Robert G, Trombka, Jacob I, & Zuber, Maria T. 2001. The MESSENGER mission to Mercury: scientific objectives and implementation. *Planetary and Space Science*, **49**(14–15), 1445–1465.

Solomon, Sean C., McNutt, Ralph L., Gold, Robert E., & Domingue, Deborah L. 2007. MESSENGER Mission Overview. *Space Science Reviews*, **131**(1), 3–39.

Sonnerup, B. U. Ö. 1974. Magnetopause reconnection rate. *J. Geophys. Res.*, **79**(1), 1546–1549.

Sonnerup, B. U. Ö, & Cahill, L. J. 1967. Magnetopause structure and attitude from Explorer 12 observations. *J. Geophys. Res.*, **72**(1), 171.

Sonnerup, B. U. Ö., & Scheible, M. 1998. Minimum and Maximum Variance Analysis. *ISSI Scientific Reports Series*, **1**, 185–220.

Sonnerup, B. U. Ö., Paschmann, G., Papamastorakis, I., Sckopke, N., Haerendel, G., Bame, S. J., Asbridge, J. R., Gosling, J. T., & Russell, C. T. 1981. Evidence for magnetic field reconnection at the Earth's magnetopause. *J. Geophys. Res. Sp. Phys.*, **86**(A12), 10049–10067.

Sonnerup, Bengt U. Ö. 1970. Magnetic-field re-connexion in a highly conducting incompressible fluid. *Journal of Plasma Physics*, **4**(1), 161–174.

Sonnerup, Bengt U. O. 1987. On the stress balance in flux transfer events. *J. Geophys. Res.*, **92**(A8), 8613.

Southwood, D.J., Farrugia, C.J., & Saunders, M.A. 1988. What are flux transfer events? *Planetary and Space Science*, **36**(5), 503 – 508.

Sun, W. J., Fu, S. Y., Slavin, J. A., Raines, J. M., Zong, Q. G., Poh, G. K., & Zurbuchen, T. H. 2016. Spatial distribution of Mercury's flux ropes and reconnection fronts: MESSENGER observations. *J. Geophys. Res. Sp. Phys.*, **121**(8), 7590–7607.

Sundberg, Torbjörn, Slavin, James A., Boardsen, Scott A., Anderson, Brian J., Korth, Haje, Ho, George C., Schriver, David, Uritsky, Vadim M., Zurbuchen, Thomas H., Raines, Jim M., Baker, Daniel N., Krimigis, Stamatios M., McNutt, Ralph L., & Solomon, Sean C. 2012. Messenger observations of dipolarization events in Mercury's magnetotail. *J. Geophys. Res. Sp. Phys.*, **117**(9).

Swisdak, M., Rogers, B. N., Drake, J. F., & Shay, M. A. 2003. Diamagnetic suppression of component magnetic reconnection at the magnetopause. *Journal of Geophysical Research: Space Physics*, **108**(A5).

Trattner, K. J., Mulcock, J. S., Petrinec, S. M., & Fuselier, S. A. 2007. Probing the boundary between antiparallel and component reconnection during southward interplanetary magnetic field conditions. *J. Geophys. Res. Sp. Phys.*, **112**(A8).

Trenchi, L., Fear, R. C., Trattner, K. J., Mihaljcic, B., & Fazakerley, A. N. 2016. A sequence of flux transfer events potentially generated by different generation mechanisms. *J. Geophys. Res. A Sp. Phys.*, **121**(9), 8624–8639.

Walsh, B. M., Foster, J. C., Erickson, P. J., & Sibeck, D. G. 2014. Simultaneous Ground- and Space-Based Observations of the Plasmaspheric Plume and Reconnection. *Science*, **343**(6175), 1122–1125.

Wang, Y. L., Elphic, R. C., Lavraud, B., Taylor, M. G.G.T., Birn, J., Raeder, J., Russell, C. T., Kawano, H., Zong, Q. G., Zhang, H., Zhang, X. X., & Friedel, R. H. 2005. Initial results of high-latitude magnetopause and low-latitude flank flux transfer events from 3 years of Cluster observations. *Journal of Geophysical Research: Space Physics*, **110**(A11).

Winslow, Reka M., Johnson, Catherine L., Anderson, Brian J., Korth, Haje, Slavin, James A., Purucker, Michael E., & Solomon, Sean C. 2012. Observations of Mercury's northern cusp region with MESSENGER's Magnetometer. *Geophys. Res. Lett.*, **39**(8), 1–6.

Winslow, Reka M., Anderson, Brian J., Johnson, Catherine L., Slavin, James A., Korth, Haje, Purucker, Michael E., Baker, Daniel N., & Solomon, Sean C.

2013. Mercury's magnetopause and bow shock from MESSENGER Magnetometer observations. *Journal of Geophysical Research: Space Physics*, **118**(5), 2213–2227.

Xiao, C. J., Pu, Z. Y., Ma, Z. W., Fu, S. Y., Huang, Z. Y., & Zong, Q. G. 2004. Inferring of flux rope orientation with the minimum variance analysis technique. *J. Geophys. Res. Sp. Phys.*, **109**(A11), A11218.

Zhong, J., Wan, W. X., Wei, Y., Slavin, J. A., Raines, J. M., Rong, Z. J., Chai, L. H., & Han, X. H. 2015. Compressibility of Mercury's dayside magnetosphere. *Geophys. Res. Lett.*, **42**(23), 10,135–10,139.

Zurbuchen, Thomas H., Raines, Jim M., Slavin, James A., Gershman, Daniel J., Gilbert, Jason A., Gloeckler, George, Anderson, Brian J., Baker, Daniel N., Korth, Haje, Krimigis, Stamatios M., Sarantos, Menelaos, Schriver, David, McNutt, Ralph L., & Solomon, Sean C. 2011. MESSENGER Observations of the Spatial Distribution of Planetary Ions Near Mercury. *Science*, **333**(6051), 1862–1865.

Zwan, B. J., & Wolf, R. A. 1976. Depletion of solar wind plasma near a planetary boundary. *J. Geophys. Res.*, **81**(10), 1636–1648.